THREE DIMENSIONAL REACTING FLOW ANALYSIS OF A
CAVITY-BASED SCRAMJET COMBUSTOR

A THESIS SUBMITTED TO
THE GRADUATE SCHOOL OF NATURAL AND APPLIED SCIENCES
OF
MIDDLE EAST TECHNICAL UNIVERSITY

BY

RAMIN ROUZBAR

IN PARTIAL FULFILLMENT OF THE REQUIREMENTS
FOR
THE DEGREE OF MASTER OF SCIENCE
IN
AEROSPACE ENGINEERING

FEBRUARY 2016

Approval of the thesis:

**THREE DIMENSIONAL REACTING FLOW ANALYSIS OF A
CAVITY-BASED SCRAMJET COMBUSTOR**

submitted by **RAMIN ROUZBAR** in partial fulfillment of the requirements for the degree of **Master of Science in Aerospace Engineering Department, Middle East Technical University** by,

Prof. Dr. Gülbin Dural Ünver
Dean, Graduate School of **Natural and Applied Sciences**   _____

Prof. Dr. Ozan Tekinalp
Head of Department, **Aerospace Engineering**   _____

Assoc. Prof. Dr. Sinan Eyi
Supervisor, **Aerospace Engineering Dept., METU**   _____

Examining Committee Members:

Prof. Dr. Serkan Özgen
Aerospace Engineering Dept., METU   _____

Assoc. Prof. Dr. Sinan Eyi
Aerospace Engineering Dept., METU   _____

Assoc. Prof. Dr. Oğuz Uzol
Aerospace Engineering Dept., METU   _____

Asst. Prof. Dr. Harika S. Kahveci
Aerospace Engineering Dept., METU   _____

Asst. Prof. Dr. Sıtkı Uslu
Mechanical Engineering Dept., TOBB University   _____

Date: 03.02.2016

I hereby declare that all the information in this document has been obtained and presented in accordance with academic rules and ethical conduct. I also declare that, as required by these rules and conduct, I have fully cited and referenced all material and results that are not original to this work.

Name, Last Name: Ramin Rouzbar

Signature:

ABSTRACT

THREE DIMENSIONAL REACTING FLOW ANALYSIS OF A CAVITY-BASED SCRAMJET COMBUSTOR

Rouzbar, Ramin

M.S., Department of Aerospace Engineering

Supervisor: Assoc. Prof. Dr. Sinan Eyi

February 2016, 120 pages

Scramjet engines have become one of the main interest areas of the supersonic propulsion systems. Scramjets are rather a new technology and they possess unsolved issues and problems regarding their operation, especially in the combustion process. Combustion at high speeds cause various problems as flame instability and poor fuel-air mixing efficiency. One of the methods used to overcome these problems is to recess cavity in the combustor wall where secondary flow is generated. In this study, a CFD tool is developed to analyze the reacting flow passing through the cavity-based scramjet combustor.

Developed CFD code is based on three dimensional coupled Navier-Stokes and finite rate chemistry equations. Ethylene-air reduced chemical reaction model is used as fuel-air combination. Non-dimensionalized governing equations are discretized by Finite Volume Method (FVM) and Newton GMRES method is used to solve the coupled system of equations. First and second order schemes are investigated with different flux vector splitting methods. Moreover, flux limiters are implemented to

improve the convergence of the second order schemes. It is found that second order schemes and Van Leer flux vector splitting methods are more accurate.

In order to remove the dependency of the solutions on grid resolution, mesh refinement is done. In addition, effect of various fuel injection angles and injector locations on the efficiency of the combustor are investigated. It is found that 90 degree fuel injection angle gives the best mixing efficiency while addition of downstream injectors do not contribute to the overall efficiency. To sum up, the fundamental aim of this study is to analyze the reacting flow through the scramjet combustor efficiently and also examine new methods to improve the performance of the combustor.

Keywords: Air-breathing propulsion, Reacting flow, Computational Fluid Dynamics, Supersonic combustion.

ÖZ

KAVİTELİ SCRAMJET YANMA ODASININ
ÜÇ BOYUTLU TEPKİLİ AKIŞ ANALİZİ

Rouzbar, Ramin

Yüksek Lisans, Havacılık ve Uzay Mühendisliği Bölümü

Tez Yöneticisi: Doç. Dr. Sinan Eyi

Şubat 2016, 120 sayfa

Scramjet motorları, süpersonik itki sistemlerinin önemli ilgili alanlarından biri haline gelmiştir. Scramjetler nispeten yeni bir teknoloji olup, işleyişi ile ilgili özellikle yanma sürecinde çözülmemiş problemlere sahiptir. Yüksek hızlarda yanma eylemini gerçekleştirmek bazı sorunlara neden olabilmektedir. Yüksek hızlardaki akışların düşük dayanma zamanı sebebi ile alev kararlı olamamakta ve yakıt-havanın karışma verimi düşük olmaktadır. Bu problemleri çözmek için önerilen yöntemlerden biri yanma odası duvarına kavite yerleştirerek ikincil akış oluşturmaktır. Bu çalışmada, scramjet yanma odasından geçen tepkili akışları analiz etmek için bir CFD yazılımı geliştirilmiştir.

Gelişitirilmiş CFD yazılımı, 3 boyutlu bağlaşık Navier-Stokes ve sonlu hız kimyasal denklemlerini çözmektedir. Etilen-hava kimyasal reaksiyon modeli yakıt-hava kombinasyonu olarak kullanılmıştır. Boyutsuzlandırılmış korunum denklemleri sonlu hacim yöntemi (FVM) ile ayrıklaştırılmıştır ve bağlaşık denklem sistemleri, Newton GMRES yöntemi ile çözülmüştür. Birinici ve ikinci dereceli şemalar ile birlikte akı vektörü ayırma yöntemleri araştırılmıştır. Ayrıca, akı kısıtlayıcıları ikinci

dereceli şemaların yakınsama özelliğini geliştirmek için uygulanmıştır. Bu çalışmalar sonucunda, ikinci dereceli şemalar ve Van Leer akı vektörü ayırma yöntemlerinin en doğru sonucu verdikleri anlaşılmıştır.

Sonuçların ağ boyutlarına bağımlı olmaksızın elde edilmesi için farklı boyutlarda ağlar oluşturulmuştur ve veriler ile karşılaştırılmıştır. Ek olarak, farklı yakıt enjeksiyon açılarının ve yerlerinin yanma odası performansının üzerindeki etkisi incelenmiştir. En yüksek karışma verimi 90 derece enjeksiyon açısında elde edilmiştir. Ayrıca, kaviteden sonra enjektör eklemenin yanma verimine pek katkısı olmadığı gözlenmiştir. Özetle, bu çalışmanın temel amacı scramjet yanma odası tepkili akışını verimli bir şekilde analiz etmek ve yanma odasının performansını geliştirmek için yeni yöntemler denemektir.

Anahtar kelimeler: Hava solunumlu itki sistemleri, Tepkili akışlar, Hesaplamalı Akışkanlar Dinamiği, Süpersonik yanma.

To my family

ACKNOWLEDGEMENTS

TABLE OF CONTENTS

LIST OF TABLES

TABLES

LIST OF FIGURES

FIGURES

xvi

xvii

LIST OF SYMBOLS

a	Speed of sound
C_p	Specific heat at constant pressure
e_t	Total energy per unit volume
$\hat{F}_c, \hat{G}_c, \hat{H}_c$	Convective (inviscid) flux vectors in generalized coordinates
$\hat{F}_v, \hat{G}_v, \hat{H}_v$	Viscous flux vectors in generalized coordinates
G	Gibbs free energy
H	Enthalpy
I	Total numbers of reactions
J	Jacobian of transformation matrix
K	Total number of species
K_e	Reaction rate equilibrium constant
k_f	Forward reaction rate
k_b	Backward reaction rate
L	Characteristic length
M	Mach number
p	Pressure
Q	Reaction products
$\hat{Q}$	Conservative vector of flow variables in generalized coordinates
R	Reaction reactants
$\hat{R}$	Residual vector
Re	Reynolds number
R_u	Universal gas constant
S	Entropy
$\hat{S}$	Chemical reaction source vector
T	Temperature
U, V, W	Contravariant velocity components

u, v, w	Velocity vector components
W	Molecular weight
ρ	Density
γ	Specific heat ratio
ξ, η, ζ	Generalized coordinates
ξ_x, ξ_y, ξ_z	Transformation metrics in ξ direction
η_x, η_y, η_z	Transformation metrics in η direction
$\zeta_x, \zeta_y, \zeta_z$	Transformation metrics in ζ direction
τ	Shear stress
$v'_{k,i}, v''_{k,i}$	Stoichiometric coefficients of the kth species in ith reaction
$\dot{\omega}$	Source term (production term) for the chemical species
χ	Chemical symbol for the reactants and products of the reaction

LIST OF ABBREVIATIONS

AUSM   Advection Upwind Splitting Method

CFD   Computational Fluid Dynamics

DNS   Direct Numerical Simulation

FDM   Finite Difference Method

FEM   Finite Element Method

FVM   Finite Volume Method

GMRES   Generalized Minimal Residual Method

LES   Large Eddy Simulation

METU   Middle East Technical University

NASA   National Aeronautics and Space Administration

RANS   Reynolds Averaged Navier Stokes

TÜBİTAK   The Scientific and Technological Research Council of Turkey

TVD   Total Variation Diminishing

CHAPTER 1

INTRODUCTION

1.1 Motivation of the Study

The basic principle of the Computational Fluid Dynamics (CFD) is to reduce the cost of the experimental studies. Analysis and design of the Scramjet engines are not an exception to this trend. In order to reduce the number of experiments and so, reduce the costs of design and speed up this process, Computational Fluid Dynamics tools are being used. Different algorithms and methods are being improved and implemented to these CFD tools to have a better understanding of the problems prior to their real life applications.

In this thesis, a CFD tool is developed to analyze the flow through the Scramjet engine combustor. Since the experimental studies of the high speed flows and especially hypersonic speeds are cumbersome and expensive, the use of Computational Fluid Dynamics tools become more crucial. Testing of Scramjet engines require highly developed laboratories with high-tech instruments which are only available in some of the countries today. In order to improve the vehicles flying at hypersonic speeds faster and with a lower cost, most of the design and analysis work should be done with modeling in computer areas, i.e. using CFD tools.

Scramjet combustion chamber is basically the most important part of the Scramjets. The design and analysis of the combustor is difficult compared to other parts of the engine since peak temperatures occurs at this part due to combustion process. In this thesis, the analysis of Combustor is done by developing a CFD tool which takes into account most of the processes happening in the combustion chambers such as mixing of the fuel-air, reactions, flame holding, etc.

1.2 Limitation of the Study

In this thesis, the analysis are done in steady state conditions. In other words, the time variant solutions are not considered. Also, turbulence models are not included in the solutions. The analysis are limited to the combustion chamber of the Scramjet engine. Other parts of the engine namely inlet, isolator and nozzle is not part of analysis.

1.3 Layout of the Study

Chapter 2 encloses the literature study about scramjet engines and hypersonic flow. This includes historical background of the supersonic air-breathing propulsion systems with a focus on scramjet engines. Different parts of the scramjet engine with their working principles are introduced. Different methods used to enhance the performance of the supersonic combustion are presented.

Chapter 3 gives theoretical background of the scramjet engine governing equations. The equations of motions for the flow analysis of a scramjet combustor analysis are briefly explained. Thermodynamic modeling of the flow and chemical reaction models are presented in this chapter.

Chapter 4 contains the computational algorithms and methods used to solve the problem for scramjet combustor. In this chapter, numerical discretization of the equations are shown. Different flux splitting methods and first and second order schemes are presented. Newton-GMRES method used in this study is explained.

In Chapter 5, the results for inviscid and viscous flows are simulated. Different grid resolutions are used as mesh refinement study and validation of the code is done. Effect of different numerical methods on solutions are investigated. Various fuel injection angle and patterns are compared. Analysis of the chemical reaction model is done and variation of flow variables and species are demonstrated by 3D contours.

Chapter 6 contains the general conclusions of the study. Moreover, the recommendation for the future work is also provided in here.

CHAPTER 2

LITERATURE REVIEW

This chapter is devoted to historical background of the development of the Scramjets. Moreover, brief explanation of the Scramjet working principles for different parts of the engine especially for combustion chamber is given. Most recent researches on the development of the cavity recessed scramjet combustors is presented.

2.1 Introduction to Scramjet Engines

Scramjet engines are named as Supersonic Combustion RAMJETS (SCRAMJETS). Since Scramjets are descendants of the ramjets, the definition of ramjets should be given in advance.

Ramjet engines are kind of air-breathing propulsion systems which uses the forward motion of the engine and specific inlet design to compress the air without the use of axial compressor. Therefore, Ramjet engines have no moving parts. Ramjets compresses the oncoming flow by passing it through one or more oblique shocks. After decelerating the flow into subsonic speeds the combustion occurs. Since ramjet engines need an oncoming flow at supersonic speeds, they are unable to operate at zero speed, i.e. at take-off. As a result, assisted take-off, by using other engine types will be required during take-off.

Since at high Mach numbers, typically above 5, decelerating the flow into subsonic speeds cause excessive pressure and temperature increase in the combustion chamber, the use of ramjet engines became non-profitable at these high speeds [1]. Therefore, the idea of the supersonic combustion is risen where the incoming flow is not needed to be decelerated to subsonic speeds. Therefore, the new type of ramjets

for which combustion occurs at supersonic speeds are introduced as supersonic combustion ramjet (Scramjet).

2.2 Historical Background

More than a century has passed since Rene Lorin discovered the idea of using ram pressure (pressure that is exerted on a body when it flows through a fluid) in propulsion systems in 1913 [1]. There has been lots of improvements in the area of hypersonic propulsion systems since then and many studies and experiments are done. Here some of the most important contributions is highlighted.

Rene Leduc started the conceptual design of the ramjet engine in 1920s but, got the patent with an airplane that has a ramjet in 1934 [2]. In 1928, Albert Fono from Hungary, patented by designing a propulsion system which had all of the components of today's ramjets. Unfortunately, the propulsion system designed by Fono was never built. Although Leduc got patent in 1934, the flights was delayed because of World War II. In 1946, experimental aircraft (Leduc 010) was constructed with the concept of the Leduc's design and its first powered flight took place in 1949 [1]. Interests in ramjet reached its maximum in 1950s and a lots of researches were done at that time.
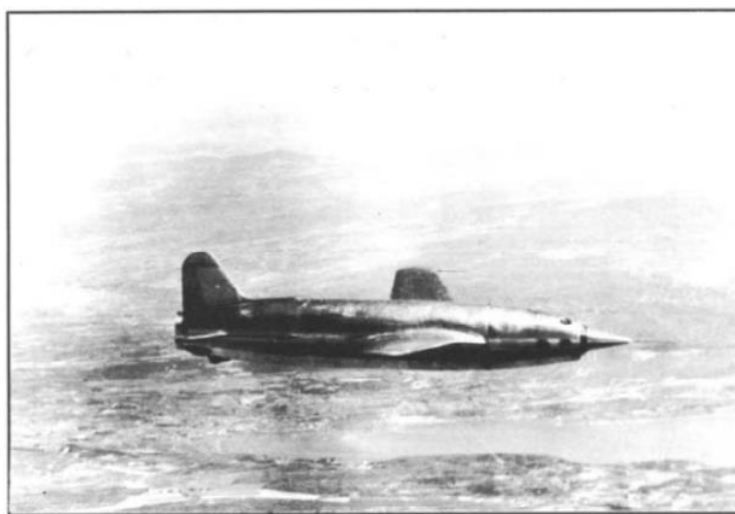
Figure 2.1 Experimental Aircraft of Leduc [1]

However, the development of the scramjet did not start until the late 1950s or early 1960s. In 1958, Weber and McKay [3] discovered that by the use of shock-wave interactions, efficient combustion (reduced loses) can be considered for flows at supersonic speeds. They indicate that with the proper inlet geometry, the scramjet can be more efficient than ramjet at flight speeds exceeding Mach 5. In 1960s, Antonio Ferri demonstrated a scramjet for the first time [4]. Following the works of Weber, McKay and Ferri, lots of research projects on the development of the scramjet engines were started.

The most important of these projects was NASA's HRE (Hypersonic Research Engine) project. The primary aim of the project is to test a hypersonic scramjet engine in flight using X-15A-2 research plane which should be modified to carry hydrogen for scramjet engine. Since the repair expenses of the X-15A-2 became too high, the X-15 project was cancelled in 1968 and the in flight test of the scramjet engine was not achieved [1]. Most of the research projects until then and afterwards for some years were continued on the development of scramjet by ground testing.

Fry [4] tabulated scramjet's evolution considering different projects from 1955 until 2004, which are shown in Table 2.1 and Table 2.2.

Table 2.1 Scramjet Evolution 1955-2003 [4]

Era	Country/service	Engine/vehicle	Engine type	Dates, year	Cruise Mach no.	State of development
1955–1975	U.S. Navy	External burn[b]	ERJ	1957–1962	5–7	Combustion tests
	Russia	Chetinkov research	ERJ	1957–1960	5–7	Component tests
	U.S. Air Force	Marquardt SJ	DMSJ	1960–1970	3–5	Cooled engine tests
	U.S. Air Force	GASL SJ[a]	SJ	1961–1968	3–12	Cooled engine tests
	U.S. Navy	SCRAM[b]	LFSJ	1962–1977	7.5	Free-jet test
	U.S. Air Force	IFTV[c]	H₂/SJ	1965–1967	5–6	Component tests
	U.S. Air Force–NASA	HRE[a]	H₂/SJ	1966–1974	4–7	Flowpath tests
	NASA	AIM[b]	H₂/SJ	1970–1984	4–7	Cooled engine tests
	France	ESOPE[b]	DMSJ	1973–1974	5–7	Component tests
1975–1990	U.S. Navy	WADM/HyWADM[b]	DCR	1977–1986	4–6	Component tests
	Russia	Various research	SJ/DCR	1980–1991	5–7	Combustion tests
	NASA	NASP[b]	MCSJ	1986–1994	0–26	Free-jet test (M7)
	Germany	Sänger II[b]	ATRJ	1988–1994	4	Concept vehicle

[a]System discussed and shown.   [b]System discussed.   [c]IFTV incremental flight test vehicle.

Table 2.2 Scramjet Evolution 1990-2003 [4]

Era	Country/service	Engine/vehicle	Engine type	Dates, year	Cruise Mach no.	Cruise altitude, ft	State of development
1990–2003	United Kingdom	HOTOL[c]	SJ	1990–1994	2–8	——	Combustion tests
	Japan	PATRES/ATREX[b]	TRBCC	1990–	0–12	100,000	Component tests
	Japan	NAL-KPL research[b]	SJ	1991–	4–12	50,000-100,000	Component tests
	Russia	Kholod[a]	DCR	1991–1998	3.5–5.4	50,000–115,000	Flight tests
	Russia/France	Kholod[a]	DCR	1991–1995	3.5–5.4	50,000–115,000	Flight tests
	Russia/United States	Kholod[a]	DCR	1994–1998	3.5–7	50,000–115,000	Flight tests
	France	CHAMIOS[b]	SJ	1992–2000	6.5	——	Component tests
	France	Monomat	DMSJ	1992–2000	4–7.5	——	Component tests
	France	PREPA[a]	DMSJ	1992–1999	2–12	0–130,000	Component tests
	Russia	ORYOL/MIKAKS	SJ	1993–	0–12	0–130,000	Component tests
	France/Russia	WRR[b]	DMSJ	1993–	3–12	0–130,000	Component tests
	Russia	GELA Phase II[a]	RJ/SJ	1995–	3–5+	295,000	Flight tests
	Russia	AJAX[b]	SJ	1995–	0–12	0–130,000	Concept
	U.S. Air Force	HyTech[a]	SJ	1995–	7–10	50,000–130,000	Component tests
	United States	GTX[d]	RBCC	1995–	0–14	50,000–130,000	Component tests
	U.S. Navy	Counterforce	DCR	1995–	4–8	80,000–100,000	Component tests
	NASA	X-43A/Hyper-X[a]	H2/SJ	1995–	7–10	100,000	Flight tests
	France/Germany	JAPHAR[a]	DMSJ	1997–2002	5–7.6	80,000	Component tests
	United States	ARRMD[b]	DCR	1997–2001	3–8	80,000	Component tests
	Russia	IGLA[a]	SJ	1999–	5–14	82,000–164,000	Flight tests
	NASA	X-43C[b]	DMSJ	1999–	5–7	100,000	Component tests
	Unites States	IHPTET[b]	ATR	1999–	0–5	0–90,000	Component tests
	United States	RTA[b]	TBCC	1999–	0–5	0–90,000	Component tests
	France	Promethee[b]	DMSJ	1999–2002	2–8	0–130,000	Component tests
	India	AVATAR-M[b]	SJ	1999–	0–14	0–orbit	Combustion tests
	United Kingdom	HOTOL Phase II	SJ	2000–	2–8	——	Component tests
	France	PIAF[b]	DMSJ	2000–	2–8	0–110,000	Component tests
	United States	MARIAH	MHD/SJ	2001–	15	——	Combustion tests
	Australia	HyShot[b]	SJ	2001–2002	7.6	75,000–120,000	Flight tests
	United States	Gun launch technology	SJ	2001–	——	——	Flight tests
	United States	ISTAR[b]	RBCC	2002–2003	2.4–7	0–orbit	Component tests
	United States	X-43B[b]	RB/TBCC	2002–2003	0–10	100,000	Component tests
	Russia	Mig-31 HFL[b]	SJ/DCR	2002–	2–10	50,000–130,000	Flight tests
	United States	HyFly[a]	DCR	2002–	3–6.5	85,000–95000	Flight tests planned
	United States	SED[a]	SJ	2003–	4.5–7	80,000	Planned flight tests
	France	LEA[a]	SJ/DCR	2003–2012	4–8	80,000	Flight tests planned
	United States	RCCFD[b]	TBCC	2003–	0.7–7	0–orbit	Flight tests planned

[a]System discussed and shown. [b]System discussed. [c]Horizontal takeoff and landing (HOTOL). [d]NASA Glenn Rc hydrogen fueled/cooled (GTX).

The first successful verified scramjet combustion in flight environment was achieved by Australian HyShot program in July 2002 [5]. The engine operated effectively and demonstrated the supersonic combustion. However, it was designed for the purpose of demonstrating the technological achievement of the supersonic combustion and it is not used to provide thrust to propel an aircraft. Later in 2004, the first flight with scramjet propulsion system which produced thrust is achieved by X-43A (Figure 2.2). On May 2010, X-51A wave rider broke the record of longest hypersonic flight time of 140 seconds by using Pratt & Whitney Scramjet engine.

Figure 2.2 NASA X-43A

2.3 Overview of the Scramjet Components

At high Mach numbers, above 3, pressure increase can be achieved by changing the inside geometry of the engine. In other words, there is no need for rotating elements such as compressors to increase the pressure of the incoming flow. Scramjets are designed based on this principle. Scramjet lacks any moving part and provides pressure increase necessary for the burning cycle by changing shape and area of the engine's inner geometry [6]. Scramjet engines basically consist of four main parts; inlet, isolator, combustor and nozzle. Theoretically scramjet design is very simple but practically, many problems arise which will be mentioned later. The components of the scramjet engine are shown schematically in Figure 2.3.
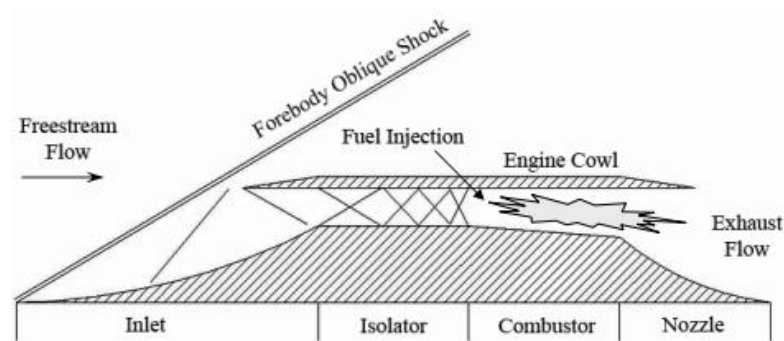
Figure 2.3 Schematic Illustration of a Scramjet Engine [7]

The inlets are designed to capture the air needed for the engine, decelerate the flow into speeds required by the engine with least possible loss in the total pressure and generating drag as small as possible [8]. Inlets of the scramjet engines are not favored to be separated from the fuselage. This is due to the fact that separating the body and engine will cause an increase in drag of the vehicle. Moreover, hypersonic boundary layers do not separate commonly compared to flows at low Mach numbers. Inlet design for the scramjets can be challenging because of the machinery limitation. To clarify, cooling might be needed for the inlet material and inlets might be required to change their geometry while flying. In other words, they can be required to have variable geometries to adapt for low and very high Mach numbers [6].

Increased heat values because of the combustion occurring in the combustor cause back pressure and reduction in the mass flow of the air which effects the inlet flow and may cause unstart. In order to prevent unstart, a component named 'isolator' is placed between inlet and combustor. Isolator contains the shock train created by the back pressure of the combustor and prevents it from reaching to the inlet.

Combustion chamber is a component where mixing of the fuel-air and supersonic combustion occurs. Detailed information about the scramjet combustor is given in the following section.

Nozzle is desired to expand the flow beyond combustor. Nozzle of a scramjet is a divergent duct which is suggested to be open type nozzle in order to adapt for the large pressure ratio required [6]. Open type are kind of nozzles which use vehicles aft-body as part of the nozzle.

2.4 Combustion Chamber

In scramjet, the combustion occurs at supersonic speeds. Since decelerating the flow into subsonic regions decreases the efficiency of the engine and cause other machinery problems, supersonic combustion is necessary at high Mach numbers [1]. However, air entering combustion chamber at supersonic speeds results in additional

difficulties which needs to be overcome. This makes the design of the combustion chamber to be the most challenging part of the scramjet propulsion system design. Since flow must be maintained at supersonic speeds throughout the combustor, the following problems arise [6]:

- Poor fuel-air mixing rate
- Reduced residence time
- Difficult flame holding

In order to overcome these problems, several studies were done and some methods were proposed. Most of the proposed ideas, solved some of the aforementioned difficulties but they also possessed some new issues. The main idea behind most of these methods is to use physical obstacle in the combustor. Obstacles in the flow path enhances the mixing and combustion efficiency by increasing the residence time. However, physical obstacles need cooling which is a severe problem in high enthalpy flows [9]. Moreover, pressure loss and increase in drag are additional problems. Some of the proposed and studied methods are introduced here.

2.4.1 Ramp Injectors

In order to enhance the mixing in the combustor, ramp injectors can be used. Ramp injector's principle is to increase the fuel-air mixing by adding axial velocity to the parallel injection [10]. This type of mechanism increases the mixing by producing counter-rotating vortices and creating shock and expansion waves caused by supersonic flow passing over the ramps. There are two types of ramp injectors; compression and expansion ramps. Both types are illustrated in Figure 2.4. Ramps which are raised in the flow path are compression types while the ramps recessed in the floor are of expansion type. Compression ramps create a stronger vortex but, since they do not reach to the smaller scale, expansion ramps result in better combustion efficiencies. Moreover, expansion ramps attain their maximum efficiencies in less distance then the compression ramps [11].
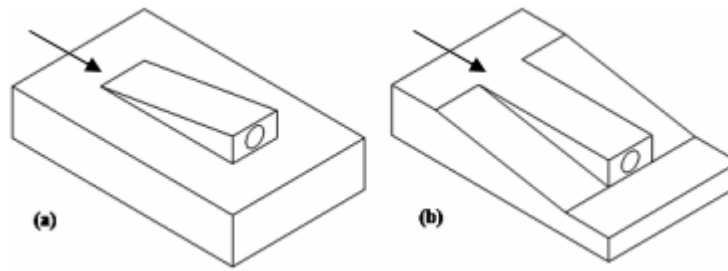
Figure 2.4 Ramp Injectors   a) Compression Type   b) Expansion Type [7]

Although Ramp injectors enhance the fuel-air mixing and combustion efficiency, they possess some crucial disadvantages. Since the fuel is injected along the wall, mixing can only be done only near to the wall until the shear layers expand enough through the core flow which will happen at the far downstream [6]. In addition, placing obstacles in flow path will cause pressure losses and consequently increase in the drag [7]. Physical obstacles in high enthalpy flows creates high temperatures which cause severe problems for the materials used.

2.4.2 Strut Injectors

Struts are placed vertically in the combustion chamber from bottom to the top. Struts are designed with a wedge at the leading edge and fuel injectors at the trailing edge [11]. Fuel injection is efficient in struts because the fuel is added to the flow throughout the whole flow field from several locations of the trailing edge. However, since struts are in-stream devices, they have significant pressure losses and remarkable contribution to the drag [12].
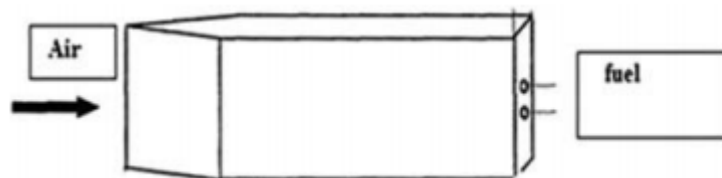
Figure 2.5 Wedge-Shaped Strut Injector [11]

10

To decrease the pressure loss, some researchers tried to modify the leading and trailing edge of struts. Considering this, NASA conducted experiments with different variations in the shape of the struts to determine the effect of different parameters such as thickness, length, leading edge sweep, etc. [13]. It is concluded that thickness of the strut has the most contribution to the drag. Moreover, a study on wedge-shaped and diamond-shaped strut injection and its results show that the wedge-shaped strut injectors are more efficient [14]. Although strut injectors provide proper fuel injection to the flow but, high pressure losses and increase in drag because of pressure loss has not been solved yet.

2.5 Cavity Flameholders

In late 90s, cavity flame holders were proposed as a new concept for flame stabilization in supersonic combustion chambers [15]. In this concept, fuel injection methods are combined with flame holding techniques. Cavities were first employed by Central Institution of Aviation Motors (CIAM) in Russia. Cavity technique were first used for flight tests of a Russian/French dual-mode Scramjet [16]. In the following experiments it is observed that implementations of cavities increased the hydrocarbon combustion efficiency remarkably [17].

The principle idea behind cavity technique is to create a recirculation region where the mixing of the fuel and air occurs at relatively low speeds [18]. Since cavities are recessed in the combustor, pressure losses are decreased compared to other techniques where the devices are placed in-stream. By creating low speed recirculation regions, cavities increase the residence time and so, mixing and combustion becomes more efficient and stable. Since there are many factors affecting the performance of the cavity flame holders such as cavity geometry, fuel injection patter and fuel type and so on, cavity stabilization method has not been fully understood yet. Many researches are going on studying cavities with different geometries and varying characteristics.

Generally, cavities are separated into two categories regarding their geometry: open and closed cavities [19]. The parameter used to characterize cavities is Length-to-Depth ratio (L/D) of the cavity. Cavities are called "open" when their length to depth ratio is lower than ten (L/D < 10). In open cavity flows, the shear layer separated from the upstream corner reattaches to the aft-wall of the cavity downstream. In open cavity flow regimes with smaller aspect ratio (L/D < 2-3) where single large vortex is formed in the cavity, transverse oscillations are dominant. Whereas, in open cavities of higher length to depth ratio where cavity is filled with several vortices (Figure 2.6), longitudinal oscillations are more dominant [20]. Shear layer impingement at the aft-wall of the open cavities results in high pressure and so increases the drag.

The second category of the cavities which are called "closed", have length to depth ratio higher than ten, L/D > 10. In closed cavity flow regimes, shear layer formed at the upstream corner cannot pass the entire cavity and reattaches to the cavity floor. Closed cavities generate great drag coefficients because of pressure increase at the aft-wall and pressure decreases at front wall [21]. Drag values are higher in closed cavities compared to open ones. Hence, open cavities are preferred for the use in scramjet combustion chambers.
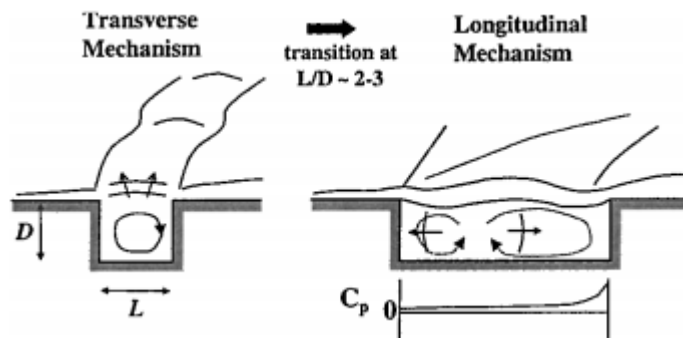
Figure 2.6 Open Cavity Flow, L/D < 10 [21]
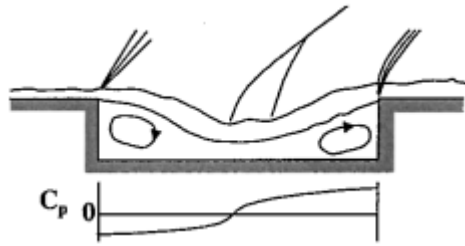
Figure 2.7 Closed Cavity Flow, L/D > 10 [21]

A study from Hsu et al. [22] has shown that closed cavities results in unstable flames while open cavities with low aspect ratio does not provide the volume necessary for flame holding. Stable combustion was achieved for a limited range of L/D which corresponds to minimum drag and entrainment.

The most efficient cavities are open cavities with higher aspect ratios. However, in this flow regimes oscillations are controlled by longitudinal mechanisms. The longitudinal oscillations are explained with two basic models [21]. As shear layer forms at the upstream corner of the cavity and then reattaches to the aft-wall causes an increase in the cavity pressure. Therefore a compression wave is being generated which travels upstream to the front wall. The first model suggests that this wave produces vortices in the front wall which amplify while traveling downstream as can be seen in the Figure 2.8. This will deflect shear layer and cause shock/impingement at the aft-wall. Unlikely, the second model proposes that shear layer deflection is a result of compression wave reflection of itself from the front wall, not the induction of vortices (Figure 2.8).

a) First Model   b) Second Model
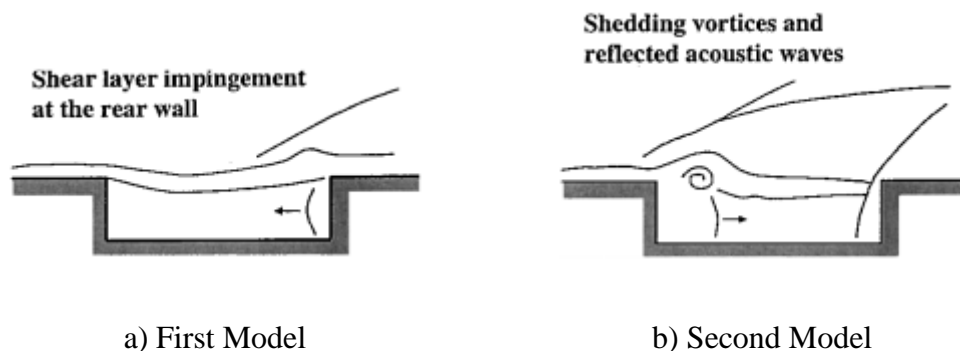
Figure 2.8 Proposed Models for Explanation of Longitudinal Oscillations [21]

13

Since shear layer interaction with the cavity aft-wall is the basic factor for fluctuations in the cavity, controlling the formation of the shear layer can prevent the cavity oscillations. For this purpose, passive and active methods to control the shear layer are introduced. In passive methods, control of the shear layer is done by installing vortex generators or spoilers upstream of the cavity or by inclining the cavity aft-wall. In this way, formation of shear layers and their reattachments to the aft-wall will be controlled and consequently compression waves will not be reflected into the cavity (Figure 2.9.). On the other hand, in active control methods, formation of shear layer is controlled by mechanics, acoustic or fluid injection methods. Upstream mass injection as can be seen in Figure 2.10, is the most promising technique. Since active control methods can be adapted to various conditions, they are more efficient than the passive methods.
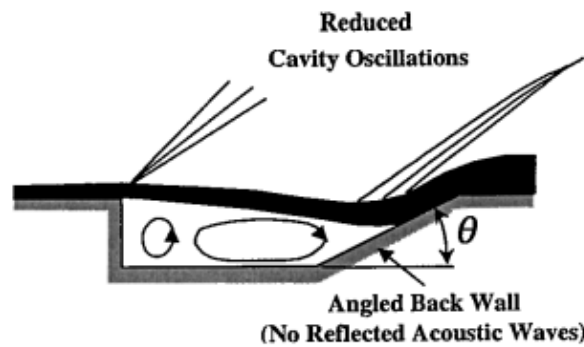
Figure 2.9 Angled Back wall as a Passive Control Method [21]
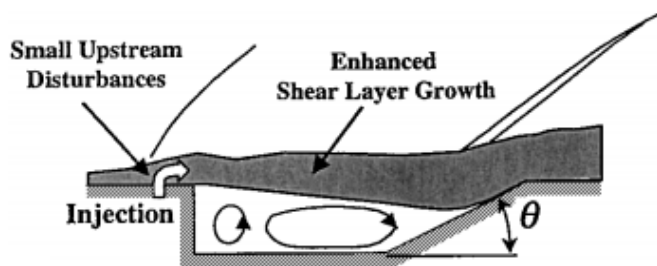
Figure 2.10 Upstream Fuel Injection as an Active Control Method [21]

Ben-Yakar [23] demonstrated the effect of inclined cavity aft-wall on the reattachment of the shear layer and its stabilizing effect. From the experiment results,

it is concluded that for cavity with 90 degree aft-wall, compression waves were propagated into the cavity. This occurs after the generation of shock waves in the shear layer reattachment location, at the cavity trailing edge. However, in the inclined cavities, shear layer reattaches to the aft-wall in a steady manner so that no acoustic waves are reflected inside of the cavity.
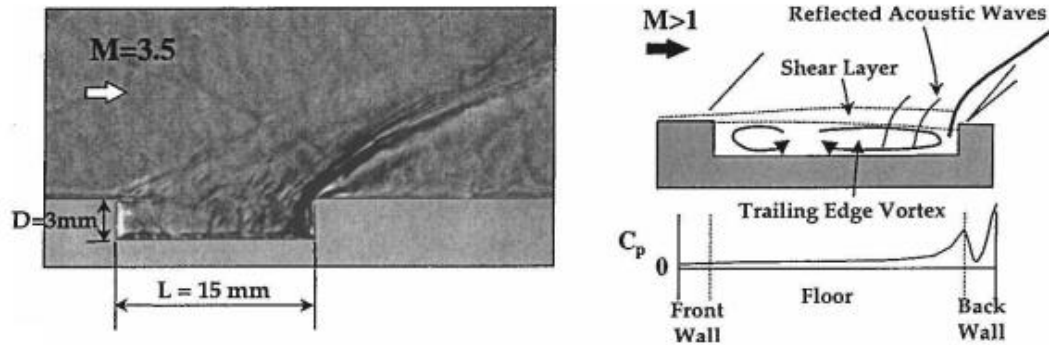
Figure 2.11 Unsteady Nature of Shear Layer at 90-deg Aft-wall [23]
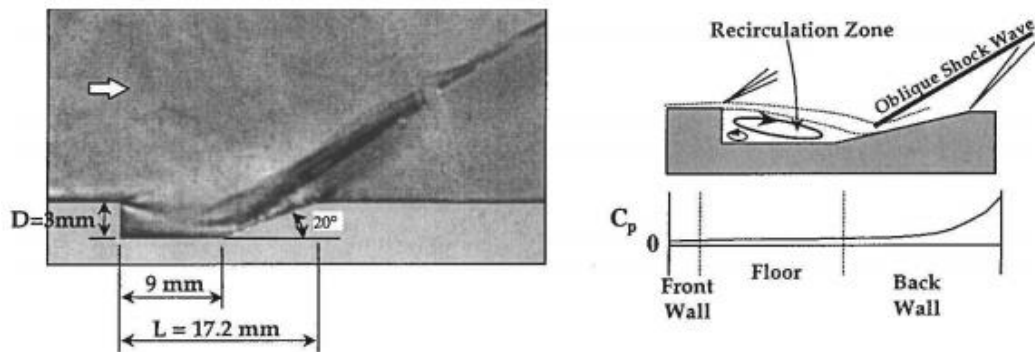
Figure 2.12 Steady Shear Layer Reattachment at Inclined Cavity Aft-wall [23]

Pressure drag produced in the cavity is a result of following reasons. First, pressure difference between the aft-wall back face and free-stream pressure. This pressure difference will cause net force in the x-direction, i.e. drag force will be generated. Second, high pressure region will be generated at the location of shear layer reattachment. This creates a net force in x-direction on the front wall face inside the cavity [21].

15

Experimental studies of Zhang and Edwards [20] shown that in longitudinal mode (L/D > 3), cavity drag increases significantly as L/D increases. This is due to the fact that by increasing L/D, oscillations are damped at the reattachment location and so pressure increases at the aft-wall of the cavity. Moreover, because of momentum diffusion, pressure drops at the front wall. These pressure fluctuations cause an increases in the cavity drag as shown in Figure 2.13.
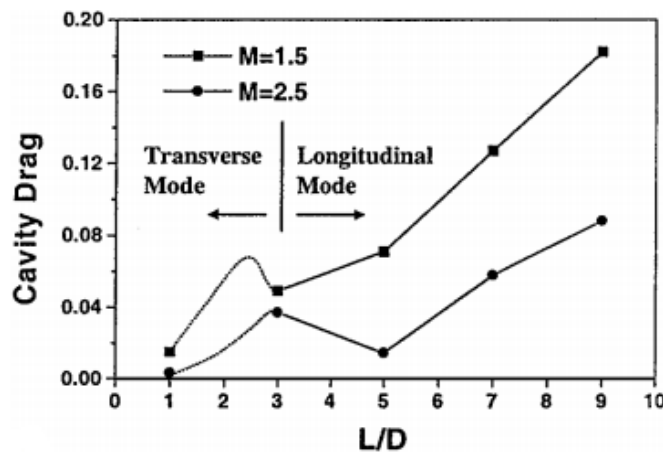
Figure 2.13 Cavity Drag for Different L/D [23]

As can be concluded from the aforementioned studies, cavity drag is mostly effected by the aft-wall of the cavity. Therefore, several studies are done regarding the design of back wall. Researches of Gruber et al. [19] demonstrated that drag increases for small angles ($\theta = 16$) of the aft-wall. Small angles lead to creation of expansion waves at the cavity upstream which increases drag since pressure decreases at the aft-wall face. Therefore, large pressure difference contributed to high drag values. However, the studies of Zhang et al. [24] shows that decreasing back wall angle from $\theta = 90$ to $\theta = 45$, decreased the drag coefficient. In another study from Samimy et al. [25], a cavity with aft-wall angle of 20 degree is chosen to minimize the pressure difference upstream and downstream of the cavity. This is the key for decreasing the cavity drag. From all these studies it can be concluded that minimum drag coefficient may occur at the wall angle between $\theta = 16$ and $\theta = 45$ degrees.

16

2.6 Numerical Methods

In order to analyze the flow in the scramjet combustor different computational models can be implemented. Reynolds averaged Navier-Stokes equations (RANS), Large Eddy Simulations (LES) and Direct Numerical Simulations (DNS) are used for simulation purposes. DNS is very expensive to solve the complex reacting flows. Therefore, RANS and LES methods are the mostly used methods in flow analysis of the scramjets. Baurle and Eklund [9] used the VULCAN Navier-Stokes code in their studies. In this code, Reynolds averaged equations were solved with cell-centered finite volume method. For chemical reaction modeling, finite rate kinetics model was implemented. In their study, Menter Baseline (BSL) and Menter Shear Stress Transport (SST) turbulence models were used. Edwards low-diffusion flux split scheme was employed with Van Leer flux limiter.

Lin et al. [26] used the CFD++ code to perform analysis and simulations on scramjet model. The simulations were done based on finite volume method, multi-dimension TVD (Total Variation Diminishing) schemes and Harten-Lax-van Leer-Contact (HLLC) Riemann solver with minmod flux limiter. Two-equation $\kappa - \varepsilon$ turbulence model was employed. Reduced finite rate kinetics model was used for modeling reacting flows. In a study of Ghodke et al. [27], second order accurate block structured finite volume method was used to solve the LES equations. Linear Eddy Mixing (LEM) and Artificial Neural Network (ANN) models were used for chemical reaction calculations. In order to evaluate the fluxes a hybrid methodology characterized by shock/interaction interactions was implemented.

CHAPTER 3

PHYSICAL MODELING

In the scramjet combustor, the flow is characterized by the fluid motion along with chemical reactions. In other words, reacting flow is the basic characteristic of the flows which experience combustion. Governing equations of these flows are principle conservation laws of fluid mechanics and chemical reaction mechanisms. Theoretical background are given as follows.

3.1 Governing Equations of Fluid Motion

Differential form of the conservation of mass, momentum and energy are applied for a distinctive volume of the fluid which can be shown mathematically in the following manner for Cartesian coordinate systems.

Conservation of mass in its differential form which is known as continuity equation is given as:

$$\frac{\partial \rho}{\partial t} + \frac{\partial}{\partial x}(\rho u) + \frac{\partial}{\partial y}(\rho v) + \frac{\partial}{\partial z}(\rho w) = 0 \qquad (3.1)$$

Momentum equations which are referred to as Navier-Stokes equations are shown in the following.

Momentum in the x-direction:

$$\frac{\partial}{\partial t}(\rho u) + \frac{\partial}{\partial x}(\rho u^2 + p) + \frac{\partial}{\partial y}(\rho uv) + \frac{\partial}{\partial z}(\rho uw)$$
$$= \frac{\partial}{\partial x}(\tau_{xx}) + \frac{\partial}{\partial y}(\tau_{xy}) + \frac{\partial}{\partial z}(\tau_{xz}) \qquad (3.2)$$

Momentum in y-direction:

$$\frac{\partial}{\partial t}(\rho v) + \frac{\partial}{\partial x}(\rho u v) + \frac{\partial}{\partial y}(\rho v^2 + p) + \frac{\partial}{\partial z}(\rho v w)$$

$$= \frac{\partial}{\partial x}(\tau_{xy}) + \frac{\partial}{\partial y}(\tau_{yy}) + \frac{\partial}{\partial z}(\tau_{yz}) \tag{3.3}$$

Momentum in the z-direction:

$$\frac{\partial}{\partial t}(\rho w) + \frac{\partial}{\partial x}(\rho u w) + \frac{\partial}{\partial y}(\rho v w) + \frac{\partial}{\partial z}(\rho w^2 + p)$$

$$= \frac{\partial}{\partial x}(\tau_{xz}) + \frac{\partial}{\partial y}(\tau_{yz}) + \frac{\partial}{\partial z}(\tau_{zz}) \tag{3.4}$$

Conservation of Energy:

$$\frac{\partial}{\partial t}(\rho e_t) + \frac{\partial}{\partial x}(\rho u e_t + pu) + \frac{\partial}{\partial y}(\rho v e_t + pv) + \frac{\partial}{\partial z}(\rho w e_t + pw)$$

$$= \frac{\partial}{\partial x}\left(u\tau_{xx} + v\tau_{xy} + w\tau_{xz} - q_x\right) + \frac{\partial}{\partial y}\left(u\tau_{xy} + v\tau_{yy} + w\tau_{yz} - q_y\right) \tag{3.5}$$

$$+ \frac{\partial}{\partial z}\left(u\tau_{xz} + v\tau_{yz} + w\tau_{zz} - q_z\right)$$

In addition to fundamental conservation laws of fluid mechanics, conservation of mass should be applied for every species in reacting flows.

$$\frac{\partial \rho_k}{\partial t} + \frac{\partial}{\partial x}(\rho_k u) + \frac{\partial}{\partial y}(\rho_k v) + \frac{\partial}{\partial z}(\rho_k w) = \dot{\omega}_k \tag{3.6}$$

where, subscript k denotes different species and $\dot{\omega}_k$ is the source term for the species which will be explained in the following sections.

3.2 Thermodynamic Model

In order to close the system of equations, equation of state is used which relates the thermodynamic properties. The pressure is related to density and internal energy as follows:

$$p = p(\rho, e, \rho_k) \qquad (3.7)$$

where, e is the internal energy and ρ_k is the density of the kth species.

In low enthalpy flows where temperatures are below 1000 K, ideal gas assumption is used. In ideal gas assumption, the specific heats, C_p and C_v are constant and so specific heat ratio is also a constant. However, in high enthalpy flows, the specific heats become temperature dependent variables.

In order to estimate the specific heats as a function of temperature, several models such as one temperature and two temperature models are developed. In one temperature models, all energy modes are assumed to be in equilibrium mode. These methods are simpler compared to other methods, but, equilibrium rates are overestimated [28]. In two temperature models, two distinctive temperatures are used in formulation. One for translational energy modes and the other for vibrational energy modes. Hence, two temperature models are complex and solving the coupled equation for these two temperature requires large computation time and sources. Moreover, vibrational energy can be neglected compared to temperatures of chemical reactions. Therefore, one temperature models are sufficient to estimate the values of the specific heats accurately.

The energy of different species are found as functions of temperature and tabulated with molar thermodynamic data. However, in order to use these tables for computational purposes, data are used to fit a polynomial equation [29]. A 9-constant form of these polynomial curve fits are used for representation of thermodynamic properties [30].

The specific heat at constant pressure is modeled as:

$$\frac{C^o_{p,k}(T)}{R} = a_1\,\frac{1}{T^2} + a_2\,\frac{1}{T} + a_3 + a_4\,T + a_5\,T^2 + a_6\,T^3 + a_7\,T^4 \qquad (3.8)$$

Specific heat at constant pressure of a mixture is written as [31]:

$$C_{pm} = \sum_{k=1}^{K} \frac{\rho_k}{\rho}\,C_{p,k} \qquad (3.9)$$

Integration of polynomial for $C^o_{p,k}$ is employed to find the enthalpy for temperature T.

$$H^o = \int_{T_0}^{T} C^o_p\,dT + B \qquad (3.10)$$

where B is the constant of integration which makes the enthalpy zero at reference temperature. Reference state of elements are accepted to be the stable phase of pure elements at temperatures and pressures of $298.15\,K$ and $1\,bar$, respectively. Therefore, reference temperature is chosen as $298.15\,K$. For different temperatures, enthalpy is calculated as sensible heat added to the heat of formation at reference temperature [32].

$$H^o(T) = \Delta_f H^o(298.15) + [H^o(T) - H^o(298.15)] \qquad (3.11)$$

Polynomial to estimate the enthalpy is derived as follows:

$$\frac{H^o_k(T)}{RT}$$

$$= -a_1\,\frac{1}{T^2} + a_2\,\frac{ln\,(T)}{T} + a_3 + a_4\,\frac{T}{2} + a_5\,\frac{T^2}{3} + a_6\,\frac{T^3}{4} + a_7\,\frac{T^4}{5} + \frac{b_1}{T} \qquad (3.12)$$

Mixture's enthalpy can be calculated as:

22

$$H_m = \sum_{k=1}^{K} \frac{\rho_k}{\rho} H_k \qquad (3.13)$$

In order to find the polynomial for entropy change, specific heat at constant pressure is divided by temperature and then integrated. The integration bounds from the reference temperature to the local temperature.

$$S^o = \int_{T_0}^{T} \frac{C_p^o}{T} dT + C \qquad (3.14)$$

The polynomial is found to be as:

$$\frac{S_k^o(T)}{R}$$
$$= -a_1 \frac{1}{2T^2} - a_2 \frac{1}{T} + a_3 \, lnT + a_4 T + a_5 \frac{T^2}{2} + a_6 \frac{T^3}{3} + a_7 \frac{T^4}{4} + b_2 \qquad (3.15)$$

Entropy of the mixture is also can be found as:

$$S_m = \sum_{k=1}^{K} \frac{\rho_k}{\rho} S_k \qquad (3.16)$$

where, $a_1, a_2, ..., a_7$ are coefficients of the polynomial equation written for thermodynamic data calculations of different species and b_1 and b_2 are constants of the integration [30]. Chemical properties and polynomial coefficients data of the species used in this study are given in Appendix A.

For different species, the value of internal energy can be calculated as:

$$E^o = H^o - RT \qquad (3.17)$$

The specific internal energy can be estimated by using mass fraction of different species with the molar values using the equation given as follows.

$$e = \sum_{k=1}^{K} \frac{\rho_k}{\rho} E_k^o \qquad (3.18)$$

In one temperature model, total energy is formulated as:

$$E = e + \frac{1}{2}(u^2 + v^2 + w^2) + \sum_{k=1}^{K} \frac{\rho_k}{\rho} H_k^0 \qquad (3.19)$$

Moreover, the pressure of the mixture is calculated by the following equation.

$$p = \rho R_u T \sum_{k=1}^{K} \frac{C_k}{W_k} = R_u T \sum_{s=1}^{K} \frac{\rho_k}{W_k} \qquad (3.20)$$

where W_k is the kth species' molecular weight.

3.3 Chemical Reaction Model

In order to solve the reacting flows, chemistry of the flow should be modeled as well. The coupled system of governing equations with chemical reaction models should be employed to model the fluid motion. Implementing accurate and complex chemical reaction models require very large computers and computation time. Hence, the use of extensive chemical models are computationally inefficient. These chemistry models can be simplified and reduced to less complex mechanisms so that the solution of the governing equations coupled with chemical reaction become numerically efficient and economically beneficial [33]. Finite rate chemical reaction model is one of the widely used chemistry models which integrates time rate of change of the gas compounds. The detailed representation of the finite rate chemical model is given in the following sections.

3.3.1 Equilibrium Constant

Chemical reactions are represented by

$$\sum_{k=1}^{K} v_k' R_k \;\rightleftarrows\; \sum_{k=1}^{K} v_k'' Q_k \tag{3.21}$$

where, v_k' and v_k'' are stoichiometric coefficients of the reactants R_k and products Q_k, respectively. In order to calculate the equilibrium constant for different reactions, Gibbs function is needed. The Gibbs free energy is found as:

$$G^o = H^o - TS^o \tag{3.22}$$

Since Gibbs free energy is an extensive property and related to enthalpy and entropy, it can be defined by its value at stable condition of $T = 298.15\ K$ and $p = 1\ atm$.

$$G_k = G_k^o + RT\ ln(\frac{p_k}{p_0}) \tag{3.23}$$

where G_k^o is the Gibbs free energy at stable conditions and p_k is the partial pressure of species k. Partial pressure of the reactants and products can be derived as [34]:

$$-\Delta G^o = RT\ ln\ (\prod_k Q_k^{v_k''} / \prod_k R_k^{v_k'}) \tag{3.24}$$

Now, equilibrium constant is defined as the ratio of the partial pressure:

$$K_e = \prod_k Q_k^{v_k''} / \prod_k R_k^{v_k'} \tag{3.25}$$

Rearranging, the equilibrium constant equation becomes:

$$K_e = exp\left(-\frac{\Delta G^o}{RT}\right) \qquad (3.26)$$

From Equations (3.26) and (3.22), it can be concluded that equilibrium constant K_e is a function of temperature only. Therefore, equilibrium constants of formation for different sets of reactions can be calculated based on the temperature. Equilibrium constants for different reactions are tabulated in NIST-JANNAF [35].

3.3.2 Finite Rate Chemical Reactions

Finite rate chemical reaction models provide the equations by integrating the time rate of change of the chemical compounds of the gases in the reactions. This implementation will cause different time scales to be present in the problem. In other words, it will cause equations to be rather stiff. Considering the difficultness and computational inefficiency of the stiff equations, extensive chemistry models are modified to be rather simple and computationally feasible [33].

System of chemical reactions in the finite rate chemistry models can be written in the general form as in Equation (3.27). The equation is written for the K number of species and total reaction numbers of I.

$$\sum_{k=1}^{K} v'_{k,i}\chi_k \ \rightleftarrows \ \sum_{k=1}^{K} v''_{k,i}\chi_k \qquad (3.27)$$

where $v'_{k,i}$ shows the reactant's stoichiometric coefficient of the kth species in the ith reaction and $v''_{k,i}$ shows the product's stoichiometric coefficient of the kth species in the ith reaction. And, χ_k is the symbol for the kth species chemical representation.

According to law of the mass action, in each forward reaction, any change in reactants concentration will cause proportional change in the products concentration. This law makes it possible to find the reaction rates as constants using Arrhenius which

depends primarily on temperature. The Arrhenius expression to calculate the forward reaction rate is given in Equation (3.28)

$$k_{f,i} = A_i T^{B_i} \exp\left(-\frac{E_i}{R_u T}\right) \tag{3.28}$$

where A_i is the rate constant of reaction i, B_i is the temperature exponent and E_i is the activation energy for ith reaction. Values of A, B and E are found from the experiments.

If the constant values are available, the backward reaction rates can also be computed using Arrhenius formula like the forward reaction calculation. However, if these data are not available as for most cases, backward reaction rate constant can be calculated using the equilibrium constant which explained previously and reproduced after expanding it as in Equation (3.29).

$$K_e = exp\left(\left(\frac{\Delta S_i}{R} - \frac{\Delta H_i}{RT}\right)\left(\frac{p_{atm}}{RT}\right)^{\Sigma_{k=1}^{K} v'_{k,i}}\right) \tag{3.29}$$

In this case, backward reaction rate is related to the forward reaction rate constant as well as equilibrium constant.

$$k_{b,i} = \frac{k_{f,i}}{K_{e,i}} \tag{3.30}$$

Source terms for different species $\dot{\omega}_k$ in Equation (3.6) shows the production rate of kth species in a cell produced by chemical reactions occurring. In addition, the rate of change of species concentration is calculated by addition of each species concentration from different reactions. As a result, rate of the production of species which is called source term or production term of chemical reactions is found as:

$$\dot{\omega}_k = W_k \sum_{k=1}^{K} \left(v''_{k,i} - v'_{k,i}\right)\left(k_{fi} \prod_{k=1}^{K} [\chi_k]^{v'_{k,i}} - k_{bi} \prod_{k=1}^{K} [\chi_k]^{v''_{k,i}}\right) \tag{3.31}$$

where, χ_k is the molar concentration and W_k is the molecular weight of kth species. Also, K is the total number of species and i is the number of reactions used in modelling of the chemical reaction mechanism.

3.3.3 Fuel Types

Fuel selection is one of the important parameters in designing the propulsion systems. Besides to its effect in engine performance, it has great effect in the design of the vehicle. For instance, choosing a fuel with higher density will occupy less volume in the vehicle and so will increase the room available for other parts such as payload areas and etc. Therefore, fuel should be selected not only to provide good performance and efficiency for the engine but also, to increase the engine's application potential [36].

Throughout years, several fuels have been tested to be used in scramjets. Among those fuels, hydrogen and hydrocarbon fuels are used extensively. Fry [4] shows that for flight Mach numbers above 8, hydrogen fuels are beneficial. On the other hand, for scramjet powered flight Mach numbers below 8, hydrocarbon fuels should be preferred which can be seen from Figure 3.1. However, in a study of Waltrup [37], it is concluded that hydrocarbon fuels can have better performance than hydrogen fuels up to Mach numbers of 10. Certainty of the efficiency of hydrogen in high Mach numbers above 10 is due to its fast reaction rate and cooling capacity compared to hydrocarbons.

Overall, hydrogen fuels have the advantages of fast burning, short ignition delay time and high cooling capacity. However, its low density and requirement for large fuel tank area are disadvantageous. Unlikely, hydrocarbon fuels are advantageous because of high density (require less volume), easy handling (not highly reactive) and more energy per volume. Hydrocarbon fuel have disadvantages of slow reaction and long ignition delay time [38], [39].

28
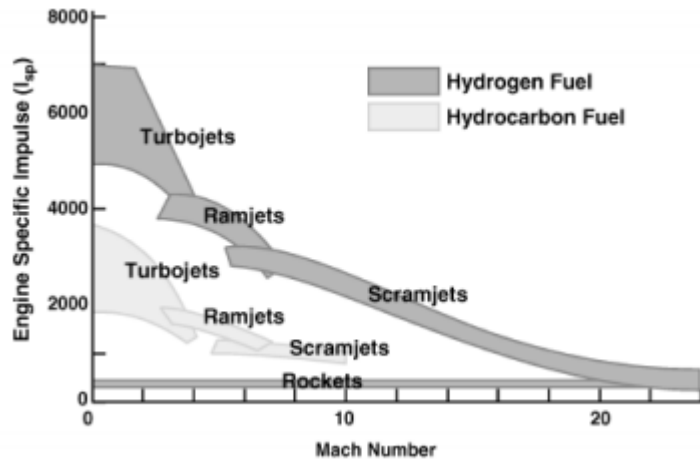
Figure 3.1 Comparison of Fuel Types at Different Mach Numbers [4]

Considering hydrocarbon fuels, ethylene and methane are the two most studied fuels. Since methane has slow kinetics, it possesses less stable regions in the combustion [40], [41]. Thus, ethylene becomes a better option among hydrocarbon fuels. Generally, hydrogen and ethylene are the most preferred and studied fuels in scramjets. Since in this study scramjet is considered for low hypersonic flows (Mach numbers below 8), ethylene is employed as the fuel for the scramjet engine analysis. Details of the ethylene-air combustion properties are given below.

3.3.4 Ethylene-Air Combustion Model

Hydrocarbon fuel systems generally have complex mechanisms. Hydrocarbon fuels with large carbon compositions in their molecules have extensive reaction mechanisms and solving these systems require high computation time and effort. For instance, detailed reaction mechanism for ethylene has been studied with 148 basic reactions [42]. Therefore, reduced ethylene reaction mechanisms are necessary considering the computational efficiency. Several studies are done to simplify and reduce the system of reactions for hydrocarbon fuels especially ethylene [6].

Varatharajan and Williams [42] used steady-state assumption along with partial-equilibrium approximation to reduce the number of reaction steps from 148 to

38 steps. Further, by restricting reactions just to induction period, these reactions can be reduced to 12 elementary reactions. Regarding these 12 elementary reactions, there exists hydroxyl (OH) among the species present in reactions. Hydroxyl is found to decrease the ignition delay time. Therefore reduced reaction models which use hydroxyl in their reactions, are not able to predict the ignition delay time [43]. Baurle and Eklund reduced the reaction mechanism to 3 steps by adjusting the reactions rate for the absence of the hydroxyl in their reaction mechanism [9]. This reduced finite rate chemical reaction model for Ethylene ignition with 3 reactions and 6 species which is shown in Table 3.1 is used in this study.

Table 3.1 Forward Reaction Rate Data for Reduced Ethylene-Air Combustion [9]

Reactions	A_f	B_f	$\dfrac{E_f}{R}$
$C_2H_4 + O_2 \rightleftarrows 2CO + 2H_2$	2.10×10^{14}	0.0	18015.3
$2CO + O_2 \rightleftarrows 2CO_2$	3.48×10^{11}	2.0	10134.9
$2H_2 + O_2 \rightleftarrows 2H_2O$	3.00×10^{20}	-1.0	0.0

CHAPTER 4

COMPUTATIONAL MODELING

Basic principle of Computational Fluid Dynamics (CFD) is to model flows as realistic as possible. However, there are many obstacles to accomplish this goal. In order to model the fluid motion precisely, solution of the complex equations are needed for complex problems. These models require high computation time and very large computers. Therefore, solving these complex equations becomes inefficient both computationally and economically. For this purpose, lots of research are done to get better solutions with rather simplified equations and reduced CPU times. Numerical algorithms and methods are developed to solve the flow problems accurately with less computation time i.e. to reach the goal of accurate modelling with efficient computation process.

In this study, the coupled equations of Navier-Stokes and finite rate chemical reactions are solved. In order to have efficient computation, computational space is transformed from Cartesian coordinates to generalized coordinates. Moreover, different flux splitting methods are introduced to the solution algorithm. First and second order schemes are presented with the addition of flux limiters for second order scheme. Moreover, Implementation of Newton GMRES method is explained.

4.1 Navier-Stokes Equations in Cartesian Coordinates

Three dimensional steady coupled equations of Navier-Stokes and finite rate chemistry model equations can be written in vector form in the generalized coordinate as Equation (4.1). Flux vectors are divided into convective (inviscid) and viscous fluxes for better representations of the flow physics and simplifying the equations for the numerical approach.

31

$$\frac{\partial(F_c - F_v)}{\partial x} + \frac{\partial(G_c - G_v)}{\partial y} + \frac{\partial(H_c - H_v)}{\partial z} - S = 0 \qquad (4.1)$$

where F_c, G_c and H_c are inviscid (convective) flux vectors and F_v, G_v and H_v are viscous flux vectors in x, y and z-direction, respectively. Moreover, S is the source vector for species. This equation obtained from Equations (3.1) to (3.6).

Aforementioned convective flux vectors are given as:

$$F_c = \begin{bmatrix} \rho u \\ \rho u^2 + p \\ \rho uv \\ \rho uw \\ (\rho e_t + p)u \\ \rho_1 u \\ \vdots \\ \rho_{K-1} u \end{bmatrix} \qquad G_c = \begin{bmatrix} \rho v \\ \rho uv \\ \rho v^2 + p \\ \rho vw \\ (\rho e_t + p)v \\ \rho_1 v \\ \vdots \\ \rho_{K-1} v \end{bmatrix} \qquad H_c = \begin{bmatrix} \rho w \\ \rho uw \\ \rho vw \\ \rho w^2 + p \\ (\rho e_t + p)w \\ \rho_1 w \\ \vdots \\ \rho_{K-1} w \end{bmatrix} \qquad (4.2)$$

where, u, v and w are velocity components. In addition, $\rho_1, \dots, \rho_{K-1}$ corresponds to density of the kth species presented in reactive flow where K is the total number of species. In order to reduce the computation time, the conservation of mass equation for one of the species is removed. This is possible because of the fact that summation of all of the densities should be equal to the total density of the flow and since total density is also introduced to the equation, one of the species' density can be removed from the equations to reduce the size of the vector. In other words, independent species is one less than the total number of species.

Viscous flux vectors are written as [44]:

$$F_v = \begin{bmatrix} 0 \\ \tau_{xx} \\ \tau_{xy} \\ \tau_{xz} \\ u\tau_{xx} + v\tau_{xy} + w\tau_{xz} \\ 0 \\ \vdots \\ 0 \end{bmatrix} \qquad G_v = \begin{bmatrix} 0 \\ \tau_{xy} \\ \tau_{yy} \\ \tau_{yz} \\ u\tau_{xy} + v\tau_{yy} + w\tau_{yz} \\ 0 \\ \vdots \\ 0 \end{bmatrix} \qquad (4.3)$$

$$H_v = \begin{bmatrix} 0 \\ \tau_{xz} \\ \tau_{yz} \\ \tau_{zz} \\ u\tau_{xz} + v\tau_{yz} + w\tau_{zz} \\ 0 \\ \vdots \\ 0 \end{bmatrix} \qquad S = \begin{bmatrix} 0 \\ 0 \\ 0 \\ 0 \\ 0 \\ \dot{\omega}_1 \\ \vdots \\ \dot{\omega}_{K-1} \end{bmatrix} \tag{4.4}$$

where $\dot{\omega}$ is the production term for the species and τ is the shear stress which can be defined as:

$$\tau_{xx} = \frac{2}{3}\mu(2\frac{\partial u}{\partial x} - \frac{\partial v}{\partial y} - \frac{\partial w}{\partial z})$$

$$\tau_{yy} = \frac{2}{3}\mu(2\frac{\partial v}{\partial y} - \frac{\partial u}{\partial x} - \frac{\partial w}{\partial z}) \tag{4.5}$$

$$\tau_{zz} = \frac{2}{3}\mu(2\frac{\partial w}{\partial z} - \frac{\partial u}{\partial x} - \frac{\partial v}{\partial y})$$

$$\tau_{xy} = \mu\left(\frac{\partial u}{\partial y} + \frac{\partial v}{\partial x}\right) \qquad \tau_{xz} = \mu\left(\frac{\partial w}{\partial x} + \frac{\partial u}{\partial z}\right) \qquad \tau_{yz} = \mu\left(\frac{\partial v}{\partial z} + \frac{\partial w}{\partial y}\right) \tag{4.6}$$

where μ is the dynamic viscosity of the fluid. Since the system of equations are not closed, one more equation comes from the equation of state for pressure as:

$$p = \rho(\gamma - 1)\left[e - \frac{\rho}{2}(u^2 + v^2 + w^2)\right] \tag{4.7}$$

4.2 Transformation Metrics

Transformation from physical to computational space increases the efficiency and accuracy of the computations and makes the implementation of the boundary conditions easier. To solve the governing equations in computational domain,

equations should be transformed from physical space. Computational domain is an equally sized grid system within a rectangular shape.

Here, generalized coordinate transformation is applied to governing equations. Equations of motion are intended to be transformed from physical domain (x, y, z) into computational space (ξ, η, ζ). Transformation is done using the following equations:

$$\xi = \xi(x, y, z)$$

$$\eta = \eta(x, y, z) \tag{4.8}$$

$$\zeta = \zeta(x, y, z)$$

Relation between partial derivatives in physical space with computational domain is derived by the chain rule as:

$$\frac{\partial}{\partial x} = \xi_x \frac{\partial}{\partial \xi} + \eta_x \frac{\partial}{\partial \eta} + \zeta_x \frac{\partial}{\partial \zeta}$$

$$\frac{\partial}{\partial y} = \xi_y \frac{\partial}{\partial \xi} + \eta_y \frac{\partial}{\partial \eta} + \zeta_y \frac{\partial}{\partial \zeta} \tag{4.9}$$

$$\frac{\partial}{\partial z} = \xi_z \frac{\partial}{\partial \xi} + \eta_z \frac{\partial}{\partial \eta} + \zeta_z \frac{\partial}{\partial \zeta}$$

where, $\xi_x, \eta_x, \zeta_x, \xi_y, \eta_y, \zeta_y, \xi_z, \eta_z, \zeta_z$ are the metrics of the transformation. Since determination of metrics are impossible in some cases, metrics should be computed numerically. Differential expression in generalized coordinates can be written as:

$$\partial\xi = \xi_x dx + \xi_y dy + \xi_z dz$$

$$\partial\eta = \eta_x dx + \eta_y dy + \eta_z dz \tag{4.10}$$

$$\partial\zeta = \zeta_x dx + \zeta_y dy + +\zeta_z dz$$

Writing these in a matrix form:

$$\begin{bmatrix} \partial\xi \\ \partial\eta \\ \partial\zeta \end{bmatrix} = \begin{bmatrix} \xi_x & \xi_y & \xi_z \\ \eta_x & \eta_y & \eta_z \\ \zeta_x & \zeta_y & \zeta_z \end{bmatrix} \begin{bmatrix} dx \\ dy \\ dz \end{bmatrix} \tag{4.11}$$

Changing independent variables of generalized coordinates to Cartesian coordinates, new matrix can be formed as:

$$\begin{bmatrix} dx \\ dy \\ dz \end{bmatrix} = \begin{bmatrix} x_\xi & x_\eta & x_\zeta \\ y_\xi & y_\eta & y_\zeta \\ z_\xi & z_\eta & z_\zeta \end{bmatrix} \begin{bmatrix} \partial\xi \\ \partial\eta \\ \partial\zeta \end{bmatrix} \tag{4.12}$$

Comparing Equations (4.11) and (4.12), it can be concluded that:

$$\begin{bmatrix} \xi_x & \xi_y & \xi_z \\ \eta_x & \eta_y & \eta_z \\ \zeta_x & \zeta_y & \zeta_z \end{bmatrix} = \begin{bmatrix} x_\xi & x_\eta & x_\zeta \\ y_\xi & y_\eta & y_\zeta \\ z_\xi & z_\eta & z_\zeta \end{bmatrix}^{-1} \tag{4.13}$$

The Jacobian of the transformation is defined as:

$$J = \frac{\partial(\xi,\eta,\zeta)}{\partial(x,y,z)} = \begin{vmatrix} \xi_x & \xi_y & \xi_z \\ \eta_x & \eta_y & \eta_z \\ \zeta_x & \zeta_y & \zeta_z \end{vmatrix}$$

$$\frac{1}{J} = \frac{\partial(x,y,z)}{\partial(\xi,\eta,\zeta)} = \begin{vmatrix} x_\xi & x_\eta & x_\zeta \\ y_\xi & y_\eta & y_\zeta \\ z_\xi & z_\eta & z_\zeta \end{vmatrix} \tag{4.14}$$

Therefore, the equation for Jacobian of the transformation can be written as:

$$J = \frac{1}{x_\xi\left(y_\eta z_\zeta - y_\zeta z_\eta\right) - x_\eta\left(y_\xi z_\zeta - y_\zeta z_\xi\right) + x_\zeta\left(y_\xi z_\eta - y_\eta z_\xi\right)} \tag{4.15}$$

As a result, metrics essential for the transformation from body-fitted space to computational space are found as follows:

$$\xi_x = J\left(y_\eta z_\zeta - y_\zeta z_\eta\right) \quad \xi_y = J\left(x_\zeta z_\eta - x_\eta z_\zeta\right) \quad \xi_z = J\left(x_\eta y_\zeta - x_\zeta y_\eta\right)$$

$$\eta_x = J\left(y_\zeta z_\xi - y_\xi z_\zeta\right) \quad \eta_y = J\left(x_\xi z_\zeta - x_\zeta z_\xi\right) \quad \eta_z = J\left(x_\zeta y_\xi - x_\xi y_\zeta\right) \quad (4.16)$$

$$\zeta_x = J\left(y_\xi z_\eta - y_\eta z_\xi\right) \quad \zeta_y = J\left(x_\eta z_\xi - x_\xi z_\eta\right) \quad \zeta_z = J\left(x_\xi y_\eta - x_\eta y_\xi\right)$$

4.3 Non-Dimensionalization of Governing Equations

Equations of motion for fluid flows can be non-dimensionalized in order to simplify the equations. In non-dimensionalized equations, units for measuring the parameters become unimportant. Therefore, different flow analysis can be implemented in an efficient way using these equation. Non-dimensionalizing of the Navier-Stokes equations are done by defining the reference parameters as:

$$x^* = \frac{x}{L} \qquad y^* = \frac{y}{L} \qquad z^* = \frac{z}{L} \qquad V_{ref} = \left(\frac{p_\infty}{\rho_\infty}\right)^{1/2}$$

$$u^* = \frac{u}{V_{ref}} = \frac{u}{(p_\infty/\rho_\infty)^{1/2}} \quad v^* = \frac{v}{(p_\infty/\rho_\infty)^{1/2}} \quad w^* = \frac{w}{(p_\infty/\rho_\infty)^{1/2}} \quad (4.17)$$

$$\rho^* = \frac{\rho}{\rho_\infty} \quad p^* = \frac{p}{p_\infty} \quad \mu^* = \frac{\mu}{\mu_\infty} \quad e_t^* = \frac{e_t}{(p_\infty/\rho_\infty)}$$

where L represents the length of the vehicle and subscript ∞ shows the free stream values. The non-dimensionalized parameters is defined as Reynolds number in the following equation:

$$Re = \frac{\rho_{ref} V_{ref} L}{\mu_{ref}} = \frac{\rho_\infty \left(\frac{p_\infty}{\rho_\infty}\right)^{\frac{1}{2}} L}{\mu_\infty} \qquad (4.18)$$

Considering the equations below,

$$\frac{p_\infty}{\rho_\infty} = RT_\infty \qquad \gamma \frac{p_\infty}{\rho_\infty} = \gamma RT_\infty \qquad (\gamma = constant)$$

$$a_\infty = \frac{V_\infty}{M_\infty} = (\gamma RT_\infty)^{1/2} = \left(\gamma \frac{p_\infty}{\rho_\infty}\right)^{1/2}$$

(4.19)

where γ is the specific heat ratio and a is the speed of sound. Using Equations (4.19), the equation for Reynolds number becomes as:

$$Re = \frac{\rho_\infty \left(\frac{p_\infty}{\rho_\infty}\right)^{\frac{1}{2}} L}{\mu_\infty} = \frac{\rho_\infty \left(\frac{V_\infty}{\sqrt{\gamma} M_\infty}\right) L}{\mu_\infty} = \frac{1}{\sqrt{\gamma} M_\infty}\left(\frac{\rho_\infty V_\infty L}{\mu_\infty}\right)$$

(4.20)

Reynolds number in terms of independent variables can be written as:

$$Re = \frac{1}{\sqrt{\gamma} M_\infty} Re_\infty$$

(4.21)

Using the non-dimensional parameters described, the equations of motion for steady flows are non-dimensionalized as:

Conservation of mass:

$$\frac{\partial}{\partial x^*}(\rho^* u^*) + \frac{\partial}{\partial y^*}(\rho^* u^*) + \frac{\partial}{\partial z^*}(\rho^* w^*) = 0$$

(4.22)

Momentum in the x-direction:

$$\frac{\partial}{\partial x^*}\left(\rho^* u^{*2} + p^*\right) + \frac{\partial}{\partial y^*}(\rho^* u^* v^*) + \frac{\partial}{\partial z^*}(\rho^* u^* w^*) =$$

$$\frac{\partial}{\partial x^*}(\tau_{xx}^*) + \frac{\partial}{\partial y^*}(\tau_{xy}^*) + \frac{\partial}{\partial z^*}(\tau_{xz}^*)$$

(4.23)

Momentum in y-direction:

$$\frac{\partial}{\partial x^*}(\rho^* u^* v^*) + \frac{\partial}{\partial y^*}(\rho^* v^{*2} + p^*) + \frac{\partial}{\partial z^*}(\rho^* v^* w^*) =$$

$$\frac{\partial}{\partial x^*}(\tau_{xy}^*) + \frac{\partial}{\partial y^*}(\tau_{yy}^*) + \frac{\partial}{\partial z^*}(\tau_{yz}^*) \tag{4.24}$$

Momentum in the z-direction:

$$\frac{\partial}{\partial x^*}(\rho^* u^* w^*) + \frac{\partial}{\partial y^*}(\rho^* v^* w^*) + \frac{\partial}{\partial z^*}(\rho^* w^{*2} + p^*) =$$

$$\frac{\partial}{\partial x^*}(\tau_{xz}^*) + \frac{\partial}{\partial y^*}(\tau_{yz}^*) + \frac{\partial}{\partial z^*}(\tau_{zz}^*) \tag{4.25}$$

Conservation of Energy:

$$\frac{\partial}{\partial x^*}(\rho^* u^* e_t^* + p^* u^*) + \frac{\partial}{\partial y^*}(\rho^* v^* e_t^* + p^* v^*) + \frac{\partial}{\partial z^*}(\rho^* w^* e_t^* + p^* w^*)$$

$$= \frac{\partial}{\partial x^*}(u^* \tau_{xx}^* + v^* \tau_{xy}^* + w^* \tau_{xz}^*) + \frac{\partial}{\partial y^*}(u^* \tau_{xy}^* + v^* \tau_{yy}^* + w^* \tau_{yz}^*) \tag{4.26}$$

$$+ \frac{\partial}{\partial z^*}(u^* \tau_{xz}^* + v^* \tau_{yz}^* + w^* \tau_{zz}^*)$$

Conservation of mass for species:

$$\frac{\partial}{\partial x^*}(\rho_k^* u^*) + \frac{\partial}{\partial y^*}(\rho_k^* v^*) + \frac{\partial}{\partial z^*}(\rho_k^* w^*) = \dot{\omega}_k^* \tag{4.27}$$

where, shear stresses are non-dimensionalized in the following equations:

$$\tau_{xx}^* = \frac{\sqrt{\gamma} M_\infty}{Re_\infty}\left(2\mu^* \frac{\partial u^*}{\partial x^*} - \lambda^* \nabla^*.\vec{V}^*\right)$$

$$\tau_{yy}^* = \frac{\sqrt{\gamma} M_\infty}{Re_\infty}\left(2\mu^* \frac{\partial v^*}{\partial y^*} - \lambda^* \nabla^*.\vec{V}^*\right) \tag{4.28}$$

$$\tau_{zz}^* = \frac{\sqrt{\gamma} M_\infty}{Re_\infty}\left(2\mu^* \frac{\partial w^*}{\partial z^*} - \lambda^* \nabla^*.\vec{V}^*\right)$$

$$\tau_{xy}^* = \mu^* \left(\frac{\partial u^*}{\partial y^*} + \frac{\partial v^*}{\partial x^*} \right) \qquad \tau_{xz}^* = \mu^* \left(\frac{\partial w^*}{\partial x^*} + \frac{\partial u^*}{\partial z^*} \right)$$

$$\tau_{yz}^* = \mu^* \left(\frac{\partial v^*}{\partial z^*} + \frac{\partial w^*}{\partial y^*} \right)$$

(4.29)

From now on, the superscript * is dropped for the sake of brevity. The Navier-Stokes equations are represented in non-dimensional form in the following section.

4.4 Navier-Stokes Equations in Generalized Coordinates

The non-dimensionalized Navier-Stokes equations in Cartesian coordinates derived as in Equations (4.22) to (4.27), are transformed into generalized coordinates, here. Metrics of transformations found in the previous sections are used to perform this transformation.

Applying the transformations in Equation (4.9) into Equation (4.1), Navier-Stokes equations are found in conservative form and in generalized coordinates as follows:

$$\frac{\partial (\hat{F}_c - \hat{F}_v)}{\partial \xi} + \frac{\partial (\hat{G}_c - \hat{G}_v)}{\partial \eta} + \frac{\partial (\hat{H}_c - \hat{H}_v)}{\partial \zeta} - \hat{S} = 0 \qquad (4.30)$$

Where inviscid and viscous flux vectors can be defined as:

$$\hat{F}_c = \frac{1}{J} \left(\xi_x F_c + \xi_y G_c + \xi_z H_c \right) \qquad \hat{F}_v = \frac{1}{J} \left(\xi_x F_v + \xi_y G_v + \xi_z H_v \right)$$

$$\hat{G}_c = \frac{1}{J} \left(\eta_x F_c + \eta_y G_c + \eta_z H_c \right) \qquad \hat{G}_v = \frac{1}{J} \left(\eta_x F_v + \eta_y G_v + \eta_z H_v \right) \quad (4.31)$$

$$\hat{H}_c = \frac{1}{J} \left(\zeta_x F_c + \zeta_y G_c + \zeta_z H_c \right) \qquad \hat{H}_v = \frac{1}{J} \left(\zeta_x F_v + \zeta_y G_v + \zeta_z H_v \right)$$

Equation (4.30) can be expressed in vector form as follows:

$$\hat{F}_c = \frac{1}{J} \begin{bmatrix} \rho U \\ \rho U u + \xi_x p \\ \rho U v + \xi_y p \\ \rho U w + \xi_z p \\ (\rho e_t + p)U \\ \rho_1 U \\ \vdots \\ \rho_{K-1} U \end{bmatrix} \qquad \hat{G}_c = \frac{1}{J} \begin{bmatrix} \rho V \\ \rho V u + \eta_x p \\ \rho V v + \eta_y p \\ \rho V w + \eta_z p \\ (\rho e_t + p)V \\ \rho_1 V \\ \vdots \\ \rho_{K-1} V \end{bmatrix} \qquad \hat{H}_c = \frac{1}{J} \begin{bmatrix} \rho W \\ \rho W u + \zeta_x p \\ \rho W v + \zeta_y p \\ \rho W w + \zeta_z p \\ (\rho e_t + p)W \\ \rho_1 W \\ \vdots \\ \rho_{K-1} W \end{bmatrix} \qquad (4.32)$$

where, contravariant velocities are defined as:

$$U = \xi_x u + \xi_y v + \xi_z w$$

$$V = \eta_x u + \eta_y v + \eta_z w \qquad (4.33)$$

$$W = \zeta_x u + \zeta_y v + \zeta_z w$$

And, viscous flux vectors are written as

$$\hat{F}_v = \frac{1}{J} \begin{bmatrix} 0 \\ \xi_x \tau_{xx} + \xi_y \tau_{xy} + \xi_z \tau_{xz} \\ \xi_x \tau_{xy} + \xi_y \tau_{yy} + \xi_z \tau_{yz} \\ \xi_x \tau_{xz} + \xi_y \tau_{yz} + \xi_z \tau_{zz} \\ \xi_x b_x + \xi_y b_y + \xi_z b_z \\ 0 \\ \vdots \\ 0 \end{bmatrix} \qquad \hat{G}_v = \begin{bmatrix} 0 \\ \eta_x \tau_{xx} + \eta_y \tau_{xy} + \eta_z \tau_{xz} \\ \eta_x \tau_{xy} + \eta_y \tau_{yy} + \eta_z \tau_{yz} \\ \eta_x \tau_{xz} + \eta_y \tau_{yz} + \eta_z \tau_{zz} \\ \eta_x b_x + \eta_y b_y + \eta_z b_z \\ 0 \\ \vdots \\ 0 \end{bmatrix}$$

$$(4.34)$$

$$\hat{H}_v = \begin{bmatrix} 0 \\ \zeta_x \tau_{xx} + \zeta_y \tau_{xy} + \zeta_z \tau_{xz} \\ \zeta_x \tau_{xy} + \zeta_y \tau_{yy} + \zeta_z \tau_{yz} \\ \zeta_x \tau_{xz} + \zeta_y \tau_{yz} + \zeta_z \tau_{zz} \\ \zeta_x b_x + \zeta_y b_y + \zeta_z b_z \\ 0 \\ \vdots \\ 0 \end{bmatrix}$$

where,

$$b_x = u\tau_{xx} + v\tau_{xy} + w\tau_{xz} \qquad b_y = u\tau_{xy} + v\tau_{yy} + w\tau_{yz}$$

$$(4.35)$$

$$b_z = u\tau_{xz} + v\tau_{yz} + w\tau_{zz}$$

And, Shear stresses non-dimensionalized in Equations (4.28) and (4.29), can be written in tensor notation as follows:

$$\tau_{x_i x_j} = \frac{\sqrt{\gamma} M_\infty}{Re_\infty} \left[\mu \left(\frac{\partial u_i}{\partial x_j} + \frac{\partial u_j}{\partial x_i} \right) + \lambda \frac{\partial u_k}{\partial x_k} \delta_{ij} \right] \qquad (4.36)$$

where λ is the bulk viscosity which is related to the dynamic viscosity by the stokes hypothesis as in the equation below:

$$\lambda = -\frac{2}{3} \mu \qquad (4.37)$$

4.5 Numerical Discretization

Governing equations of fluid motion can be written in both differential and integral form and solved accordingly. The methods used to solve these equations have different characteristics. Therefore, methods which are advantageous for the problem and domain in question should be applied. In other words, there is no globally efficient method for different type of problems. Basic principle of numerical approximations is to divide the solution domain into discrete points, areas or volumes according to domain dimensions. In order to solve the differential form of the governing equations finite difference method (FDM) is generally utilized. Finite difference methods are accurate in computational domains which are divided by equally spaced points. Hence, implementation of finite difference equations for complex geometries with discontinuities will cause numerical problems. Whereas, finite element methods (FEM) and finite volume methods (FVM) attempt to solve the governing equations of fluid motion in their integral form. In order to use finite element method, the domain

of solution should be divided to finite number of elements where approximations are done by using interpolation function at each element. Unlike finite difference method, FEM can handle complex geometries with good accuracy. However, finite element methods require high CPU time for fluid flow problems [45]. In order to solve flow problems in complex geometries with less computational time, finite volume method is introduced.

4.5.1 Finite Volume Method

In finite volume method, discretization of the domain is done by dividing the solution domain into small (finite) volumes or cells. Then, integral form of the governing equations are applied to each volume. The goal is to approximate the flow variables defined at each cell in a way to approach the exact solution for which conservation laws are satisfied. Since conservation laws are stronger in integral form, it is physically intuitive to apply equations of motion in their integral form for complex flows. Therefore, finite volume method is promising method for flows with discontinuities such as shocks and complex geometries. The governing equations of fluid motion can be written in general integral form as in Equation (4.38):

$$\frac{\partial}{\partial t} \iiint_V Q dV + \iint_S \vec{f} . \vec{n} dS = 0 \qquad (4.38)$$

Where $\vec{f}$ is the net flux across the surface S and $\vec{n}$ is the normal of the surface. For steady flows as will be applied in this study:

$$\iint_S \vec{f} . \vec{n} dS = 0 \qquad (4.39)$$

In order to discretize the Equation (4.39), cell centered finite volume method is used. The principle of this scheme is to define the flow variables in the center of the finite volumes obtained by dividing the solution domain. Flux vectors are determined at the cell interfaces of the control volume. In order to evaluate the flux vectors,

42

conservation law is applied to the control volume. According to the conservation laws, the difference between the amount of flow entering and leaving the control volume is equal to flux generated in the control volume. Mathematically, conservation of flux vectors over a finite volume can be expressed as:

$$\hat{F}.\Delta\xi = \left(\hat{F}_c - \hat{F}_v\right)_{i+\frac{1}{2},j,k} - \left(\hat{F}_c - \hat{F}_v\right)_{i-\frac{1}{2},j,k}$$

$$\hat{G}.\Delta\eta = \left(\hat{G}_c - \hat{G}_v\right)_{i,j+\frac{1}{2},k} - \left(\hat{G}_c - \hat{G}_v\right)_{i,j-\frac{1}{2},k} \tag{4.40}$$

$$\hat{H}.\Delta\zeta = \left(\hat{H}_c - \hat{H}_v\right)_{i,j,k+\frac{1}{2}} - \left(\hat{H}_c - \hat{H}_v\right)_{i,j,k-\frac{1}{2}}$$

where $\hat{F}, \hat{G}$ and $\hat{H}$ are the amount of fluxes generated in a control volume with dimensions of $\Delta\xi, \Delta\eta$ and $\Delta\zeta$.

Consequently, the governing equations presented in generalized coordinates in Equation (4.30) can be discretized as Equation (4.41):

$$\frac{\partial_\xi \left(\hat{F}_c - \hat{F}_v\right)}{\Delta\xi} + \frac{\partial_\eta \left(\hat{G}_c - \hat{G}_v\right)}{\Delta\eta} + \frac{\partial_\zeta \left(\hat{H}_c - \hat{H}_v\right)}{\Delta\zeta} - \hat{S} = 0 \tag{4.41}$$

For convenience, the equally spaced dimensions of the computational domain are set to be 1.

$$\Delta\xi = \xi_{i+\frac{1}{2},j,k} - \xi_{i-\frac{1}{2},j,k} = 1$$

$$\Delta\eta = \eta_{i,j+\frac{1}{2},k} - \eta_{i,j-\frac{1}{2},k} = 1 \tag{4.42}$$

$$\Delta\zeta = \zeta_{i,j,k+\frac{1}{2}} - \zeta_{i,j,k-\frac{1}{2}} = 1$$

Considering the aforementioned equations, discretized equation becomes:

$$\left(\hat{F}_c - \hat{F}_v\right)_{i+\frac{1}{2},j,k} - \left(\hat{F}_c - \hat{F}_v\right)_{i-\frac{1}{2},j,k}$$

$$+\left(\hat{G}_c - \hat{G}_v\right)_{i,j+\frac{1}{2},k} - \left(\hat{G}_c - \hat{G}_v\right)_{i,j-\frac{1}{2},k} \qquad (4.43)$$

$$+\left(\hat{H}_c - \hat{H}_v\right)_{i,j,k+\frac{1}{2}} - \left(\hat{H}_c - \hat{H}_v\right)_{i,j,k-\frac{1}{2}} - \hat{S}_{i,j,k} = 0$$

Since source term for chemical reactions is included in the flow variables vector, where they are computed in the cell centers, this term is not discretized.

4.6 Flux Vector Splitting Methods

Solving the semi-discrete equation needs the values of fluxes at cell faces. Since flux values are highly important in the computation process, different methods are developed to enhance the flux calculation. The goal is to improve the solutions approximation by acquiring the flow variables from the neighboring cells to the left and right of the cell interface and reach its exact solution. In this study, flux calculations will be done using upwind scheme.

Inviscid flux calculation is done by applying the flux balance for each cell of the solution domain as:

$$\left(\delta_\xi \hat{F}_c\right)_{i,j,k} = \left(\hat{F}_c\right)_{i+\frac{1}{2},j,k} - \left(\hat{F}_c\right)_{i-\frac{1}{2},j,k} \qquad (4.44)$$

where δ_ξ denotes the difference operator. The evaluation of flux values at cell faces $(i + \frac{1}{2}, i - \frac{1}{2})$ is done by using the flow variables from the neighboring cells. The flow variables used in the interface flux calculation are from the cells to the right and left of that interface as:

$$\left(\hat{F}_c\right)_{i+\frac{1}{2},j,k} = \hat{F}_c^+\left(\hat{Q}^-\right)_{i+\frac{1}{2},j,k} + \hat{F}_c^-\left(\hat{Q}^+\right)_{i+\frac{1}{2},j,k}$$

$$\qquad (4.45)$$

$$\left(\hat{F}_c\right)_{i-\frac{1}{2},j,k} = \hat{F}_c^+\left(\hat{Q}^-\right)_{i-\frac{1}{2},j,k} + \hat{F}_c^-\left(\hat{Q}^+\right)_{i-\frac{1}{2},j,k}$$

where $\hat{F}_c^+$ transfer information from the cell which is to the left of the interface i.e. information is spread from left to right and $\hat{Q}^-$ are the flow variables defined at the cell center in the left side of the interface. However, $\hat{F}_c^-$ brings information of flow variables from the cell in the right side of the interface. The flow variables at the cell center to the right of the interface are denoted by $\hat{Q}^+$. The inviscid flux vectors of $\hat{G}_c$ and $\hat{H}_c$ can be discretized similarly as $\hat{F}_c$ which is shown in Equation (4.44). Therefore, upwind flux vector splitting applied to the inviscid fluxes of the semi-discrete governing equations shown in Equation (4.43) can be written as:

$$
\begin{aligned}
&\left[\hat{F}_c^+(\hat{Q}^-)_{i+\frac{1}{2},j,k} + \hat{F}_c^-(\hat{Q}^+)_{i+\frac{1}{2},j,k}\right] - \left[\hat{F}_c^+(\hat{Q}^-)_{i-\frac{1}{2},j,k} + \hat{F}_c^-(\hat{Q}^+)_{i-\frac{1}{2},j,k}\right] \\
&+ \left[\hat{G}_c^+(\hat{Q}^-)_{i,j+\frac{1}{2},k} + \hat{G}_c^-(\hat{Q}^+)_{i,j+\frac{1}{2},k}\right] - \left[\hat{G}_c^+(\hat{Q}^-)_{i,j-\frac{1}{2},k} + \hat{G}_c^-(\hat{Q}^+)_{i,j-\frac{1}{2},k}\right] \\
&+ \left[\hat{H}_c^+(\hat{Q}^-)_{i,j,k+\frac{1}{2}} + \hat{H}_c^-(\hat{Q}^+)_{i,j,k+\frac{1}{2}}\right] - \left[\hat{H}_c^+(\hat{Q}^-)_{i,j,k-\frac{1}{2}} + \hat{H}_c^-(\hat{Q}^+)_{i,j,k-\frac{1}{2}}\right] \\
&- \hat{S}_{i,j,k} = 0
\end{aligned}
\tag{4.46}
$$

There are several methods developed for splitting flux vectors. Steger-Warming, Van leer and AUSM methods are some of the most used flux vector splitting methods which are introduced in this study.

4.6.1 Steger-Warming Method

Steger-Warming flux vector splitting method was first introduced by Steger and Warming [46] in 1981. It is one of the most used flux splitting methods. In this method, the splitting of flux vector is done by splitting the eigenvalues of the Jacobian matrix of the flux vector.

$$
\lambda_1 = u \qquad \lambda_2 = u + a \qquad \lambda_3 = u - a
\tag{4.47}
$$

The eigenvalues of the Jacobian matrix is split according to its sign .The split eigenvalues of the Euler equations are defined as in the following equations.

$$\lambda_1^\pm = \frac{u \pm |u|}{2}$$

$$\lambda_2^\pm = \frac{(u+a) \pm |u+a|}{2} \qquad \lambda_3^\pm = \frac{(u-a) \pm |u-a|}{2}$$

(4.48)

Now that the eigenvalues are split, flux vector splitting is done according to these eigenvalues and the flux vector is written as in the Equation (4.49). Eigenvalues with the plus and minus sign are always positive and negative values, respectively.

$$\hat{F}_c^\pm = \frac{\rho}{2\gamma} \begin{bmatrix} \beta \\ \beta u + a(\lambda_2^\pm - \lambda_3^\pm)\hat{\xi}_x \\ \beta v + a(\lambda_2^\pm - \lambda_3^\pm)\hat{\xi}_y \\ \beta w + a(\lambda_2^\pm - \lambda_3^\pm)\hat{\xi}_z \\ \beta \frac{(u^2+v^2+w^2)}{2} + aU(\lambda_2^\pm - \lambda_3^\pm) + \frac{a^2(\lambda_2^\pm - \lambda_3^\pm)}{\gamma - 1} \\ \beta(\rho_1/\rho) \\ \vdots \\ \beta(\rho_{K-1}/\rho) \end{bmatrix}$$

(4.49)

where,

$$\beta = 2(\gamma - 1)\lambda_1^\pm + \lambda_2^\pm + \lambda_3^\pm$$

(4.50)

Split of flux vectors in other directions ($\hat{G}_c^\pm$ and $\hat{H}_c^\pm$) according to Steger-Warming flux splitting method can be found in Appendix B.

4.6.2 Van Leer Method

Steger-Warming method is one the well-known flux splitting schemes that is commonly used. Steger-Warming scheme uses eigenvalues of the Jacobian to split the flux vector. However, splitting by eigenvalues cause discontinuities at stagnation points and in sonic conditions. In other words, non-differentiable fluxes are generated in this method. To overcome this issue, Bram Van Leer [47] introduced a new upwind flux vector splitting method which uses Mach number for splitting the flux vector. In

Van leer method, Mach number is discretized into two regions of subsonic and supersonic regions. Detailed Mach number discretization is presented as:

$$M^+ = \begin{cases} 0 & M \leq -1 \\ \left(\dfrac{M+1}{2}\right)^2 & -1 < M < 1 \\ M & M \geq 1 \end{cases}$$

$$M^- = \begin{cases} M & M \leq -1 \\ -\left(\dfrac{M+1}{2}\right)^2 & -1 < M < 1 \\ 0 & M \geq 1 \end{cases}$$

(4.51)

As it can be understood from the Equation (4.51). Mach number value is propagated downstream for flows in locally supersonic region while in subsonic flows, Mach number is propagated both in upstream and downstream direction. As a result, flux vectors can be split with ease in supersonic regions as in Equation (4.52).

$$\begin{aligned} \hat{F}_c^+ = \hat{F}_c \ , \quad \hat{F}_c^- = 0 \qquad & M \geq 1 \\ \hat{F}_c^+ = 0 \ , \quad \hat{F}_c^- = \hat{F}_c \qquad & M \leq -1 \end{aligned}$$

(4.52)

Unlike supersonic flows regions, flux vector splitting in locally subsonic flow region requires more computation effort. For locally subsonic regions, flux vectors can be written for inviscid fluxes as (ξ-direction):

$$\hat{F}_c^{\pm} = \pm \frac{\rho a}{J}\left(\frac{M \pm 1}{2}\right)^2 \begin{bmatrix} 1 \\ \dfrac{1}{\gamma}\left(-\hat{U}_\xi \pm 2a\right)\hat{\xi}_x + u \\ \dfrac{1}{\gamma}\left(-\hat{U}_\xi \pm 2a\right)\hat{\xi}_y + u \\ \dfrac{1}{\gamma}\left(-\hat{U}_\xi \pm 2a\right)\hat{\xi}_z + u \\ \dfrac{\hat{U}_\xi\left(-\hat{U}_\xi \pm 2a\right)}{\gamma + 1} + \dfrac{2a}{\gamma^2 - 1} + \dfrac{u^2 + v^2 + w^2}{2} \\ \rho_1/\rho \\ \vdots \\ \rho_{K-1}/\rho \end{bmatrix}$$

(4.53)

where J is the Jacobian Matrix, a is the speed of sound and γ is the specific heat ratio. Contravariant Mach number $\widehat{U}$ with the direction cosines of $\hat{\xi}_x, \hat{\xi}_y, \hat{\xi}_z, \hat{\eta}_x, \dots, \hat{\zeta}_z$ are defined in the following equations in their general form as:

$$\hat{\xi}_i = \frac{\xi_i}{\sqrt{\xi_x^2 + \xi_y^2 + \xi_z^2}}$$

$$\tag{4.54}$$

$$\hat{\eta}_i = \frac{\eta_i}{\sqrt{\eta_x^2 + \eta_y^2 + \eta_z^2}} \qquad \hat{\zeta}_i = \frac{\zeta_i}{\sqrt{\zeta_x^2 + \zeta_y^2 + \zeta_z^2}}$$

$$\widehat{U}_\xi = u\hat{\xi}_x + v\hat{\xi}_y + w\hat{\xi}_z$$

$$\tag{4.55}$$

$$\widehat{U}_\eta = u\hat{\eta}_x + v\hat{\eta}_y + w\hat{\eta}_z \qquad \widehat{U}_\zeta = u\hat{\zeta}_x + v\hat{\zeta}_y + w\hat{\zeta}_z$$

Split of flux vectors in η and ζ directions ($\widehat{G}_c^\pm$ and $\widehat{H}_c^\pm$) by Van Leer flux splitting method are given in Appendix B.

4.6.3 AUSM Method

Another flux vector splitting method used in this study is AUSM (Advection Upstream Splitting Method). In principle, AUSM is similar to the Van Leer splitting Method. AUSM is a rather new flux vector splitting method suggested by Liou and Steffen [48] and it is based on splitting of the flux vector into convective and pressure fluxes.

$$F_i = \begin{bmatrix} \rho u \\ \rho u^2 + p \\ \rho uv \\ \rho uw \\ \rho uH \\ \rho_1 u \\ \vdots \\ \rho_{K-1}u \end{bmatrix} = \begin{bmatrix} \rho u \\ \rho u^2 \\ \rho uv \\ \rho uw \\ \rho uH \\ \rho_1 u \\ \vdots \\ \rho_{K-1}u \end{bmatrix} + \begin{bmatrix} 0 \\ p \\ 0 \\ 0 \\ 0 \\ 0 \\ \vdots \\ 0 \end{bmatrix} \tag{4.56}$$

The first part and second part of the fluxes namely convective and pressure fluxes are split according to the Mach number and pressure values, respectively. Left and right Mach number specifications is done as Van leer Mach number definition given in the Equation (4.51). In addition, the right and left values of the pressure required for the calculation of the fluxes at the cell interfaces can be split by two definitions given in the following equations. The first definition is given as:

$$
p^{\pm} = \begin{cases} \dfrac{1}{2}p(1 \pm M) & |M| \leq 1 \\ \dfrac{1}{2}p\dfrac{M \pm |M|}{M} & |M| > 1 \end{cases}
\tag{4.57}
$$

And the second method for splitting pressure is defined as:

$$
p^{\pm} = \begin{cases} \dfrac{1}{4}p(M \pm 1)^2(2 \mp M) & |M| \leq 1 \\ \dfrac{1}{2}p\dfrac{M \pm |M|}{M} & |M| > 1 \end{cases}
\tag{4.58}
$$

The split flux vector by AUSM method in ξ-direction ($\hat{F}_c^{\pm}$) can be written as in Equation (4.59).

$$
\hat{F}_c^{\pm} = M^{\pm} \begin{bmatrix} \rho a \\ \rho a + u\hat{\xi}_x p^{\pm} \\ \rho a + v\hat{\xi}_y p^{\pm} \\ \rho a + w\hat{\xi}_z p^{\pm} \\ a[\rho e_t + (\gamma - 1)(\rho e - \dfrac{u^2 + v^2 + w^2}{2})] \\ \rho a(\rho_1/\rho) \\ \vdots \\ \rho a(\rho_{K-1}/\rho) \end{bmatrix}
\tag{4.59}
$$

Split flux vectors in other directions ($\hat{G}_c^{\pm}$ and $\hat{H}_c^{\pm}$) according to AUSM method are shown in Appendix B.

4.7 Order of Accuracy

In order to provide the information for the flux vectors, flow variables from the centers of the neighboring cells should be implemented into the flux calculation at the cell interface. To do this, first or second order interpolation is applied.

4.7.1 First Order Schemes

In first order schemes, flow variables at cell interfaces are taken to be equal to their values at cell centers to the left and right of that interface. Simply, it can be written as:

$$\hat{Q}^-_{i+\frac{1}{2}} = \hat{Q}_i \qquad \hat{Q}^-_{i+\frac{1}{2}} = \hat{Q}_{i+1} \tag{4.60}$$

where, i is the cell center to the left of $i + 1/2$ interface and $i + 1$ is the cell center to the right of the $i + 1/2$ interface. First order TVD (Total Variation Diminishing) schemes, are monotone schemes. In other words, first order schemes have dissipative characteristics and tend to decrease the effect of discontinuities in the flow (such as shocks) or in the geometry. To capture the effect of discontinuities precisely, second or higher order schemes can be employed.

4.7.2 Second Order Schemes

In second order schemes, the information of the flow variables at cell interfaces are computed by interpolating the flow variable values at the neighboring cells. The variation of flow variables between the cells are taken into account in second or higher order schemes. By increasing the order of interpolation, higher order schemes can be constructed. Second order schemes can be established for the left and right values of the flow variables using the MUSCL (The Monotonic Upstream-Centered scheme for Conservation Laws) scheme which is written as:

$$Q_{i+\frac{1}{2}}^{-} = Q_i + \frac{1}{4}[(1 - \kappa)a_i + (1 + \kappa)b_i]$$

$$\text{(4.61)}$$

$$Q_{i+\frac{1}{2}}^{+} = Q_{i+1} - \frac{1}{4}[(1 - \kappa)b_{i+1} + (1 + \kappa)a_{i+1}]$$

Where

$$a_i = Q_i - Q_{i-1} \qquad b_i = Q_{i+1} - Q_i \qquad \text{(4.62)}$$

And κ is a value between -1 and 1 which defines the order of the accuracy for the employed scheme. Any value of κ other than 1/3, produces a second order accurate scheme. While, for the κ value of 1/3, the MUSCL schemes gives third order accurate solutions.

Constructing higher order schemes improves the accuracy of the solutions. Unlike first order schemes, higher order schemes do not have dissipative characteristics. In the regions of discontinuities, the second order schemes tends to capture abrupt changes in the flow variables precisely. Second order schemes provide more information about the flow variables by taking the small variations into account. Depending on the complexity of the flow or geometry and the stability of the numerical methods applied, oscillation may be generated and the solutions might not be converge. In order to avoid these problems at local discontinuous regions, flux limiters can be employed.

4.7.3 Flux Limiters

Flux limiters are the functions implemented into the second order schemes. The aim of the flux limiters is to identify the sharp changes in the flow and reduce the order to first order at these regions where gradients are high. Thus, oscillations will be prevented and efficient solutions may be attained. The second order schemes with flux limiters are constructed as in the following equations:

$$Q^-_{i+\frac{1}{2}} = Q_i + \frac{\psi(r_i)}{4}[(1-\kappa)a_i + (1+\kappa)b_i]$$

$$\tag{4.63}$$

$$Q^+_{i+\frac{1}{2}} = Q_{i+1} - \frac{\psi(r_{i+1})}{4}[(1-\kappa)b_{i+1} + (1+\kappa)a_{i+1}]$$

where;

$$r_i = \frac{b_i}{a_i} = \frac{Q_{i+1} - Q_i}{Q_i - Q_{i-1}} \tag{4.64}$$

And, ψ is a flux limiter function which is given by different methods. Here, the flux limiter functions of minmod, superbee, Van Leer and Van Albada is employed. The basic min-mod function is introduced as:

$$\psi(r) = \max[0, min(1, r)] \tag{4.65}$$

Superbee limiter function;

$$\psi(r) = \max[0, min(2r, 1), min(r, 2)] \tag{4.66}$$

Van Leer flux limiter,

$$\psi(r) = \frac{r + |r|}{1 + |r|} \tag{4.67}$$

And, Van Albada flux limiter function:

$$\psi(r) = \frac{r^2 + r}{r^2 + 1} \tag{4.68}$$

Van Albada method is one of the most accurate flux limiter functions which is widely used and studied in the area of second order TVD schemes. Venkatakrishnan [49] suggested a modified version of Van Albada to improve the convergence characteristics of the second order schemes. The modified Van Albada limiter is given

for two different values of κ as zero and 1/3 for which second and third order accurate schemes are constructed, respectively.

$$\psi(r_i) = \frac{a_i(b_i^2 + \varepsilon^2) + b_i(a_i^2 + \varepsilon^2)}{a_i^2 + b_i^2 + 2\varepsilon^2} \qquad \kappa = 0$$

$$\psi(r_i) = \frac{a_i(2b_i^2 + \varepsilon^2) + b_i(a_i^2 + 2\varepsilon^2)}{a_i^2 + b_i^2 - a_i b_i + 3\varepsilon^2} \qquad \kappa = \frac{1}{3} \qquad (4.69)$$

where, ε^2 is a parameter used to reduce the effect of flux limiter in smooth flow regions to increase the convergence characteristics of the scheme.

4.8 Boundary Conditions

Implementation of boundary conditions can be difficult depending on the physical domain of the problem. However, transforming the solution domain from physical to computational space makes the application of boundary conditions simpler [44]. Since in this study, the computational space is used to solve the equations of fluid motion, enforcement of boundary conditions are rather simple.

In order to employ the boundary conditions properly, ghost cells are generated at the outside of the computational boundaries. The ideal is to assign values of the flow variables in these computational cells such that the proper boundary conditions are imposed. Inflow, outflow, wall and symmetry boundary conditions should be specified to solve the proposed problem. These boundary conditions may vary in different flow patterns of inviscid and viscous flow.

Inflow boundary condition is set to be as the free stream conditions and outflow condition is set to be free without any limitations. For symmetry boundary condition, the values of ghost cells are set in a way that the normal velocity to the plane of symmetry becomes zero. This is achieved by equalizing the tangential velocity of the ghost and interior cell at the symmetry plane. Whereas, the normal velocity in the ghost

cell is assigned in the opposite direction of the normal velocity of the interior cell. The symmetry boundary condition is same for inviscid and viscous flows.

Wall boundary conditions are different considering inviscid or viscous flows. For inviscid flows, the values of normal velocity at ghost cells are taken as opposite of the normal velocity in the interior cell. The tangential velocity at the wall boundary condition is not zero for inviscid flows. However, for viscous flows, no-slip boundary condition is applied at the walls. In no-slip boundary condition, the values of velocities in all directions are set to be zero. This is done by imposing the velocity at the ghost cells in the opposite direction of the velocity values of the interior cell.

4.9 Solution Method

Three dimensional coupled Navier-Stokes and chemical reaction model equations are used in this study. The non-dimensionalized governing equations were written in generalized coordinates and discretized using finite volume method. Now, the coupled system of equations should be solved. For this purpose, Newton GMRES method is applied. The generalized minimum residual method (GMRES) can be categorized as a Krylov subspace method. Basic goal of the Krylov subspace methods are to solve linear problems of $Ax = b$. Starting from an initial value of x, after each iteration the new value for the x is found along with the correction in the Krylov subspace. In other words, to calculate the value of x, the process does not need to read all the data in matrix A. Therefore, Krylov methods require less computation space.

On the other hand, Newton methods which are powerful solvers of the different equations require high CPU times. In Newton methods, Jacobian matrix computation must be done. Calculation of Jacobian matrices needs great computational effort since sparse matrices should be solved. Therefore, GMRES algorithm is implemented to Newton method to increase the efficiency of the computation and Newton GMRES method is developed. Newton GMRES method which is in subcategory of Newton-Krylov methods can be recognized as one of the inexact Newton methods.

The most important characteristic of Newton GMRES method is that it does not need the calculation of Jacobian matrix. Jacobian matrix calculation increases the computation time and so decreases the efficiency of the method. Mathematical representation of the Newton GMRES is given as follows.

Nonlinear system of equations can be written as:

$$\hat{R}(\hat{Q}) = \frac{\partial(\hat{F}_c - \hat{F}_v)}{\partial \xi} + \frac{\partial(\hat{G}_c - \hat{G}_v)}{\partial \eta} + \frac{\partial(\hat{H}_c - \hat{H}_v)}{\partial \zeta} - \hat{S} = 0 \qquad (4.70)$$

where $\hat{R}$ is the residual vector. The goal of the numerical solver is to approach the residual value of zero. In order to solve the equation of the residual, the Newton method can be written as in the following equation.

$$\left(\frac{\partial \hat{R}}{\partial \hat{Q}}\right) \Delta \hat{Q} = -\hat{R}(\hat{Q})$$

$$\Delta \hat{Q} = \hat{Q}' - \hat{Q}$$

$$(4.71)$$

where, $\hat{Q}'$ denotes the value of $\hat{Q}$ at the next iteration and $\partial \hat{R}/\partial \hat{Q}$ is the Jacobian matrix which need to be solved in Newton methods. However, implementation of GMRES is applied at this point. In order to avoid the calculation of the Jacobian matrix, Newton GMRES acquire a forcing term η_k. The accuracy of the solutions approximation is controlled by using this forcing term which its value ranges from zero to one. Convergence characteristics of the Newton GMRES method is highly dependent on the value of the η_k. The limitation of this term in calculation of the residual can be expressed as:

$$\left\| \hat{R}(\hat{Q}) + \hat{R}'(\hat{Q}) \, \Delta \hat{Q} \right\| \leq \eta_k \left\| \hat{R}(\hat{Q}) \right\| \qquad (4.72)$$

To evaluate the value of the residual at the next iteration $\hat{R}'(\hat{Q})$ Jacobian matrix is needed. To avoid this, multiplication of this value with the normalized vector of v can be approximated as in the equations using finite differencing.

55

$$\hat{R}'(\hat{Q}) \cdot v \approx \frac{\hat{R}(\hat{Q} + \epsilon v) - \hat{R}(\hat{Q})}{\epsilon} \tag{4.73}$$

Therefore, the computation of the Jacobian matrix is not necessary and this method is labeled as matrix-free numerical solution algorithm [50].

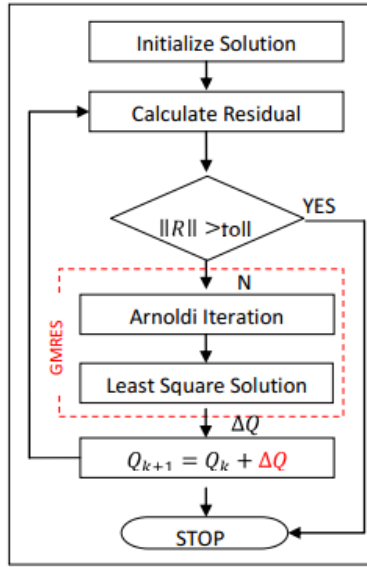The flowchart of the Newton GMRES algorithm is shown in the Figure 4.1.

Figure 4.1 Newton GMRES Scheme [50]

Newton GMRES method is started with an approximation of the initial value of the x in the problem of $Ax = B$. Then, residual (r_0) is computed for the initial value of x. The process continues with application of Arnoldi iteration. The Arnoldi iteration is a process which receives the values of residual and x and gives the Heisenberg matrix as an output with the use of Krylov subspace. The process is given as [51]:

$$V = \frac{r_0}{\|r_0\|} \tag{4.74}$$

$$AV_k = V_{k+1}H \qquad for \quad V_k = [V_1, V_2, \dots, V_k]$$

where, V is an orthonormal vector and H is the Hessenberg matrix to be constructed. The residual after the Arnoldi iteration become as:

$$min\|b - Ax\| = min\|b - A(x_0 + Vy)\|$$

$$Vy \in k_m(A, r_0)$$

$$k_m(A, r_0) = span\ \{r_0, Ar_0, A^2r_0, A^3r_0, \dots, A^{m-1}r_0\}$$

(4.75)

$$min\|b - Ax\| = min\big\|\|r_0\|e_1 - AVy\big\| = min\big\|\|r_0\|e_1 - Hy\big\|$$

Where, $k_m(A, r_0)$ is the Krylov subspace of order m and, $e_1 = [1, 0, \dots, 0]^T$. Now, the problem reduces to least square and the value of y should be optimized to get the minimum residual. For this purpose, QR factorization is employed where Hessenberg matrix, which becomes an upper matrix at the end of Arnoldi process, is decomposed to orthogonal and triangular matrices. Finally, after the minimization of the value of y, the solution of the equation is found as:

$$x_{n+1} = x_n + Hy \qquad (4.76)$$

where n is the iteration number.

CHAPTER 5

RESULTS AND DISCUSSIONS

The system of equations described in the previous chapters are solved and the results are shown here. In order to identify the effect of different parameters on the flow analysis, different parametric studies are done. Since solving three dimensional Navier-Stokes equations with chemical reactions require great computational effort, the parametric studies are done on simplified Euler equations. In this system of equations, viscous effects of the flow is ignored to increase the efficiency of the parametric studies. The validity of the results obtained by the Euler equations are investigated and approved. Therefore, evaluation of different methods and schemes along with various configurations are done and shown in the following. Finally, results obtained using Navier-Stokes equations are given.

The base geometry of scramjet combustion chamber used in this study is taken from the experimental scramjet tested in research cell 18 placed at Wright-Patterson Air Force Base. The mentioned scramjet is taken as reference since it is one of the most recent experimental scramjets used. Also, data from the experimental studies of this module are available in the literature which is crucial for code validation purposes. The schematic of the full experimental scramjet engine is shown in Figure 5.1.
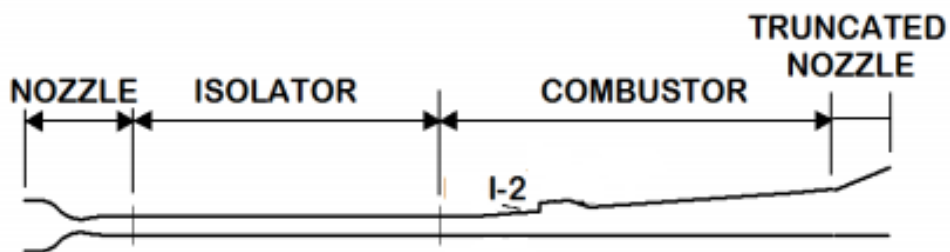

Figure 5.1 Schematic of the Experimental Scramjet [26]

From Figure 5.1, it can be seen that the facility nozzle provides the inlet flow and isolator which is a constant area duct compresses the incoming flow by passing it through several oblique shocks. Then, flow enters the combustor area where fuel is injected upstream of the cavity from I-2 injectors. Finally, divergent nozzle is implemented to increase the flow speed. The combustion chamber of this experimental scramjet is designed with a cavity recessed in its body wall. Body wall has a constant divergence angle of 2.6 degrees and L/D of the cavity is approximately equal to 5. Moreover, the aft-wall of the cavity has an angle of 22.5 degrees with respect to the cavity floor. Cavity-based combustor is shown in Figure 5.2 and Figure 5.3.
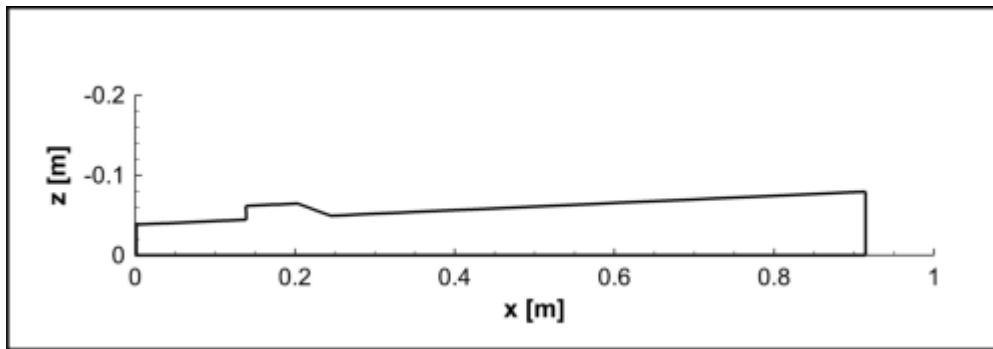

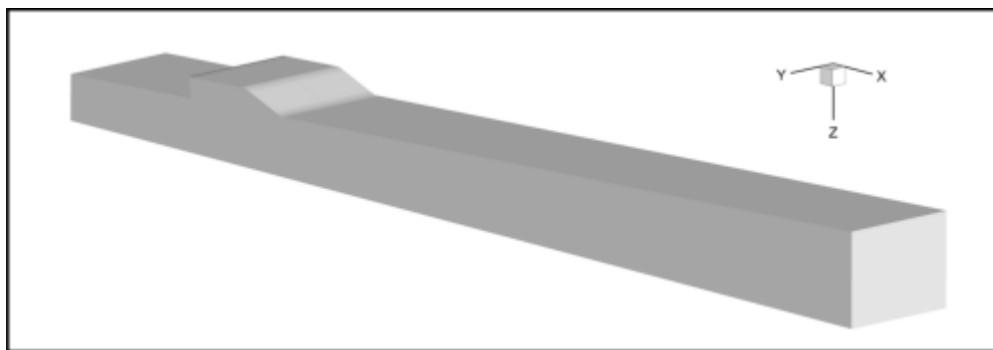Figure 5.2 Two Dimensional Drawing of the Combustor

Figure 5.3 Three Dimensional Drawing of the Combustor

Configuration of the fuel injectors used in the scramjet combustion chamber is shown in Figure 5.4. In order to take advantage of the recirculation region around the cavity, fuel is injected upstream of the cavity.
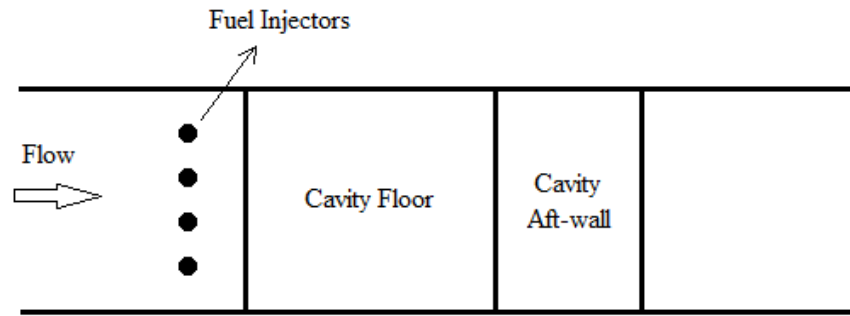
Figure 5.4 Upstream Fuel Injection Configuration (Top View)

The location of the fuel injectors is highly important in increasing the mixing efficiency of the fuel-air. Fuel injectors located far upstream will cause flame holding problems because of high velocities at the combustor entrance. Mixing efficiency reduces at high speeds because of the low residence time of the flows at these speeds. Therefore, flames will be unstable and continuous combustion will not occur. On the other hand, if the fuel injectors were placed on the edge of the cavity front wall, the fuel will not be able to penetrate into the core flow by taking advantage of the reduced velocity and recirculation region in the cavity. The shear layer will interrupt the fuel-air mixing and so efficiency of the mixing will decrease in a great amount. Therefore, fuel injection should be done from a small distance upstream of the cavity front wall. In this way, higher mixing efficiency of fuel-air will be achieved in the cavity region. This is one of the important characteristics of the cavities which make them more efficient compared to other flame holding methods in scramjet combustors.

5.1 Inviscid Flows

In this part, viscous effect of the flow is neglected and so Navier-Stokes equations are reduced to Euler equations. Three dimensional Euler equations are solved coupled with finite rate chemical reaction model equations. The idea is to study some features of the flow related to only inviscid part of the Navier-Stokes equations in a computationally efficient way. For example, flux vector splitting methods are applicable on the inviscid fluxes and viscous fluxes are not split with the methods such

as Steger-warming, Van Leer or AUSM. Therefore, the study of different flux splitting methods are done for inviscid flow. Moreover, since neglecting viscous effects reduce the computational effort and time, it is more plausible to conduct different studies with Euler equations. The amount of CPU time is reduced in great levels for these studies. However, the validity of Euler equations for performing these studies should be confirmed. The validation of the code written for inviscid flow case is done in the following section.

5.1.1 Grid Refinement for Inviscid Flows Case

In order to remove the mesh dependency on the flow solutions, grid refinement study is done. For this purpose, three different grids are generated by improving the grid resolutions and labeled as coarse, medium and fine meshes. Information about the number of cells and interfaces in different directions are tabulated in Table 5.1. The fundamental aim is to find the lowest mesh resolution which provides enough accuracy and is efficient computational-wise.

Table 5.1 Generated Meshes with Different Resolutions for Inviscid Flows

Grid Resolution	Number of Nodes (i x j x k)	Number of Cells in Half Domain
Coarse	61x11x8	2,100
Medium	65x17x17	8,192
Fine	120x21x23	26,180

In order to reduce the computational effort and increase the speed, the computations are performed on half of the solution domain. The domain is split into two parts along the side wall (y-direction) where symmetry boundary condition is applied. The combustor is symmetrical in the axis perpendicular to the flow direction

and side walls. The grid resolution for the fine mesh is shown in Figure 5.5 for whole domain. The unit directions of i, j and k are in the x, y and z directions, respectively.
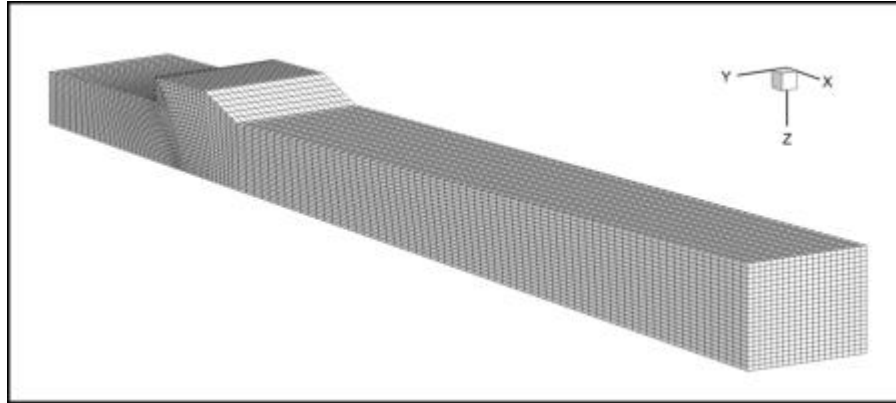

Figure 5.5 Fine Mesh Used for Inviscid Flows

Before proceeding with the solutions, the validity of the solutions should be confirmed. For this purpose, experimental and numerical data from different studies are employed. In order to verify the results of the present study, the experimental data from the wright Patterson laboratory [26] and the numerical data provided by Lin et al. [26] are used for the validation and grid refinement study. The combustor inlet conditions applied in the solution of the present study are taken from the experimental data and can be summarized as in Table 5.2.

Table 5.2 Combustion Chamber Inlet Conditions

Flow Variable	Value
Pressure	60 kPa
Temperature	700 K
Mach	1.34

Several experiments are done on this experimental scramjet to simulate the different flight conditions [26]. For validation of the code in the present study, the data

from the experiments conducted to simulate the scramjet at flight Mach number of 4.5 is used. In this experiment, Mach number of 2.2 with total temperature of approximately 950 K is provided by the facility nozzle at the entrance of the isolator. Equivalence ratio of 0.6 is maintained at upstream fuel injectors. In numerical studies of Lin et al. [26], the simulations are performed with CFD++ code. In these simulations, RANS equations are solved with two-equation cubic $\kappa - \varepsilon$ turbulence model. Moreover, the simulation are based on finite volume scheme with multi-dimensional Total Variation Diminishing (TVD) method and Riemann solvers. Data obtained from the aforementioned experimental and numerical studies are used to validate the inviscid flow solutions obtained from the present study in Figure 5.6.
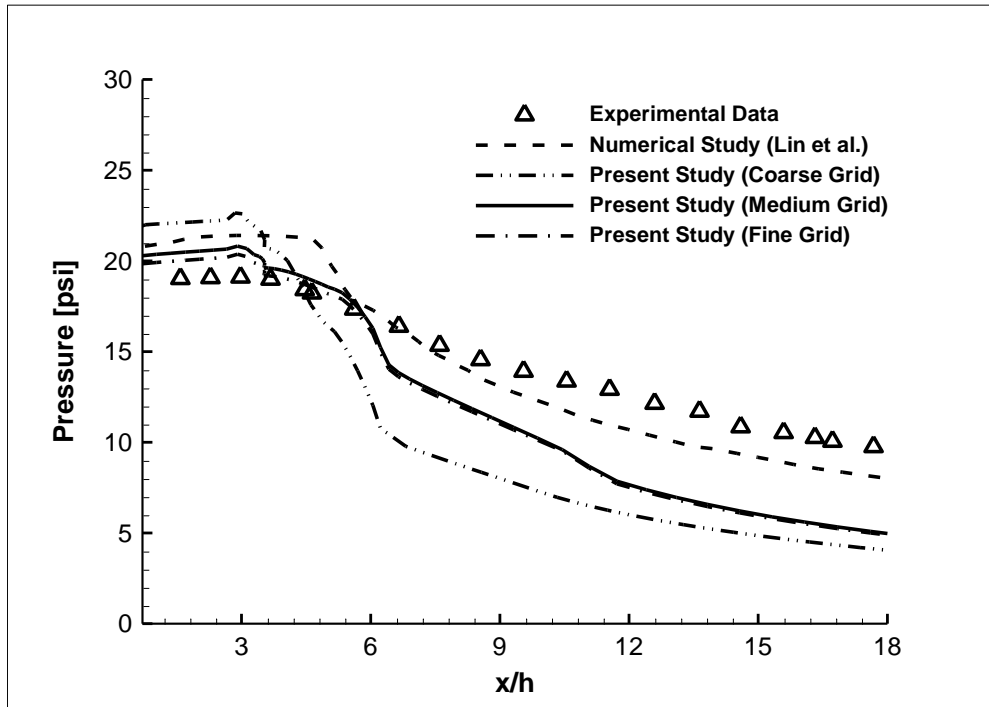

Figure 5.6 Pressure Distribution Comparison with Experimental and Numerical Data

where, x/h is the non-dimensionalized value of combustor length (x) with respect to combustor inlet height (h). The pressure distribution obtained for inviscid flow case shows that the pressure decreases in a great amount downstream of the cavity. Because no-slip boundary condition is not applied in inviscid flows, the velocity increases near

the wall and so pressure drops. However, since numerical study of Lin et al. is done using RANS equations where no-slip boundary condition is applied at the walls, decrease in the pressure values are soft like as the pressure distributions obtained from experiments. Therefore, the solutions obtained for inviscid flow are reasonable.

On the other hand, solutions of different mesh sizes are compared. In addition, CPU time used to solve the problem using these meshes are tabulated as:

Table 5.3 CPU Time Variation of Different Grid Resolutions

Grid Resolution	CPU time
Coarse	1218 s
Medium	5994 s
Fine	11490 s

As it can be seen from the Figure 5.6, medium and fine grid resolution have a very slight difference in their pressure levels. However, the solution obtained using coarse mesh experiences great deviation from the pressure values obtained for experimental and numerical data. Studying the number of nodes for these mesh sizes shows that mesh resolution is not sensitive in the i-direction. While, increasing number of the nodes in j and k direction improves the solutions accuracy. In addition, Table 5.3 shows that the CPU time for fine mesh is twice longer than the CPU time for medium mesh. Therefore, using the medium mesh resolution in simulating the combustor is computationally more efficient.

In addition to validation of the code according to pressure distribution comparison with experimental and numerical data, mixing efficiency is also compared with the numerical study of the Lin et al. [26]. Since there is no other experimental data available for the desired combustor, mixing efficiency is used as an alternative data for code validation.
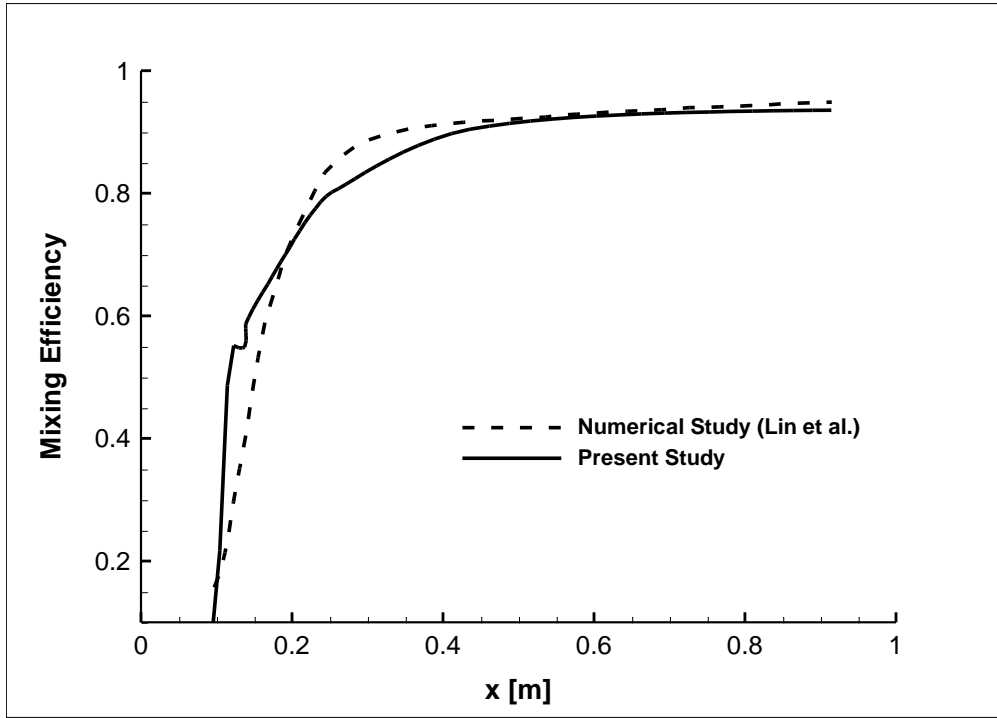
Figure 5.7 Comparison of Mixing Efficiency with Numerical Data

Studying Figure 5.7 shows that mixing efficiency obtained from the present study is overall in good agreement with the results from the numerical study of Lin et al. However, there is a slight difference in the cavity region of the combustor. Considering all, it can be concluded that the solutions obtained from the present study for inviscid flow case are accurate.

5.1.2 Comparison of Flux Splitting Methods

Different flux splitting schemes are employed and convergence histories are compared. For this purpose, solutions are obtained separately for first and second order schemes. The approximation of the solution is stopped after normalized residuals reached six orders. The comparison of Steger-Warming, Van Leer and AUSM flux splitting methods are shown in Figure 5.8 for the first order scheme.
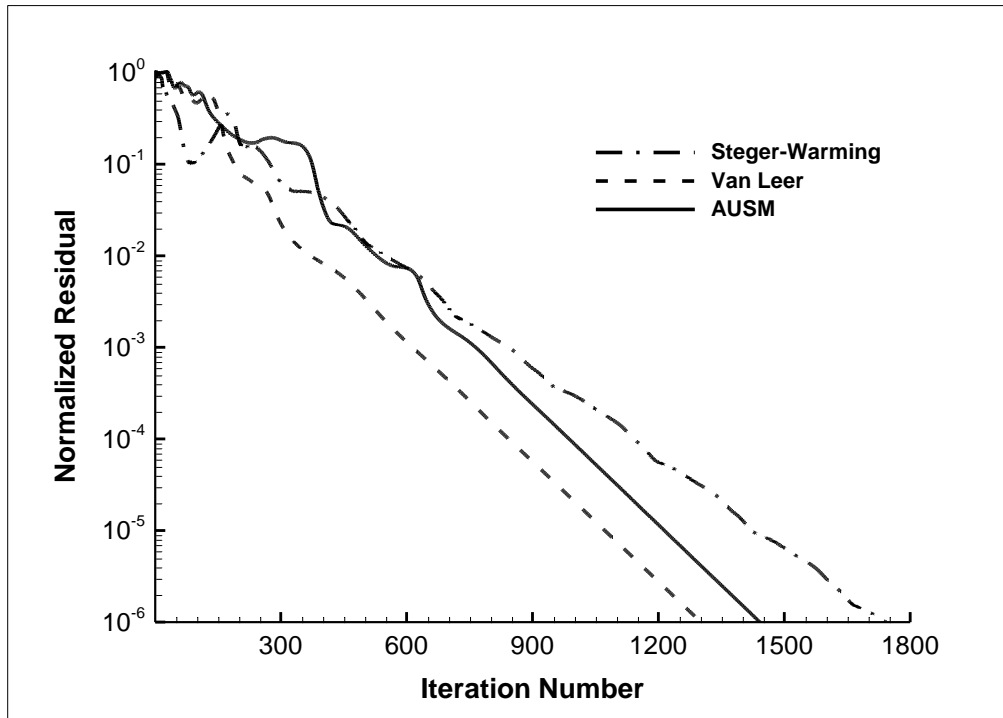
Figure 5.8 Residual History of Different Flux Splitting Methods in 1st Order Scheme

As it can be inferred from the Figure 5.8, different flux splitting methods of Steger-Warming, Van Leer and AUSM are employed for the solution of inviscid flows using the first order scheme. Steger-Warming reaches the convergence criteria after about 1700 iterations whereas Van leer and AUSM methods meet the criteria in less than 1200 iterations. In other words, Van Leer and AUSM flux splitting methods show a better performance compared to Steger-Warming method for the first order scheme case used here. However, since Newton GMRES method contains inner iteration steps in every iterations, the CPU time becomes important in the analysis of a convergence characteristics of the flux splitting methods. CPU time used in the solutions are tabulated in Table 5.4 for flux splitting methods used. It can be understood by comparing iteration numbers and CPU times that even though AUSM reaches convergence criteria at higher iteration number than the Van Leer method but the CPU time used in the AUSM is lower. This, shows that Van Leer experienced larger inner steps at every iteration. Steger-Warming shows the worst characteristic among the flux methods used here considering both iteration number and CPU time.

Table 5.4 CPU Time for Different Flux Splitting Methods in 1st Order Scheme

Flux Splitting Method	CPU time
Steger-Warming	3883 s
Van Leer	3064 s
AUSM	2324 s

Furthermore, the solutions obtained using Van Leer and AUSM methods are compared to find out the most suitable flux vector splitting method for the present study. Since Steger-Warming shows a poor convergence characteristics, it is not used for further comparison. Van Leer and AUSM methods are compared in Figure 5.9.

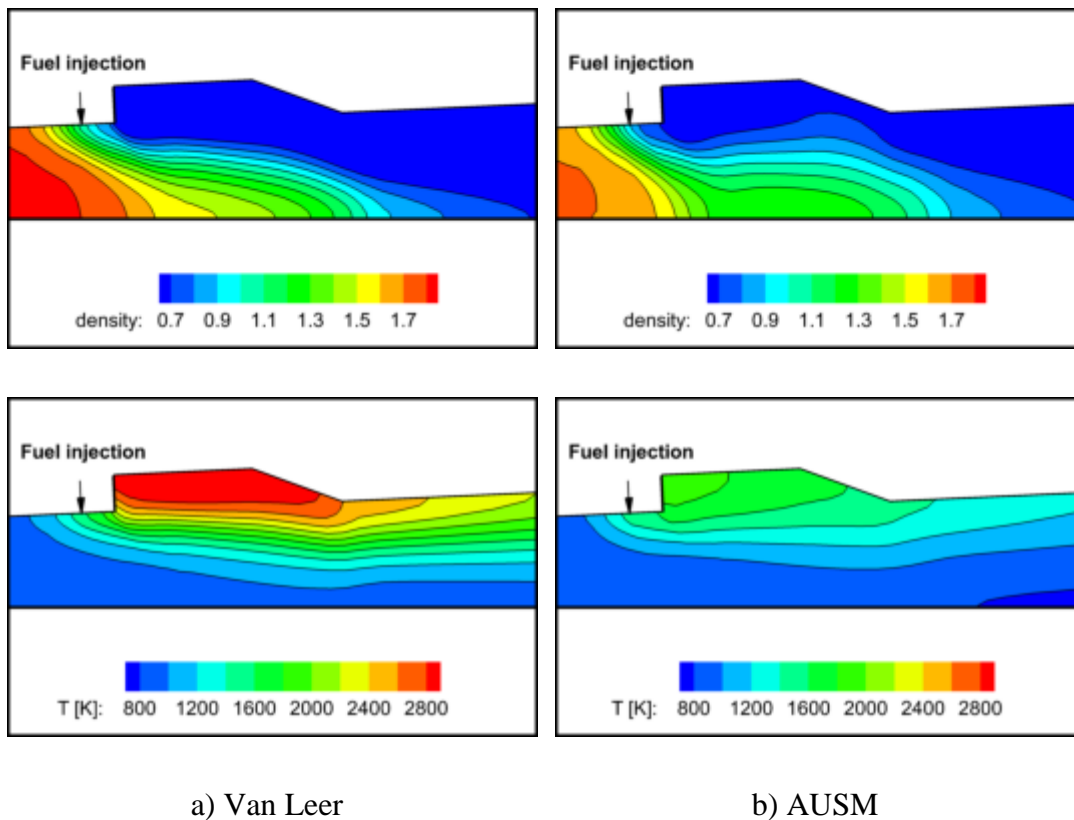a) Van Leer   b) AUSM

Figure 5.9 Comparison of Van Leer and AUSM Methods by Contours

As it can be seen from the Figure 5.9, sharp changes in the density of the flow due to shocks are captured by Van Leer method precisely. These abrupt changes become smoother in the solutions of AUSM. Moreover, the solutions from Van Leer catches the small details in the flow more than AUSM method. Therefore, comparing these two methods, Van Leer flux splitting method is most accurate flux splitting method among the employed methods in this study.

Further, flux vector splitting methods are implemented into second order schemes and the residuals are shown in Figure 5.10. Order of the interpolation used to approximate the flow variables at cell faces effects the performance of the flux vector splitting methods.
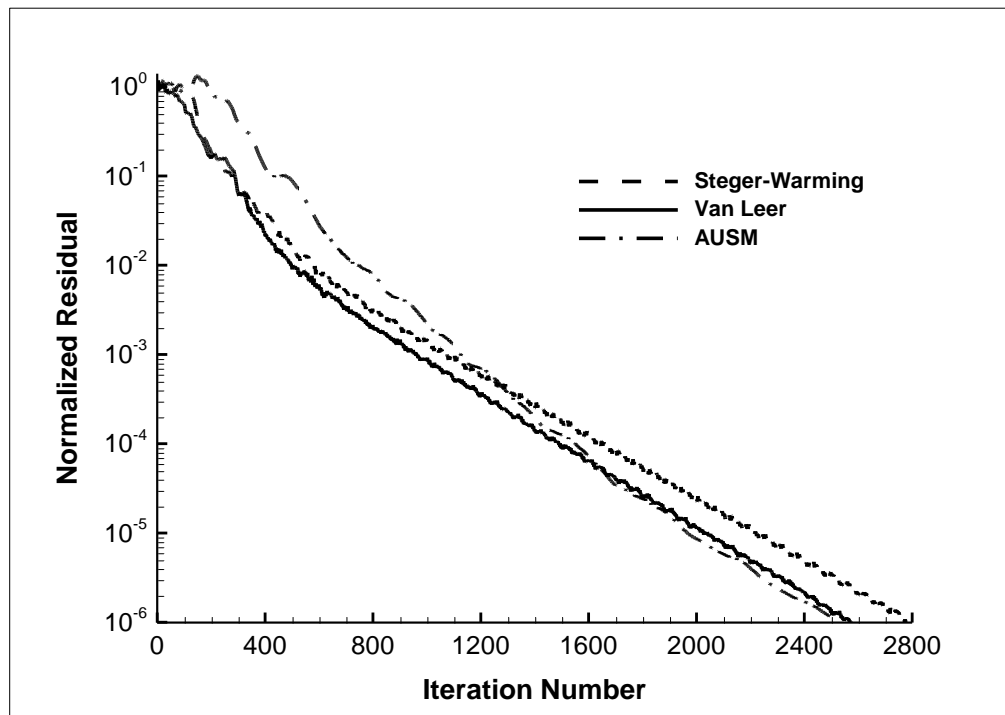

Figure 5.10 Residual History of Different Flux Splitting Methods in 2nd Order Scheme

In the second order scheme, convergence characteristics of flux vector splitting methods differed from their performance when applied with the first order schemes as expected. Van leer and AUSM has converged at almost same iteration numbers as can be seen from the Figure 5.10. However, CPU time of the AUSM method is lower than

that of Van Leer's (Table 5.5). The lower CPU time of the AUSM method is due to the fact that flux vector splitting is done by simple Mach and pressure splits. The formulation used in AUSM is very simple so that it makes AUSM computationally efficient. However, the solutions obtained are not as accurate as the other methods.

Table 5.5 Used CPU Time by Flux Splitting Methods in 2nd Order Scheme

Flux Splitting Method	CPU time
Steger-Warming	25276 s
Van Leer	26291 s
AUSM	22719 s

Analysis of the characteristics of the Steger-Warming flux splitting method in first and second order schemes shows that it is computationally inefficient in this study. Moreover, by evaluating the performance of the Van Leer and AUSM methods in both first and second order schemes base, it can be concluded that Van Leer methods is the most accurate method to be used in this study. Therefore, in the following sections, the solutions are obtained using Van Leer flux splitting method.

5.1.3 Implementation of First and Second Order Schemes

The simplest scheme to provide the information at the cell interfaces is to use first order scheme. In first order scheme, the values at cell centers are used directly as cell face values. In this scheme, the variation of flow variables between cell centers and cell faces are neglected. However, in second order schemes, the flow variables at cell interfaces are obtained by using interpolation between the variables at cell centers and so the variation of the values between the cell centers and faces is taken into account. Therefore, second order schemes are expected to give more accurate solutions than first order schemes. In this study, first and second order schemes are implemented

and the solutions obtained from these schemes are compared to get a better insight about their accuracy. Moreover, flux vector splitting methods can be important especially in the solution of second order schemes. Here, the convergence characteristics of these two schemes are analyzed using Steger-Warming, Van Leer and AUSM flux vector splitting methods.
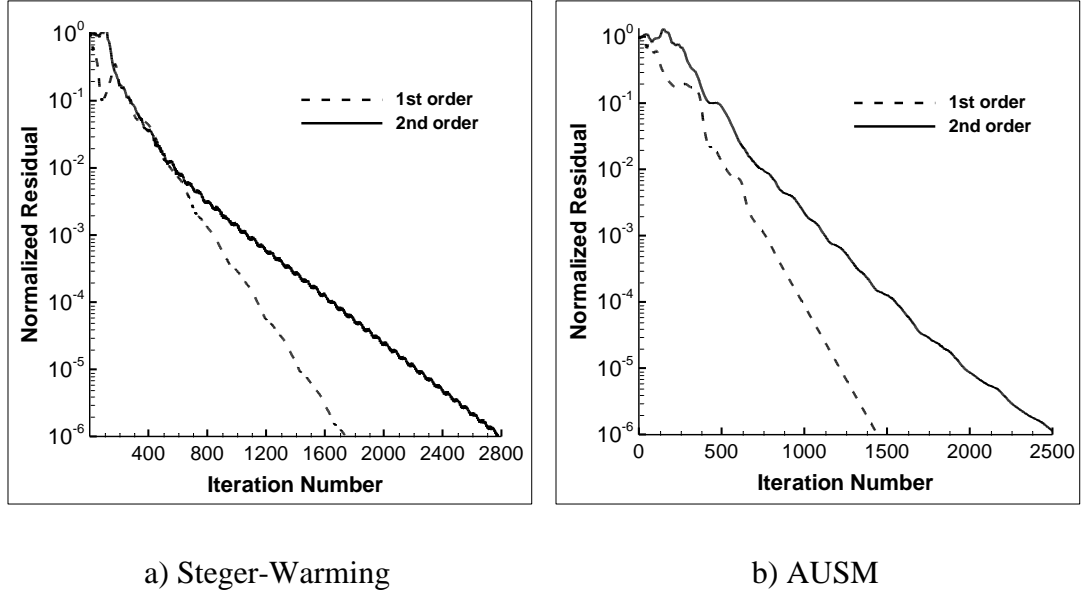

a) Steger-Warming   b) AUSM

Figure 5.11 First and Second Order Schemes' Residual Comparisons

The convergence histories of the first and second order schemes with Steger-Warming and AUSM flux splitting methods are shown in Figure 5.11. The solution of the first order scheme meets the convergence criteria at lower iterations. In other words, the solution approaches to the exact solution faster than the second order scheme with both Steger-Warming and AUSM method. This is due to accurate approximation of flow variables at cell faces which is obtained by second order interpolation of the variables. The second order schemes experiences oscillation while converging to the exact solution. The oscillations are caused by the interpolation of the flow variables at cell faces which may undershoot or overshoot considering the real values of the flow variables.

71

In addition, first and second order schemes are compared by using Van Leer flux vector splitting method as it can be seen in the Figure 5.12.
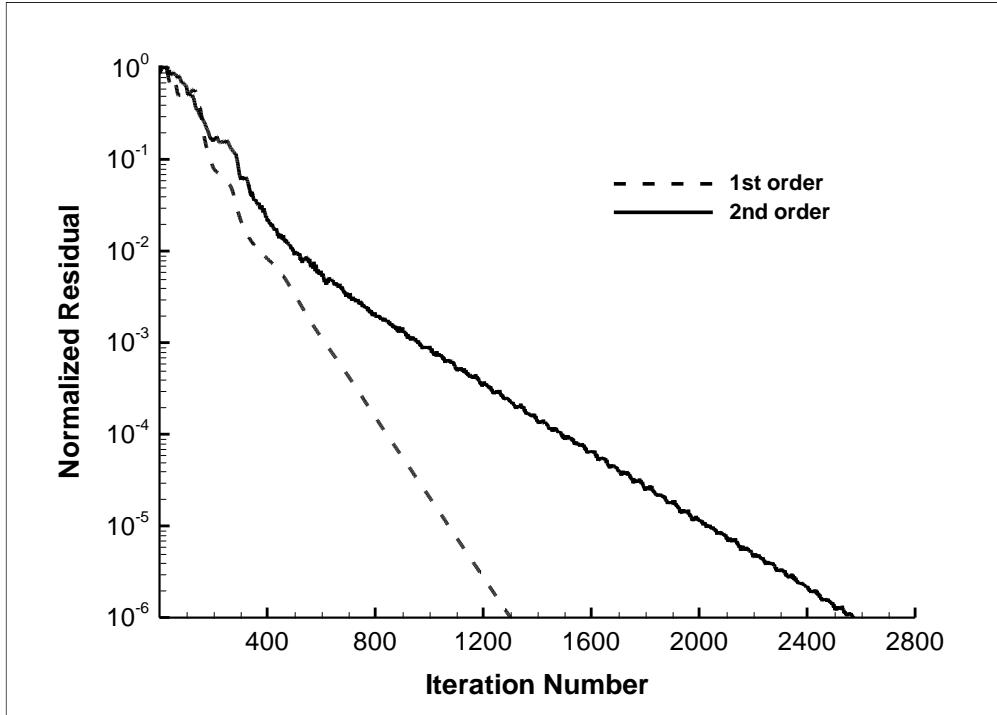

Figure 5.12 First and Second Order Schemes' Convergence Comparison (Van Leer)

It can be observed from the Figure 5.12 that second order scheme's residual, reduces six order of magnitude after higher number of iterations than the first order scheme using Van Leer method. However, Second order schemes give accurate solutions regarding the fact that flow variables are approximated in a better accuracy at cell faces compared to first order methods. Therefore, using second order schemes give more accurate solutions compared to first order schemes while first order schemes are computationally more efficient. Comparing CPU time of different flux vector splitting methods in first and second order schemes which are given in Table 5.6 shows that the CPU time increases approximately 7 times for second order scheme. However, accuracy of the solutions is more important than the CPU time used for most of the problems.

Table 5.6 Comparison of CPU Times for 1st and 2nd Order Scheme

Flux Splitting Method	CPU time (1st order)	CPU time (2nd order)
Steger-Warming	3883 s	25276 s
Van Leer	3064 s	26291 s
AUSM	2324 s	22719 s

In order to study the first and second order schemes thoroughly, variation of different flow variables are compared in the cavity region where discontinuity in the geometry along with fuel injection cause abrupt changes in the flow variables. Moreover, the chemical reactions start to occur after the injection of the fuel. The cavity region is shown in Figure 5.13.
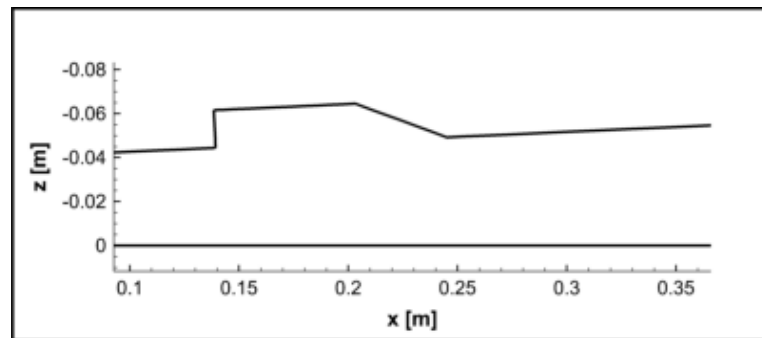

Figure 5.13 Cavity Section of the Combustor

As a first step, 2-D distribution of some of the flow variables and chemical species are shown in Figure 5.14. It can be seen that changes in the flow variables are sharper in second order schemes. The abrupt changes caused by discontinuities are captured precisely in second order implementation. Therefore, the solutions are more accurate compared to first order schemes. Moreover, moving in the downstream direction, Mach number increases because of the divergent angle of the combustor.

In addition to 2-D distributions, variation of flow variables and species' mass fraction are given by contours in Figure 5.15 and Figure 5.16.
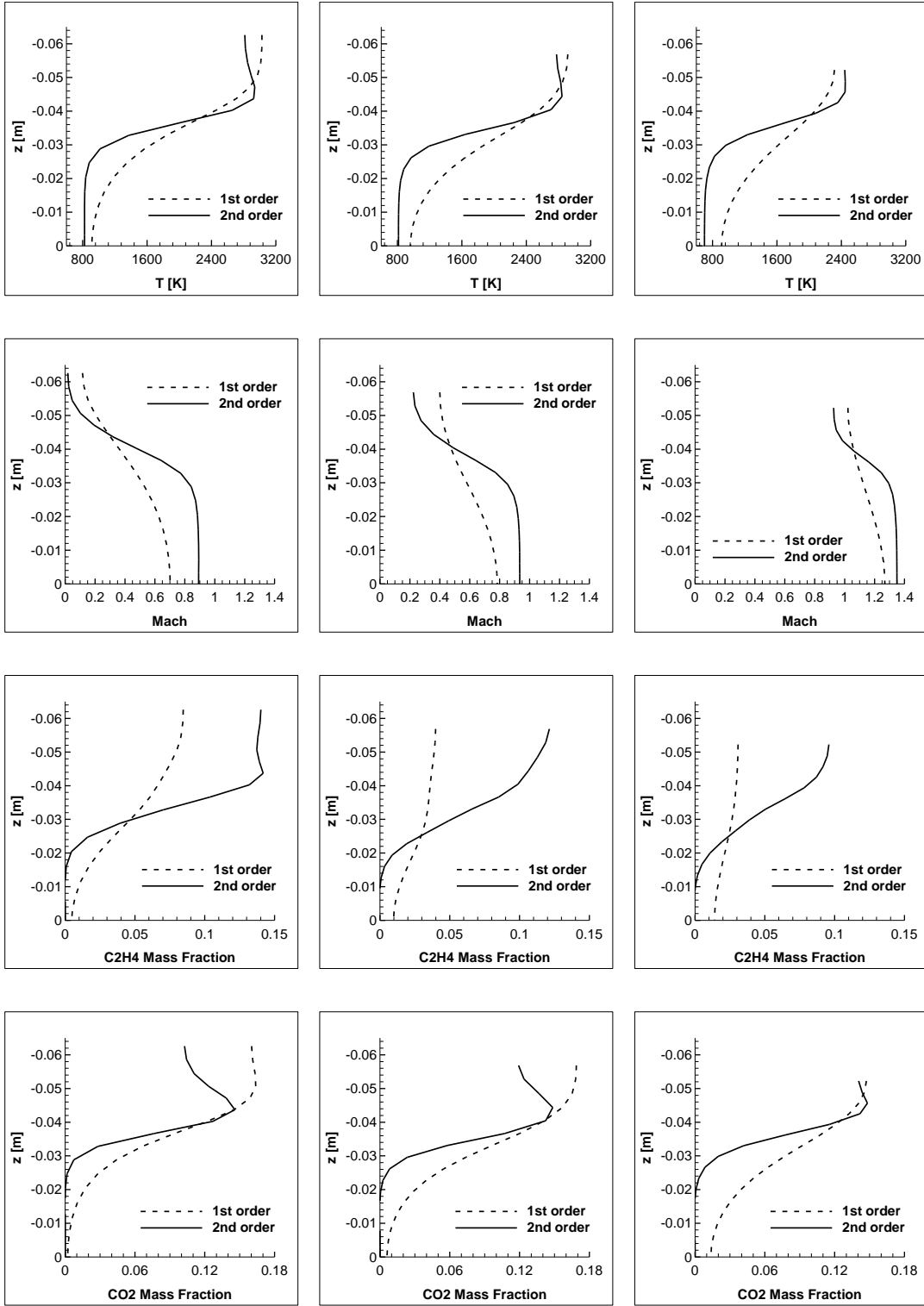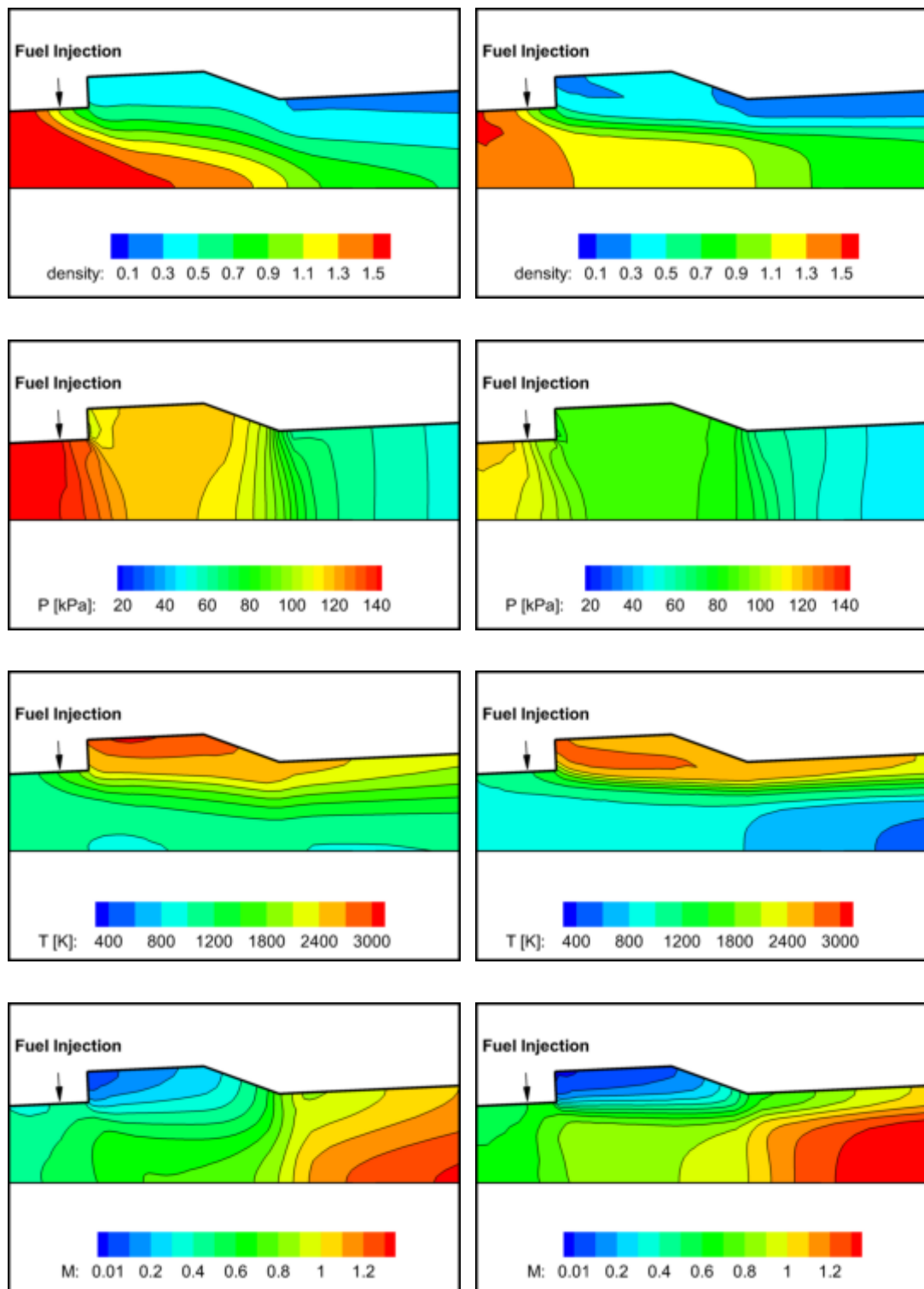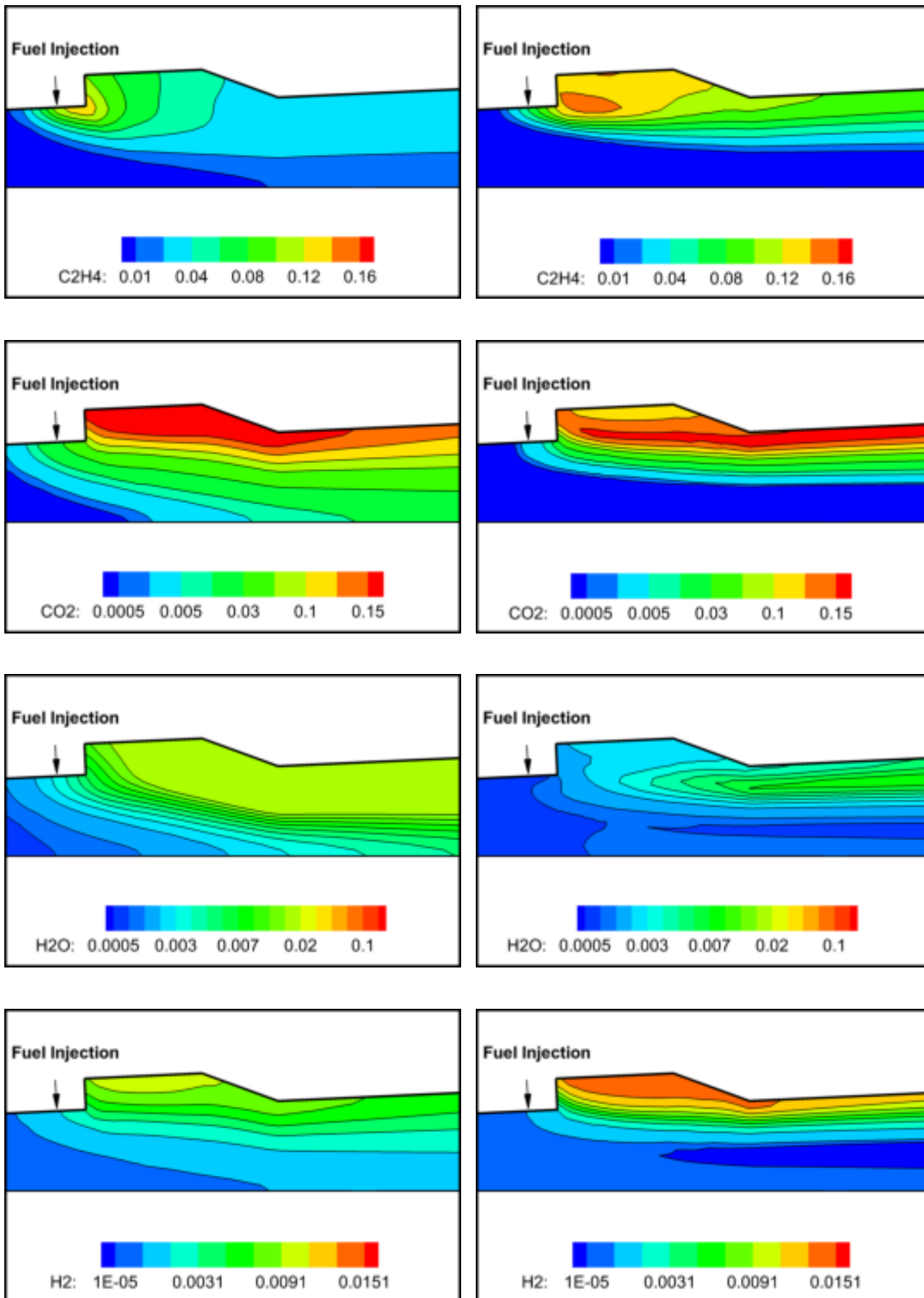
x = 0.17 m   x = 0.23 m   x = 0.31 m

Figure 5.14 2-D Distribution of Flow Variables at Different x Locations

a) First Order Scheme   b) Second Order Scheme

Figure 5.15 Comparison of 1st and 2nd Order Schemes by Flow Variable Contours

a) First Order Scheme   b) Second Order Scheme

Figure 5.16 Comparison of 1st and 2nd Order Schemes by Species' Mass Fraction

The solutions obtained for Scramjet combustor using first and second order schemes are given. As it can be seen from the Figure 5.15, the solutions obtained using second order scheme contains more details about the flow. The shocks generated in the vicinity of the fuel injection location and cavity is shown with better accuracy. Density shows an abrupt change over the shock while first order scheme approximated a gradual density variation before and after the shock. Second order scheme captured slight variations of pressure and Mach values around the fuel inject location and details of the flow variables are more accurate. However, the results obtained using first order scheme can also be considered enough accurate. It gives information about the flow in a rather fast computation.

Moreover, the comparison of the variation of the chemical species around the cavity are also given in Figure 5.16. Fuel (Ethylene, C_2H_4) is injected upstream of the cavity and the reactions takes place afterward. The variation of the mass fractions of the species shown upstream and downstream of the cavity present the occurrence of the chemical reactions mostly in the cavity region. The accuracy of the species mass fraction contours are high for second order schemes. Ethylene spreads over the cavity and reacts with Oxygen (O_2) and gives carbon monoxide (CO) and hydrogen (H_2) as the products. Then, the products react with oxygen (O_2) and carbon dioxide (CO_2) and hydrogen dioxide (H_2O) are produced. The variation of these species for both first and second order schemes give details about the reaction mechanism. Abrupt changes in the species mass fractions are captured more precisely in second order schemes.

5.1.4 Flux Limiters

In higher order schemes due to the presence of discontinuities in flow (shocks) or geometry, solution may possess oscillations. In order to avoid these oscillation in the solution domain, different flux limiters are used. In this study, to control the sharp changes in second order schemes some of the most suitable flux limiter functions are employed and compared according to their convergence characteristics. Convergence histories of these flux limiter are shown in Figure 5.17.
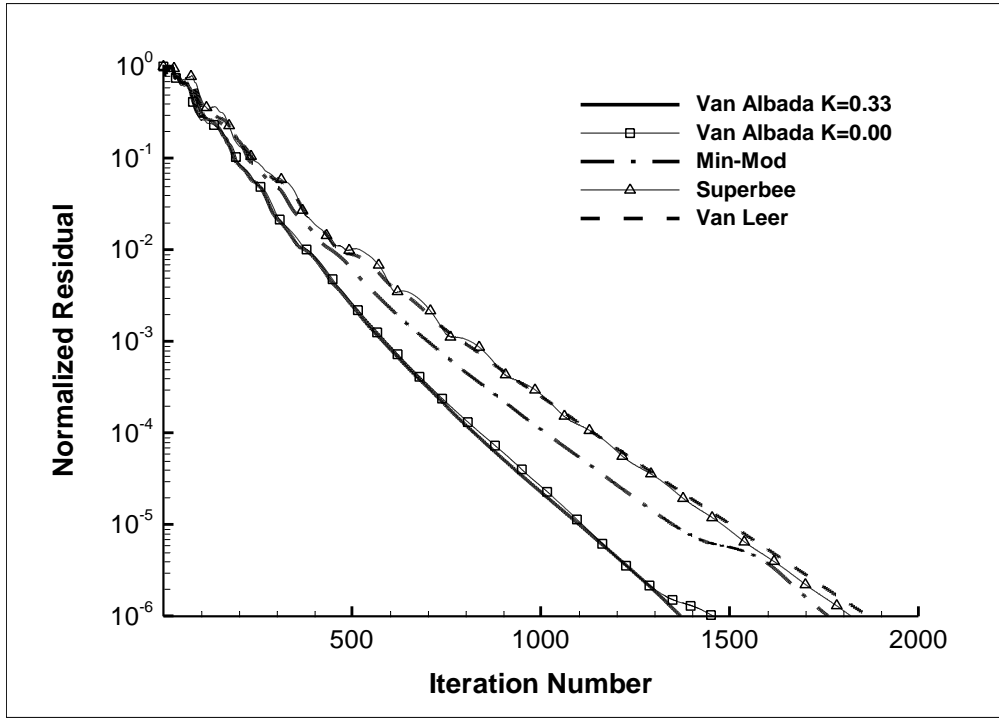
Figure 5.17 Residual History of Different Flux limiters

From the Figure 5.17, it can be observed that Van Albada flux limiter function with different orders of accuracy (second and third order accuracy) experienced a better convergence history. Van Albada limiter of third order accuracy provides the best solution by reaching the normalized residual criteria in less than 1400 iterations. Although the other flux limiter such as Superbee limiter gave reasonable solution in discontinuities but they do not reach the speed of Van Albada limiter. Therefore, third order Van Albada function is used as flux limiter in this work.

In order to improve the convergence characteristics of the Van Albada limiter, different values of ε^2 are implemented into the flux limiter function in Equation (4.69). The results obtained for these values of ε^2 are shown in Figure 5.18. ε^2 is a parameter which stops the activation of flux limiter function in smooth regions. Since flux limiters are efficient in discontinuous, ε^2 becomes an important characteristic of Van Albada flux limiter function.
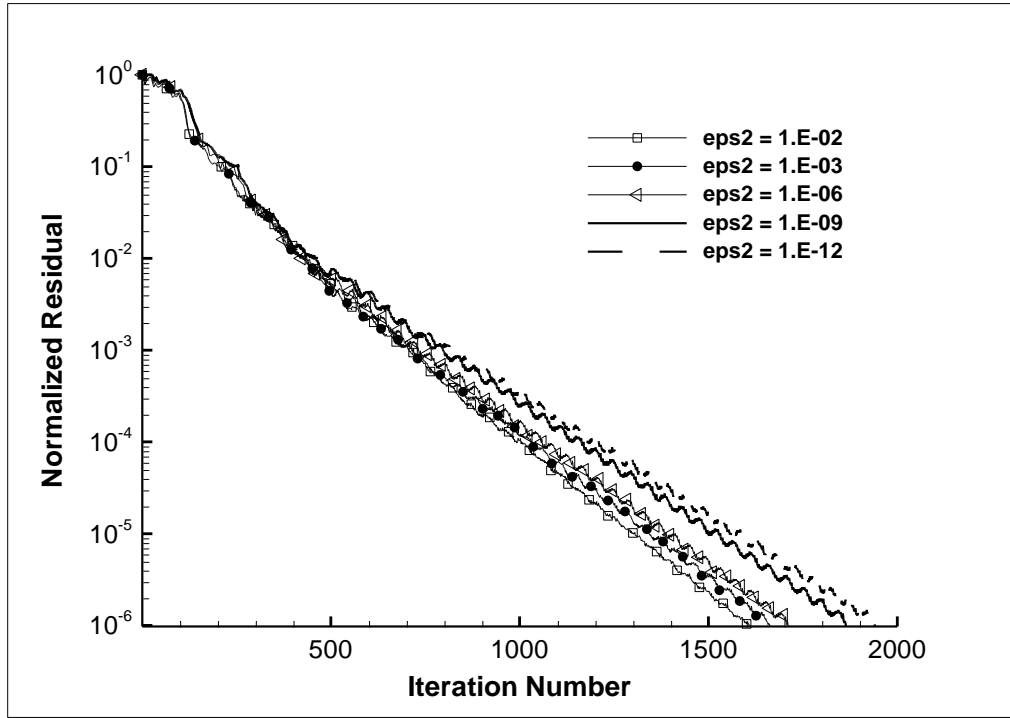
Figure 5.18 Normalized Residual Comparisons for Different Epsilons

Increasing the value of ε^2 causes an improvement in the convergence of the solution which can easily be noticed from the Figure 5.18. Considering very small numbers (1×10^{-12}), normalized residual meets the convergence condition at higher iteration numbers. For ε^2 values of relatively high i.e. 1×10^{-3}, the solution shows better convergence characteristics. However, increasing the values of ε^2 can cause some discrepancies in simulations around the shocks.

Although flux limiters may increase the convergence acceleration but, they may reduce the accuracy of the solutions, too. Here, applying flux limiters decreased the fluctuations in the residual and improved the convergence. However, the accuracy of the solutions dropped and solutions are approached the accuracy of first order. Therefore, the accuracy of second order scheme become slightly better than first order scheme which makes the use of flux limiters unreasonable in this study.

5.1.5 Fuel Injection Angle

Fuel-air mixing is one of the most important performance parameters of the scramjet engine. In order to increase the mixing efficiency, fuel is injected at different angles. The idea is to penetrate the fuel into the core flow as much as possible to reach a higher mixing efficiency and so to have a better combustion. For this purpose, mixing efficiency with different fuel injection angles with respect to the flow direction are analyzed and results are shown in the Figure 5.19. The mixing efficiency of the reaction mechanism can be defined as [9]:

$$\eta_m = \frac{\int Y_r \rho(\boldsymbol{v}.\boldsymbol{n})dA}{\int Y \rho(\boldsymbol{v}.\boldsymbol{n})dA} \qquad (5.1)$$

where, Y is the mass fraction of the fuel and Y_r is mass fraction of the reactant which is least available i.e. the reactant that would react if the reaction were completed. In this study, the reactant of the fuel (Ethylene) is oxygen.
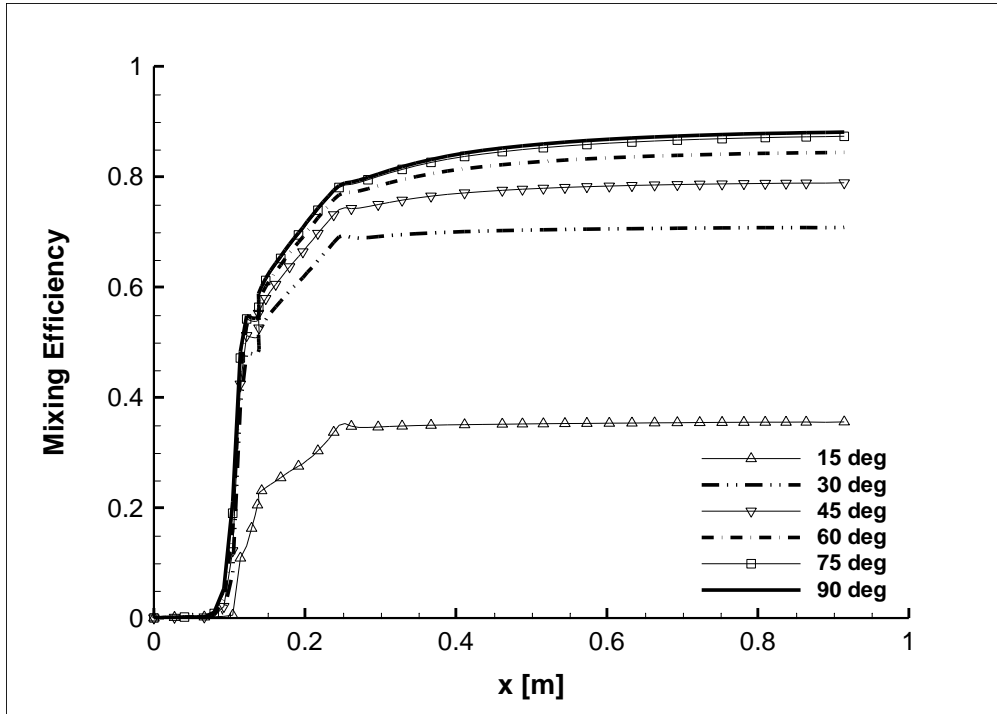

Figure 5.19 Mixing Efficiency for Different Fuel Injection Angles in Flow Direction

From the Figure 5.19, it can be seen that increasing the fuel injection angle in the flow direction increase the mixing efficiency of the fuel-air. This is expected as by increasing the injection angle fuel penetrates to the core flow at high rates. However, after a certain angle (approximately 60deg), increase in the efficiency becomes slow. Maximum mixing efficiency is reached at 90 degrees where injection is perpendicular to the flow direction. Generally, Injection fuel perpendicular to the flow cause problems of flame holding and instability. However, the recession of cavity after the fuel injection stabilizes the flow and improves flame holding.

In addition, fuel injection is done against to the flow direction and results are shown in Figure 5.20. Same as the injection in flow direction, mixing efficiency of the injections in reverse angles are also less than 90 degree injection.
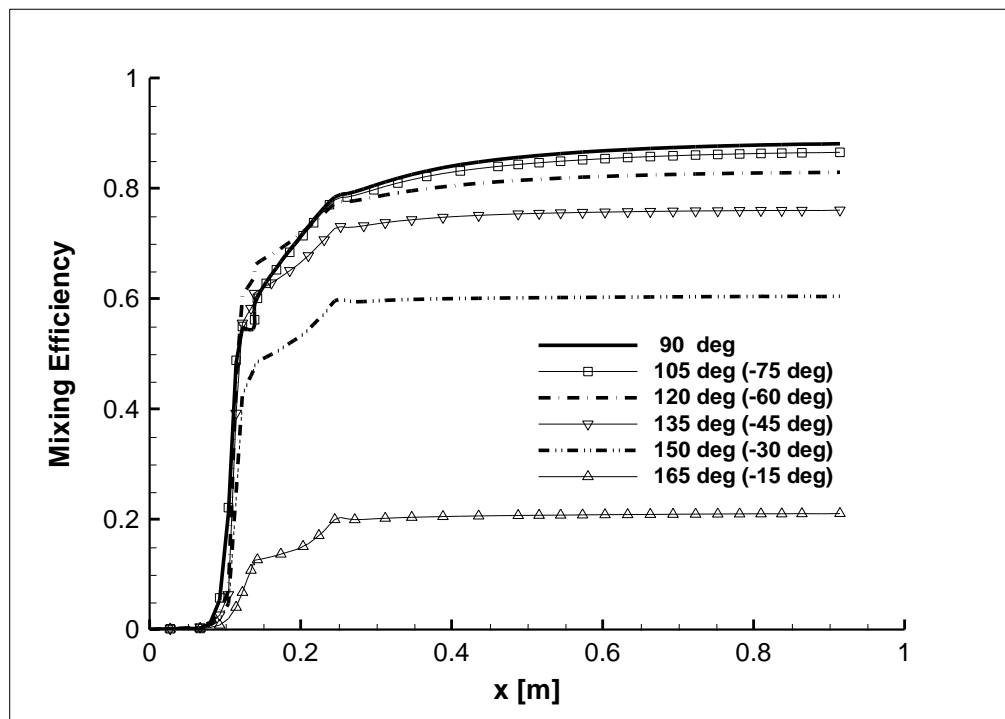

Figure 5.20 Mixing Efficiency for Fuel Injection Angles against the Flow Direction

Comparing the injection angles, it can be concluded that the injection in flow direction gives better efficiencies for same angles at reverse angle. Figure 5.21 shows that injecting fuel against the flow direction results in deflection of the flow from the

81

cavity region and so an increase in the flow velocity over the cavity. This contradicts the principle of the use of cavities where slowing down the velocity to create recirculation region and so increasing the mixing efficiency is intended. Therefore, fuel injections in the flow direction are better to increase the mixing efficiency.
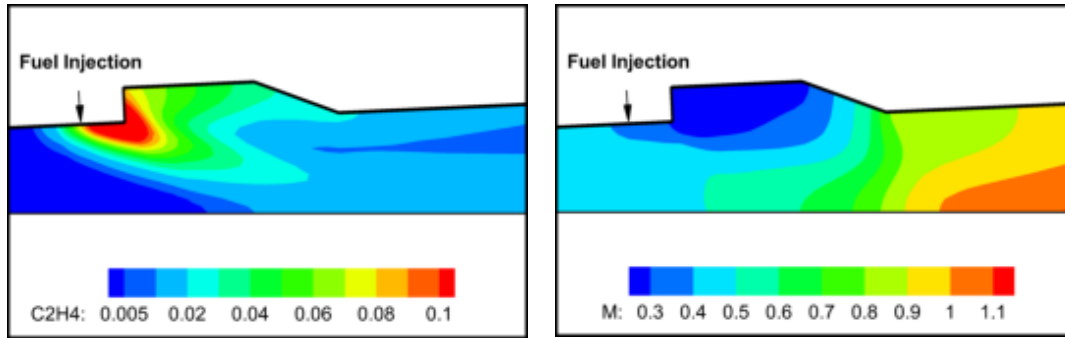
a) Fuel Injection Angle of 45 degree
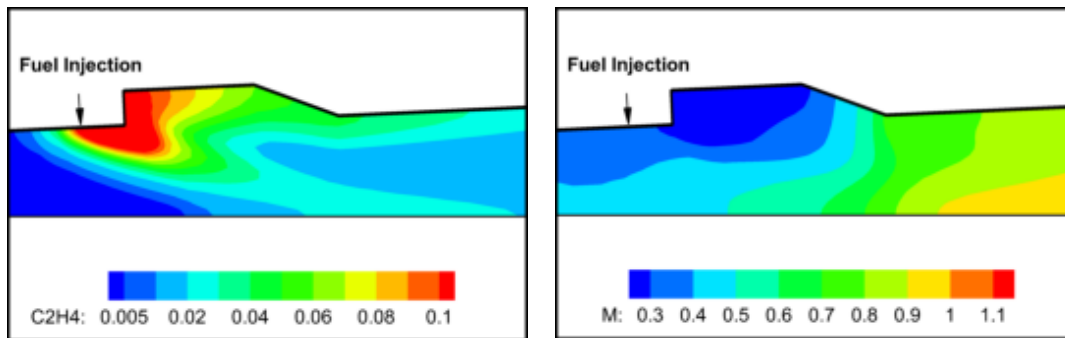
b) Fuel Injection Angle of 90 degree
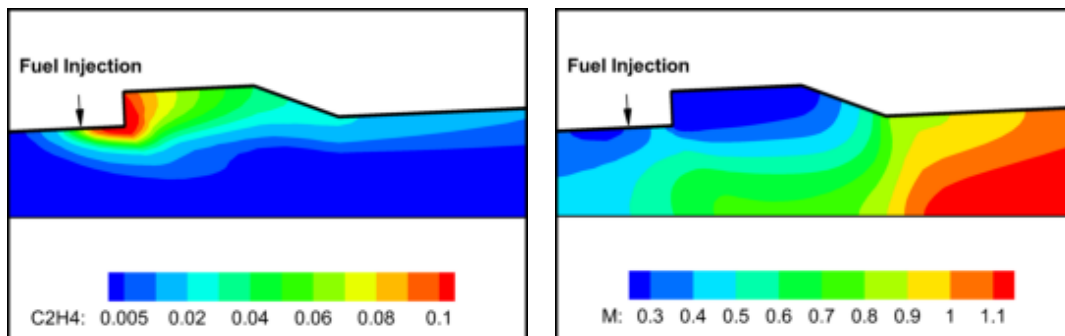
c) Fuel Injection Angle of 135 degree (-45 degree)

Figure 5.21 Ethylene (Fuel) and Mach Contours for Different Fuel Injection Angles

5.1.6 Downstream Fuel Injection

Fuel-air mixing and combustion is one the most important problems of the scramjet combustor design. Mixing of the fuel with air entering the combustor at high speeds in molecular level is a difficult process. Cavity recessed scramjet combustor is one of the methods developed to increase the efficiency and provide stable flame holding. Some methods are proposed to increase the mixing efficiency even further using cavity-based combustor. One of the methods proposed is to inject fuel downstream of the cavity beside the upstream fuel injection (Figure 5.22).
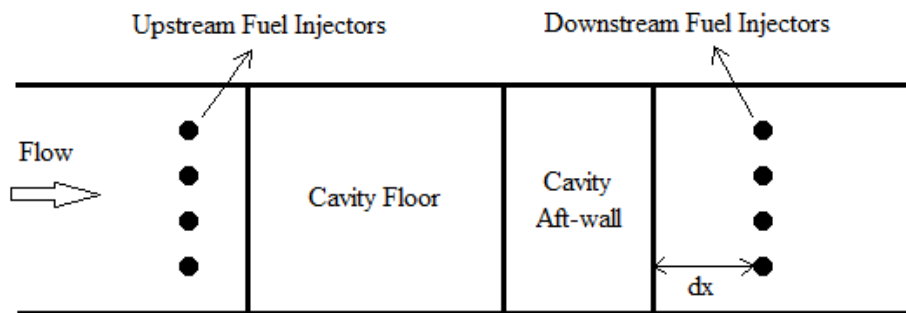

Figure 5.22 Both Upstream and Downstream Fuel Injection Pattern

The idea behind the design of the combustor with an additional fuel injection is to make use of the slowed down flow and increased temperature in the cavity beyond the upstream fueling. Decreased velocity of the flow after the cavity is thought to increase the mixing efficiency and the increased temperature in the cavity might increase the combustion effectiveness. Here, a study is conducted to evaluate the effect of proposed method on mixing efficiency of the combustor. Fuel is injected from different distances starting from the edge of the cavity aft-wall (dx) i.e. downstream of the cavity aft-wall. The mixing efficiencies are plotted for different downstream fuel injection locations. It should be noted that the fuel injections in this configuration is done both from the upstream and downstream fuel injectors simultaneously.
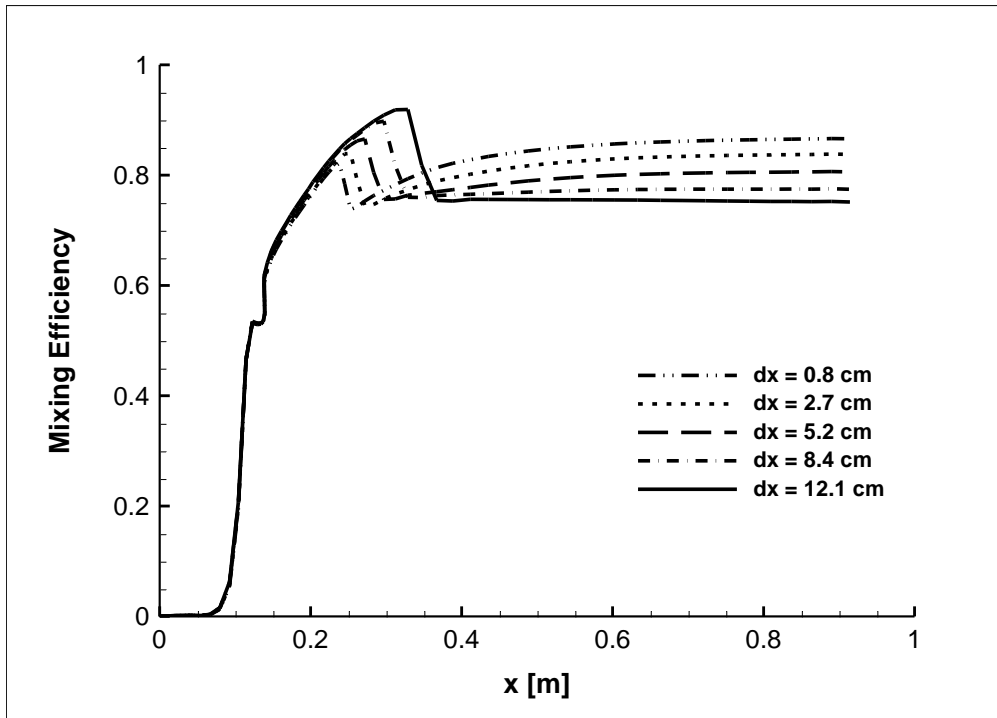
Figure 5.23 Mixing Efficiency for Different Downstream Fuel Injection Locations

As it can be seen from the Figure 5.23, mixing efficiency is reduced at some point with downstream fuel injection. This point corresponds to a location just before the injectors. But, again after the fuel injection the mixing efficiencies are raised for the configurations where the injection distance is near to the edge of the cavity aft-wall. However, for far downstream injections, mixing do not experience an improvement and it remains approximately same through the combustor exit. One of the reasons behind the poor performance of secondary fueling far downstream is that there is not much space left in the combustor to continue the combustion process in the combustor and reactions might continue to occur in the nozzle which is undesirable. The best mixing efficiency is achieved for the configuration where the fuel injectors are placed just after the cavity ($dx = 0.8\ cm$). This can be due to two reasons; first, peak temperature is reached in the cavity and so secondary fueling near the cavity takes the most advantages of the high temperature and second, Injectors being close to cavity means that there is much space left beyond the fuel injection so that combustion process can continue further downstream.

Now that solutions are obtained for configurations with only upstream fuel injection and with both upstream and downstream fueling, the comparison of their mixing efficiencies are plotted in Figure 5.24. It can be deduced that by addition of downstream fuel injection mixing is improved in the cavity compared to only upstream fueling. However, after the secondary fueling location the mixing efficiency is reduced up to the point where the fuel injected from the downstream injector again mixes with the air. Close to the combustor exit, the mixing rate of the fuel-air is almost similar for both cases.
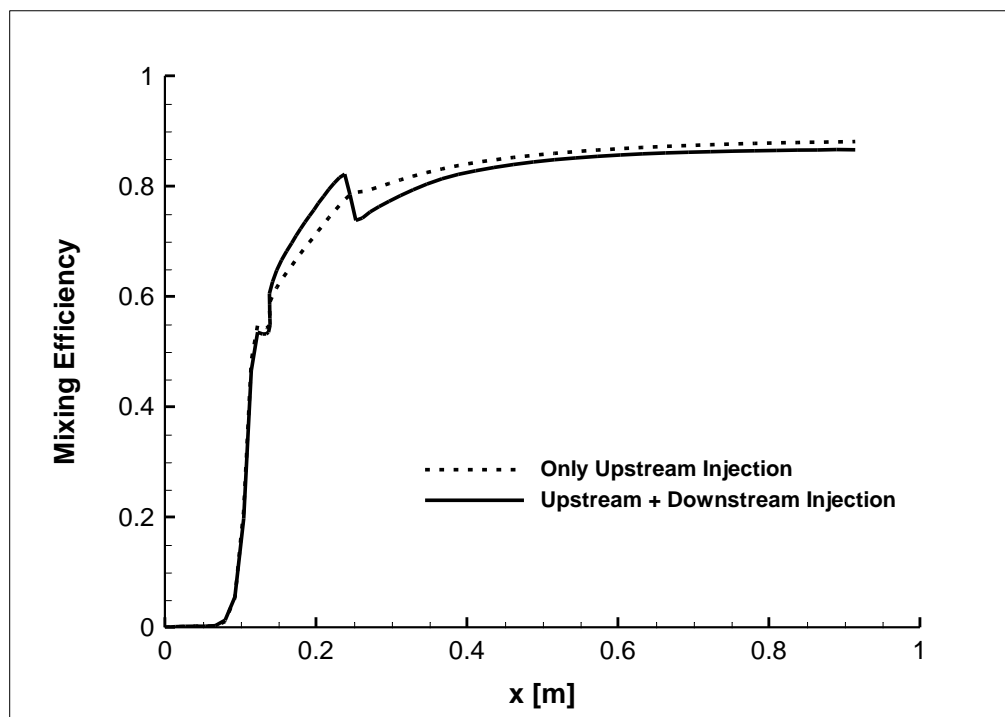
Figure 5.24 Effect of Downstream Fuel Injection on Mixing Efficiency

Different contour plots for cases of only upstream fueling and for simultaneous upstream and downstream fuel injections are shown in Figure 5.25 and Figure 5.26. Difference in these can be seen by comparing flow variables of density, pressure, temperature and Mach and also, mass fraction of species included in the reaction mechanisms. Addition of the downstream fueling do not contribute to the mixing efficiency of the combustor and so, this configuration is not very efficient to be used.
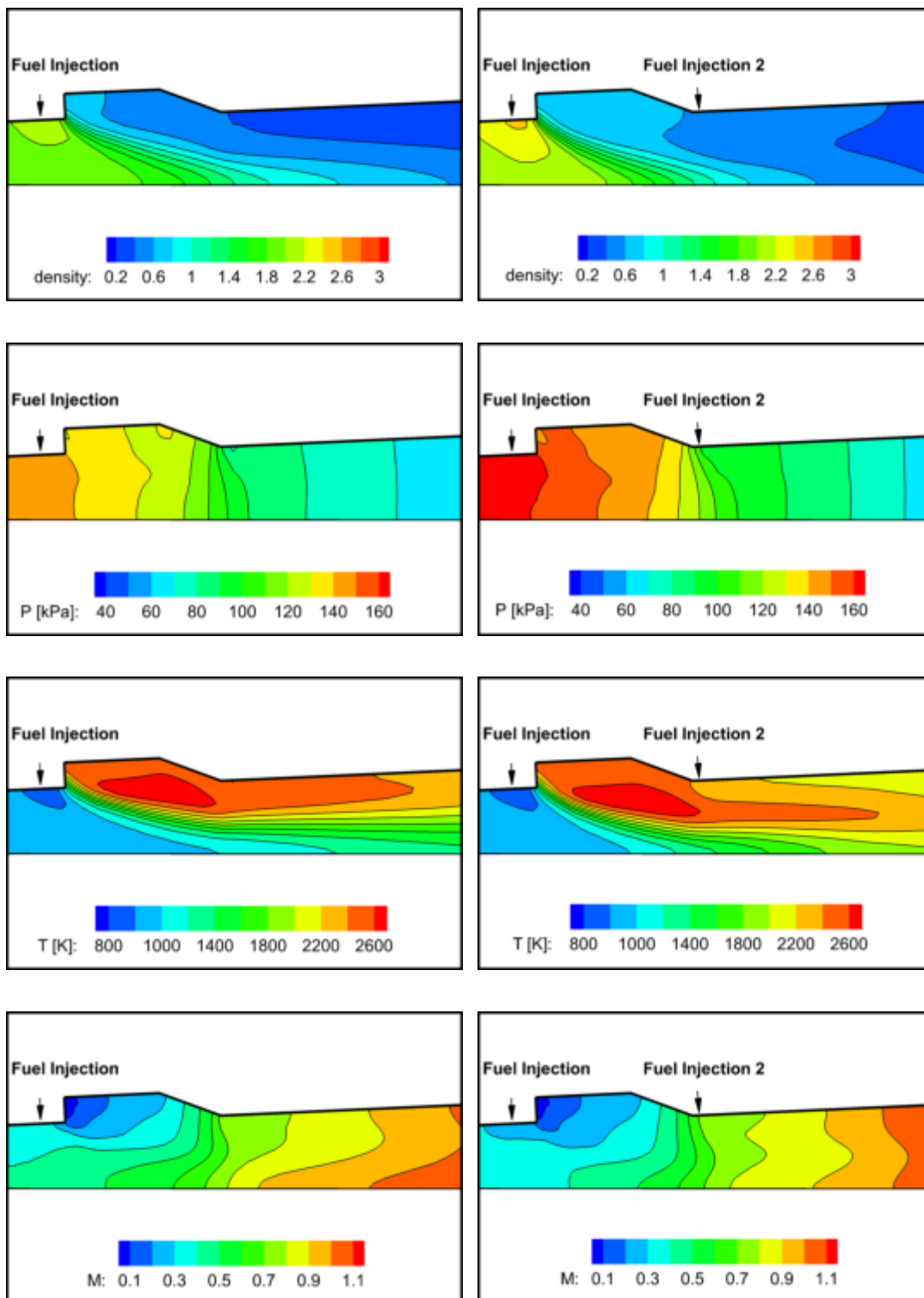
a) Only Upstream Injection   b) Upstream and Downstream Injection

Figure 5.25 Comparison of Two Injection Patterns by Flow Variable Contours
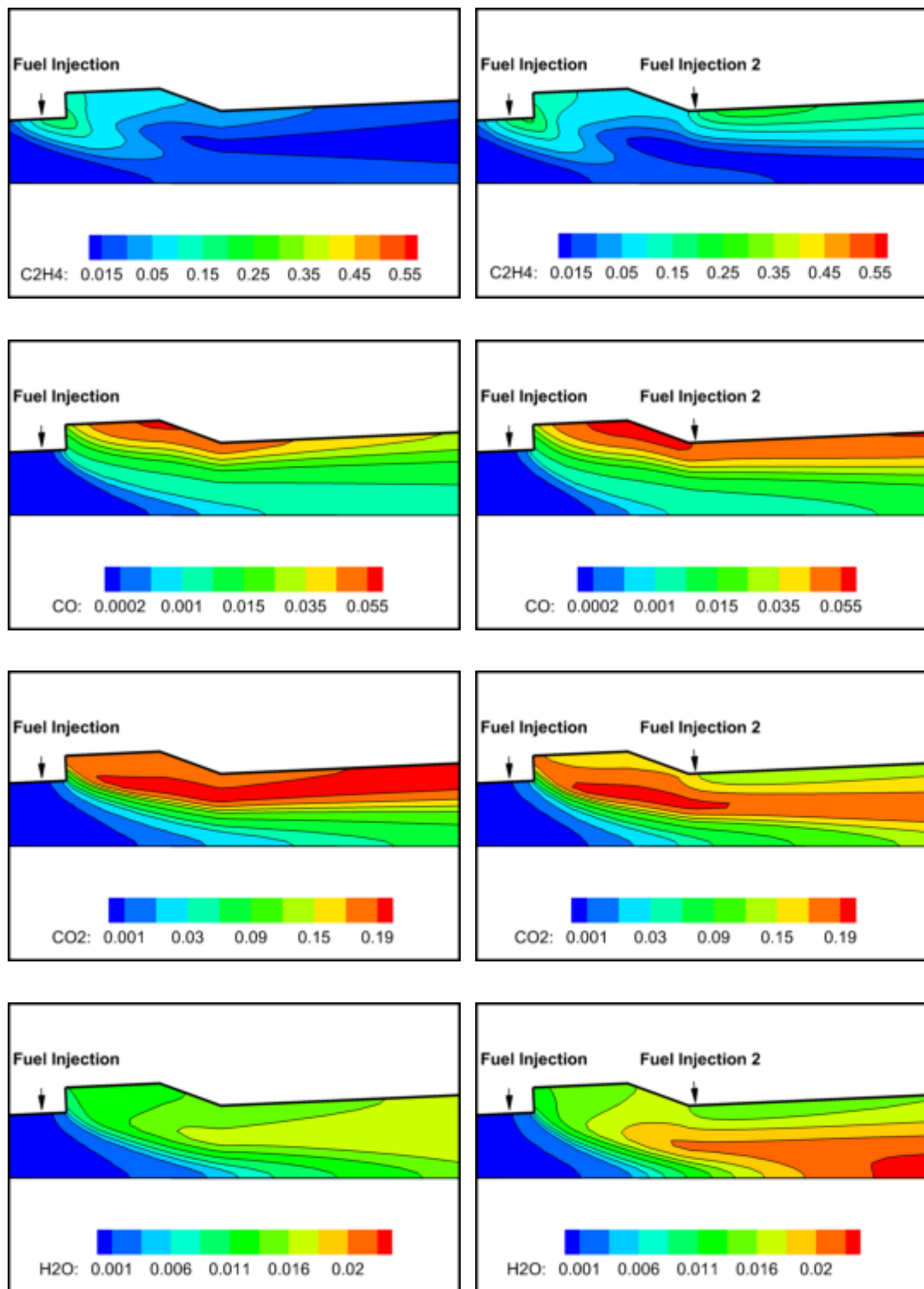
a) Only Upstream Injection   b) Upstream and Downstream Injection

Figure 5.26 Comparison of Two Injection Patterns by Species' Mass Fraction

5.2 Viscous Flows

In this part, three dimensional coupled Navier-Stokes and finite rate chemical reaction model equations are solved. Solutions for the analysis of the flow passing through scramjet combustor is presented. Viscous effects of the flow are included in the equations. Therefore, physics of the flow is more accurate and modeling of the scramjet combustion chamber is more precise. Viscous effects in the vicinity of the boundaries cause the formation of boundary layers. The no-slip condition is applied for the wall boundaries i.e. velocity at the wall boundaries are equaled to zero. In order to capture the effects of no slip boundary condition precisely, the grid resolution should be improved near the boundaries. In other words, grids generated must be dense in the vicinity of the wall boundaries. The meshes generated for the inviscid flow are not applicable and suitable for the viscous flows and so viscous meshes are generated for this part.

5.2.1 Grid Refinement for Viscous Flow Case

In order to study the sensitivity of the solutions to grid resolution, mesh refinement study is done. The generated meshes are categorized as coarse, medium and fine. Solutions obtained using different mesh types are compared and dependency of the solutions on resolution of these grids are examined. The goal is to reach the best possible accuracy in the solution for the least grid resolution. This leads to get the solution with enough accuracy by providing the lowest computational effort and time. Using very fine grid resolutions possibly gives the most accurate solutions. However, the amount of CPU time required to achieve this accuracy is very high and as a result makes the computation process extremely inefficient.

Table 5.7 Generated Meshes with Different Resolutions for Viscous Flows

Grid Resolution	Number of Nodes (i x j x k)	Number of Cells in Half Domain
Coarse	94x41x32	57,660
Medium	120x51x40	116,025
Fine	142x61x48	198,810

Since the scramjet combustor is symmetrical in the y-direction, the solutions domain is split into two parts. Half of the solution domain is solved and the symmetry boundary condition is applied on the symmetry plane (j-plane). Halving the solution domain reduces the CPU time required to solve the whole solution domain and so makes the computation more efficient. This is crucial especially in solving Navier-Stokes equations where computational effort is great. Here, the analysis of the flow through scramjet combustor will be done using the generated meshes. The grid resolution for the medium mesh is shown in Figure 5.27 for the whole domain. The unit directions of i, j and k are in the x, y and z directions, respectively.
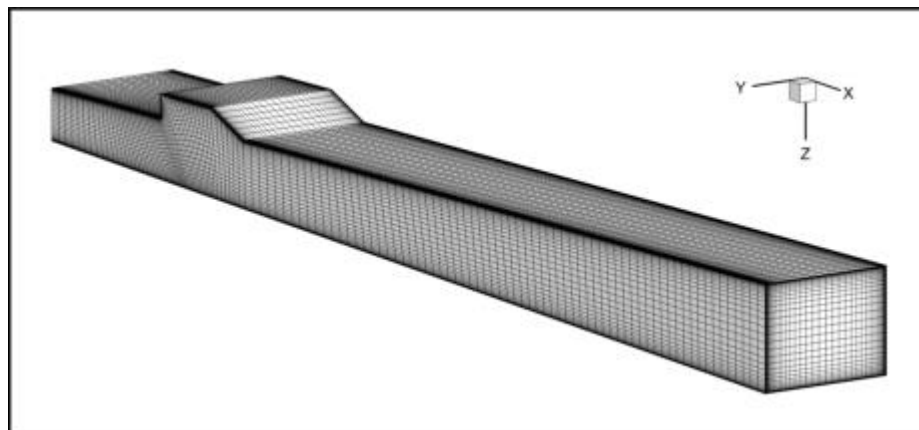

Figure 5.27 Medium Grid Size Generated for Viscous Flows

Before proceeding with the solution, the extent of the validity of the developed code must be affirmed. For this purpose, the solutions obtained using the developed code for the present study is compared with the experimental data from Lin et al. [26]. Moreover, the numerical solutions given by Lin et al. [26] are used as an additional reference data for the analysis of the scramjet combustor. The sensitivity of the solutions to the grid resolution are examined by comparing the experimental and other numerical data. The experiments are done to simulate the flight conditions of Mach 4.5. For this purpose, Mach number of 2.2 and total temperature of 950 K is produced at the isolator inlet. Lin et al. performed the numerical analysis using CFD++ code. In their simulations, RANS equations are employed with two-equation cubic $\kappa - \varepsilon$ turbulence model. The pressure data from these experimental and numerical data are compared with the pressure distributions of the present study for viscous flows in Figure 5.28.
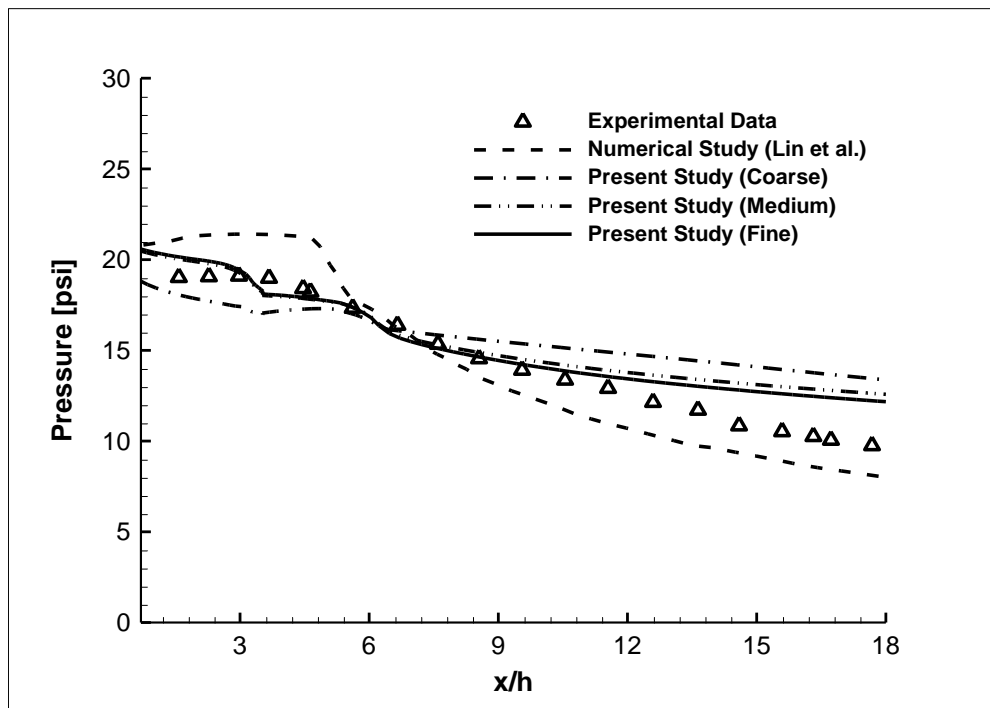

Figure 5.28 Comparison of Pressure Distribution with Experimental and Numerical Data (Viscous Flows)

As it can be seen from the Figure 5.28, the pressure distributions obtained by the present study for viscous flows are in a relatively good agreement with the experimental data. However, the pressure values are higher downstream of the cavity. This can be due to the fact that in laminar flows, the velocities are small near the wall boundaries and so the pressures are high. However, in turbulent flows, the pressure values are lower in the boundary layer region, Therefore, adding turbulence models can decrease the pressure values at the walls and consequently the pressure distribution in the cavity downstream may be obtained to be in a better agreement with the experiments.

Pressure distribution approaches the experimental data as the resolution of grids are increased. Pressure distribution obtained for coarse mesh deviates from the experimental in greater amount than the medium and fine meshes. The solution for the medium and fine meshes are very similar and it can be concluded that mesh dependency of the solution becomes insignificant from medium to fine meshes. However, CPU time used to obtain solutions for fine mesh is very high compared to medium mesh (Table 5.8). Therefore, performing computations on medium size mesh is more efficient.

Table 5.8 Variation of CPU Time for Different Grid Resolutions

Grid Resolution	CPU time
Coarse	17827 s
Medium	30635 s
Fine	57187 s

Convergence characteristics of medium grid resolution for the viscous flow is shown in Figure 5.29.
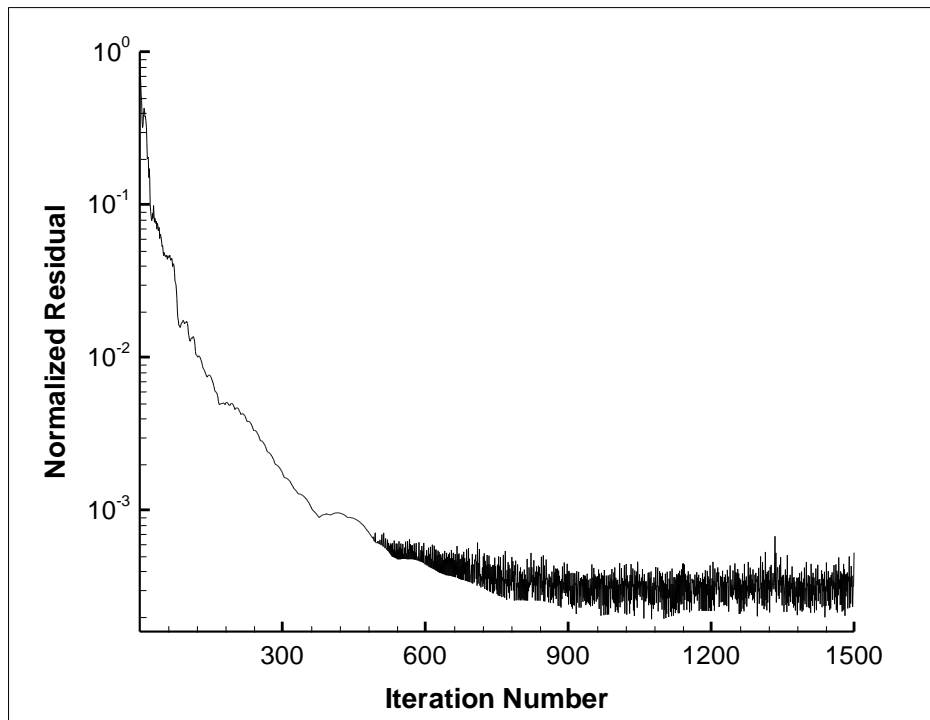
Figure 5.29 Convergence History of the Viscous Flow Solution (Medium Mesh)

The residual of the solutions obtained for the viscous flows are decreased more than three orders. Convergence starts to oscillate after the three orders reduction and literally convergence stops. The oscillations in the convergence pattern can be due to many reasons. Obtaining steady state solutions are difficult for flows with unsteady behavior. Injection of the fuel can cause oscillation in the solutions and prevent convergence. Moreover, combustor contains discontinuities in geometry where the cavity is recessed in the wall. Presence of the cavity creates a recirculation region where backward flows are generated. These can affect the convergence characteristics of the solution.

In addition, considering the coupled equations of Navier-Stokes and chemical reactions, the no-slip boundary condition can cause oscillation in the vicinity of the boundaries. Therefore, fluctuations in the residual can be explained by large discontinuities in the flow and geometry and problems may be related to numerical and CFD methods or approaches.

5.2.2 Comparison of First and Second Order Schemes

In this part, the solutions obtained for viscous flows using first and second order schemes are given. To study the effect of using different schemes, solutions obtained for viscous flows are compared. For this purpose, variation of different flow variables and species' mass fraction are plotted in the cavity region of the combustor. The cavity region is the most important part of the combustor because of discontinuities in the geometry and flow (shocks, fuel injection and etc.) which occurs in this region. The cavity region is shown in Figure 5.30.
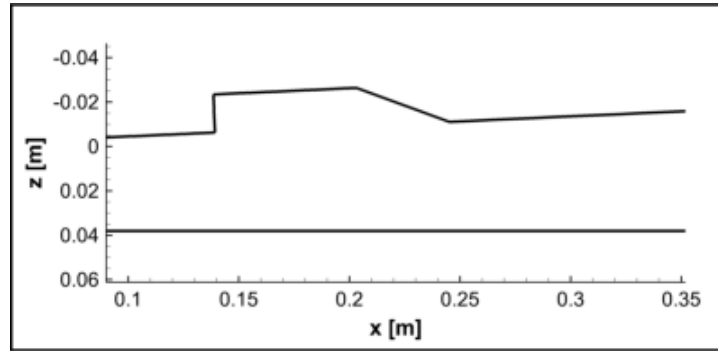

Figure 5.30 Cavity Section of the Combustor (Viscous Flow Case)

In Figure 5.31, 2-D distribution of flow variables and species' mass fraction at different locations in the combustor cavity region is shown. Moreover, variation of these variables are given by contour plots in Figure 5.32 and Figure 5.33.

From 2-D distributions, it can be seen that the variation of flow variables are sharper in the second order schemes. In other words, second order schemes capture the abrupt changes occurred because of the flow or geometry discontinuity. Moving from the wall boundaries into the core flow, the changes in the flow variables such as Mach number become greater in second order scheme solutions. Near to the walls, the variation is very small while reaching high values in the core flow. In other words, the changes occur sharply. However, the variation of the flow variables and species are gradual starting from the walls to the core flow in first order schemes.
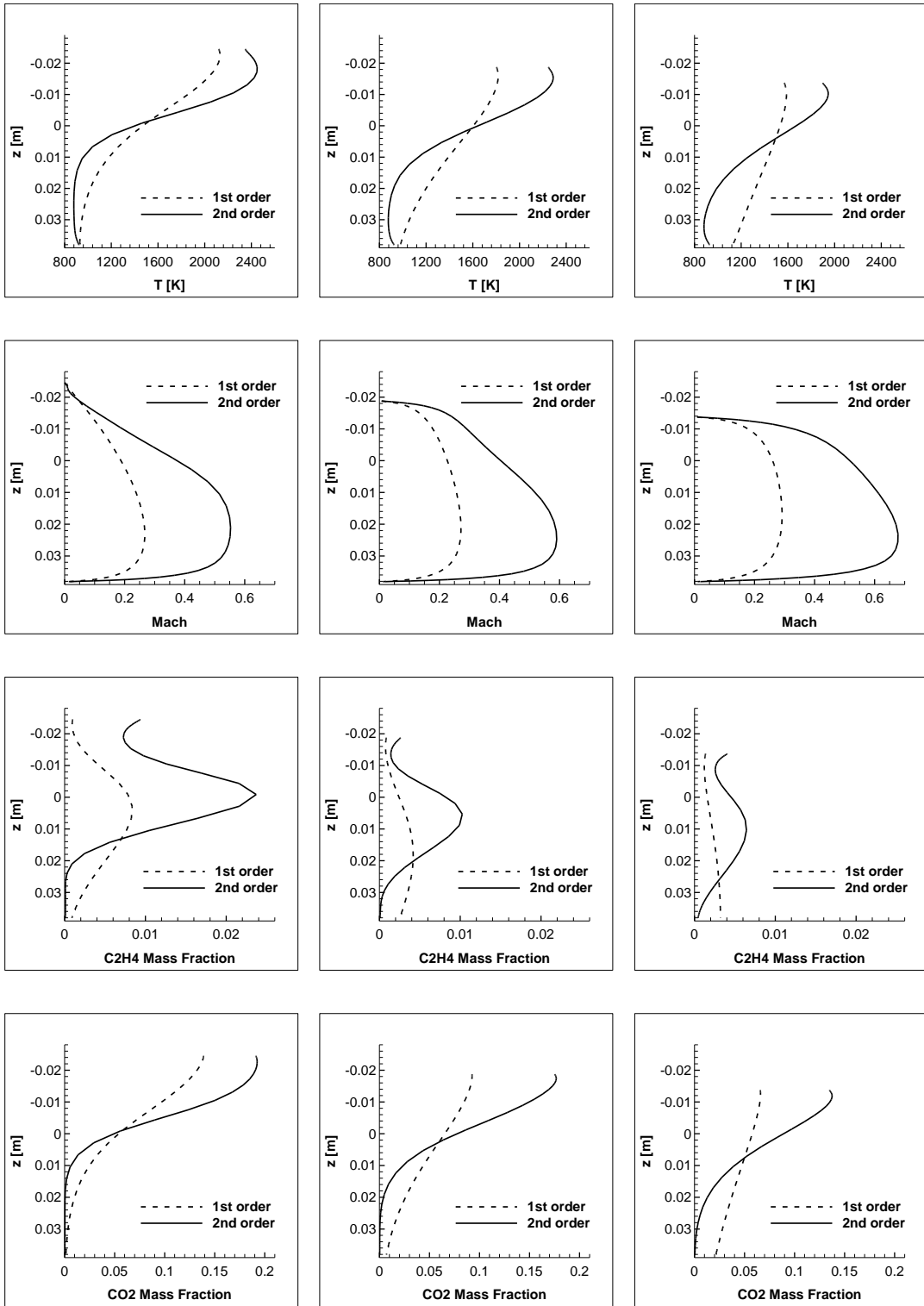
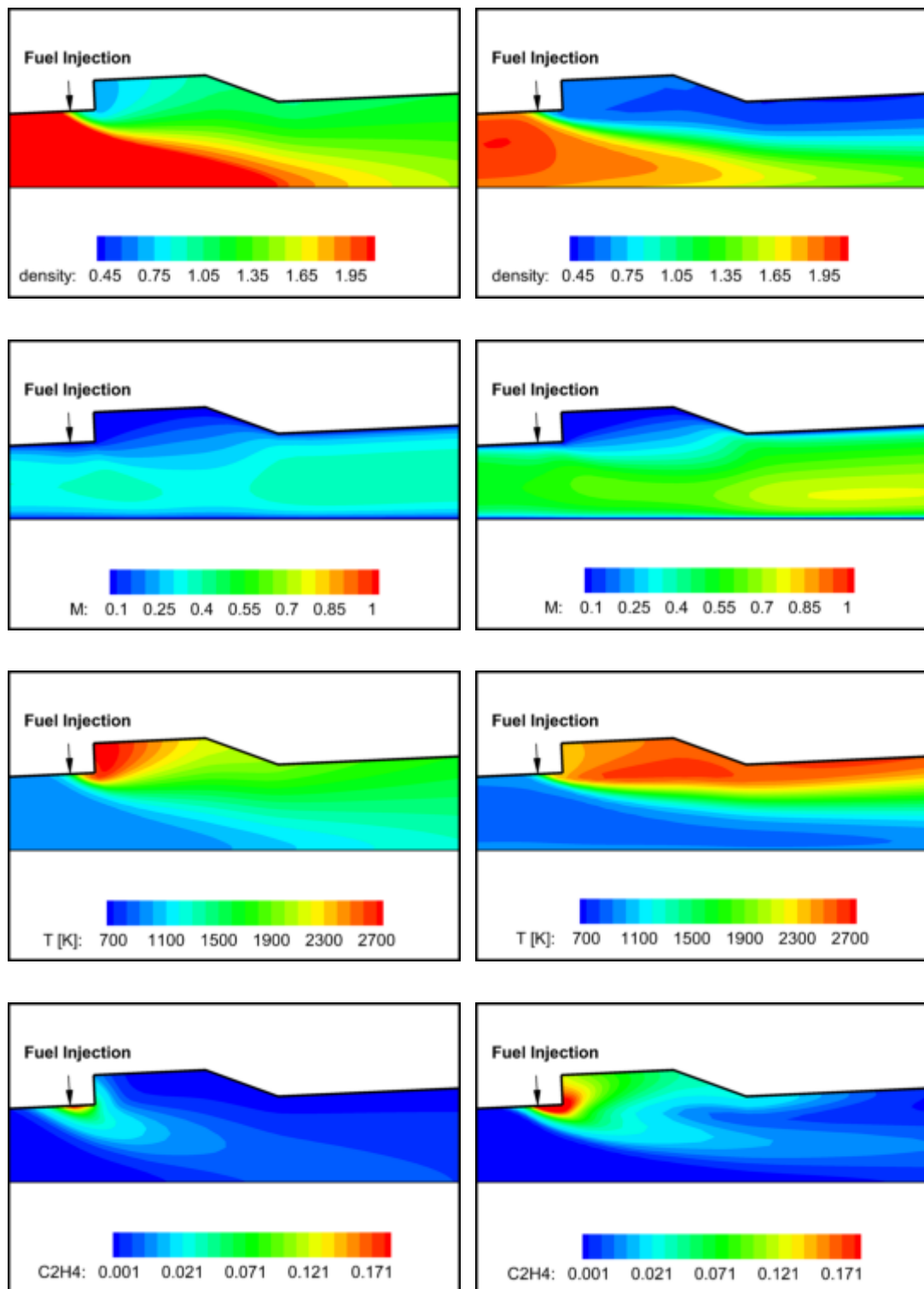x = 0.17 m   x = 0.23 m   x = 0.31 m

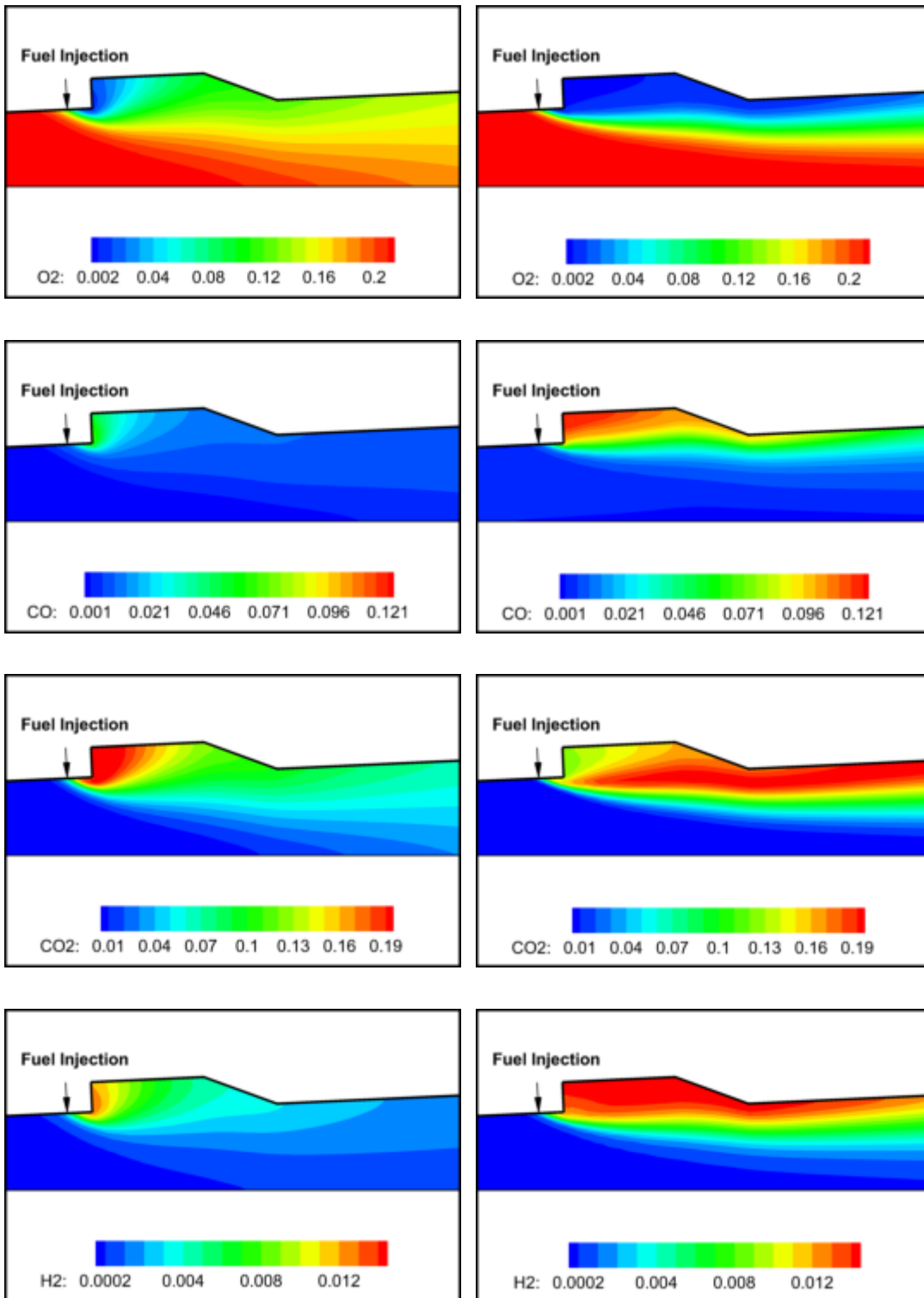Figure 5.31 2-D Distribution of Flow Variables at Different x Locations

94

a) First order scheme   b) Second Order Scheme

Figure 5.32 Comparison of 1ˢᵗ and 2ⁿᵈ Order Schemes by Contours

a) First Order Scheme   b) Second Order Scheme

Figure 5.33 Comparison of 1st and 2nd Order Schemes by Species' Mass Fraction

It can be observed from Figure 5.32 and Figure 5.33 that solutions obtained from second order schemes present precise information about the thermodynamic properties and chemical species. Small changes in flow variables are more subtle in second order schemes. First order schemes give good accuracy in smooth regions as it can be seen from cavity upstream and fuel injection location. The presence of discontinuities in the geometry and flow pattern cause a reduction in the exactness of the first order scheme. Cavity creates a 90 degree deflection angle (geometry-wise) and shocks create sharp changes in the values of density, pressure and so on. Therefore, second order schemes are more accurate to be used in complex geometries and flows.

5.2.3 Reaction Mechanism Analysis

In order to analyze the performance of the chemical reaction model, 1-D mass flux weighted values of temperature, mixing efficiency and species' mass fractions are calculated from their three dimensional distributions and shown in Figure 5.34 and Figure 5.35. It can be concluded that temperature and mixing efficiency are dependent values. Starting from the fuel injection location, both temperature and mixing efficiency rises. This is anticipated as reactions are dependent on the temperature. Increase in the mixing efficiency becomes very gradual downstream of the cavity. This is due to the fact that temperature drops at combustor downstream.
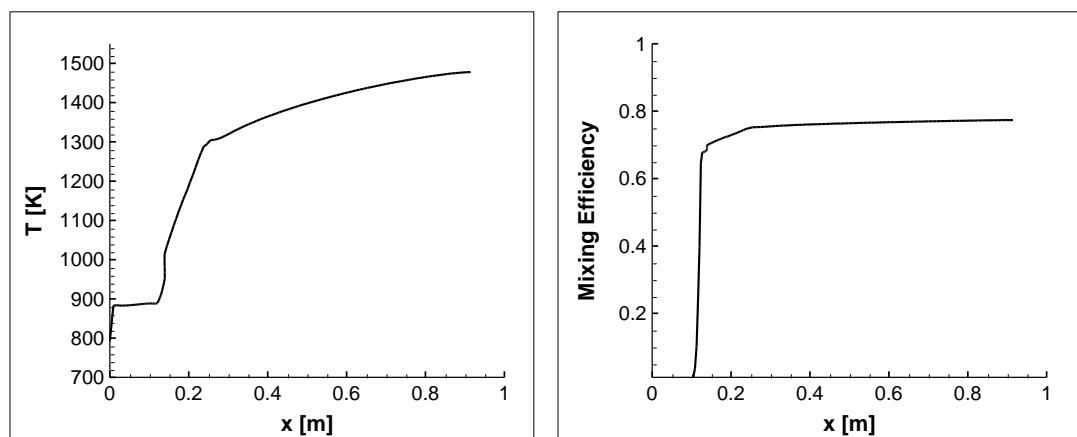

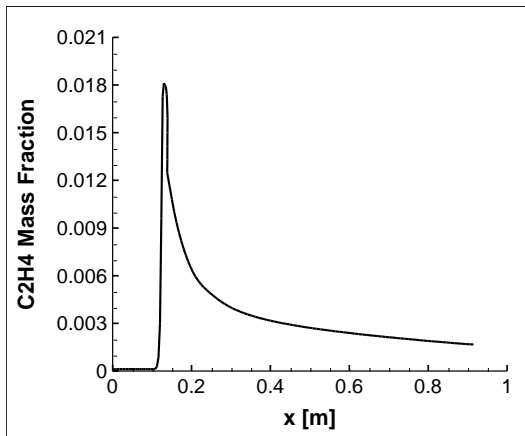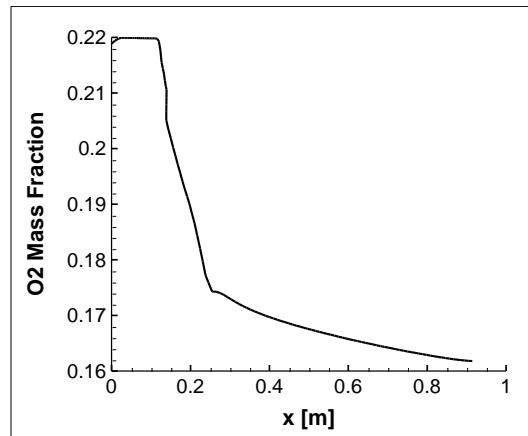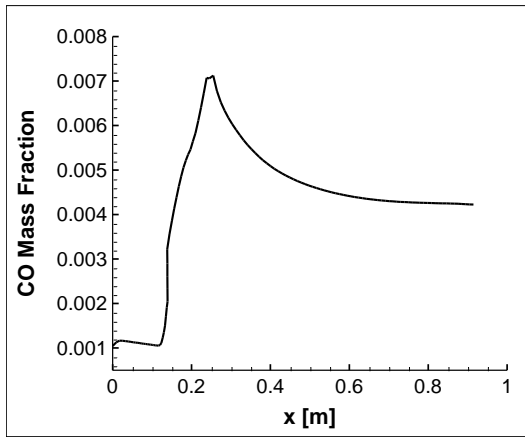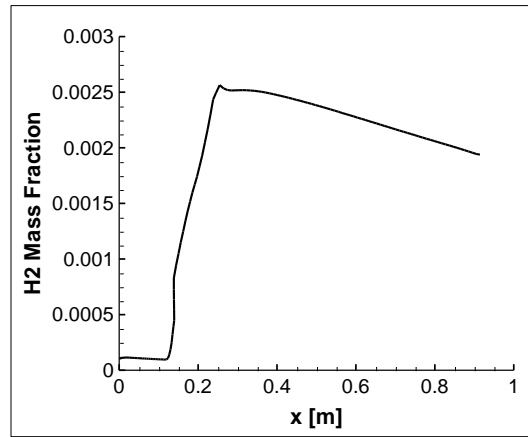Figure 5.34 Variation of Mass flux Weighted Temperature and Mixing Efficiency
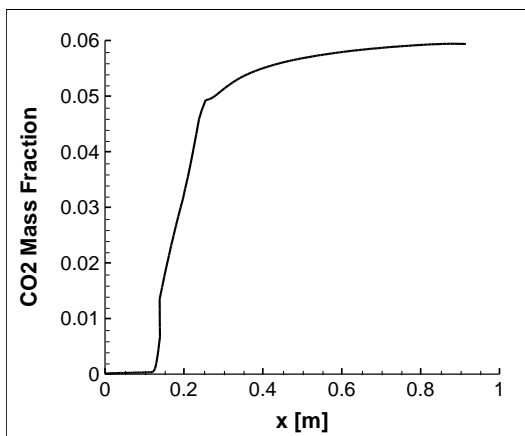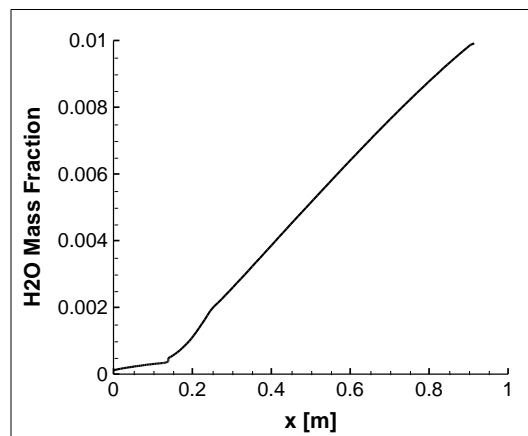
a) Ethylene

b) Oxygen

c) Carbon Monoxide

d) Hydrogen

e) Carbon Dioxide

f) Hydrogen Dioxide

Figure 5.35 Mass Flux Weighted 1-D Variation of Species through Combustor

As it can be seen from the Figure 5.35, fuel is injected approximately 0.1 meters from the combustor inlet upstream of the cavity. After the injection of ethylene (C_2H_4) chemical reactions takes place. Fuel is reacted with oxygen (O_2) and carbon monoxide (CO) and hydrogen (H_2) are produced. It can be clearly seen that mass fraction of oxygen reduces after the injection of the fuel. In addition, increase in the mass fraction of hydrogen stops and then it continuously drops downstream of the cavity. This is reasonable since produced hydrogen reacts with oxygen to give hydrogen dioxide (H_2O) as product. Therefore, production of hydrogen dioxide continuously increases up until the combustor exit. Moreover, carbon monoxide reacts with oxygen too and carbon dioxide (CO_2) is generated. Thus, production of the carbon dioxide is dependent on the reaction of ethylene with oxygen to produce the carbon monoxide. Increase in the mass fraction of carbon dioxide becomes very slow downstream because of the slow reaction of ethylene-oxygen in this region.

5.2.4 Fuel Injection Angle

Because of the low residence time of the flow in combustion chamber of the scramjets, fuel-air mixing becomes a crucial problem. Beside to use of the cavities to increase the mixing efficiency, different methods are also employed to increase the fuel-air mixing efficiency even further. Injecting fuel at different angles is one of the methods proposed in this purpose. By changing the injection angle it is intended to penetrate the fuel into the core flow in a great amount to increase the mixing of the species. A Study is conducted to evaluate the effectiveness of this idea. As a first step, fuel is injected at different angles in the flow direction and mixing efficiencies are obtained as shown in Figure 5.36. Furthermore, fuel is injected at different angles against the flow direction. The idea is that by injecting fuel in the opposite direction, increasing the collision of the species and so get a better mixing efficiency. The mixing efficiencies obtained for viscous flows by injecting fuel against the flow direction is shown in Figure 5.37.
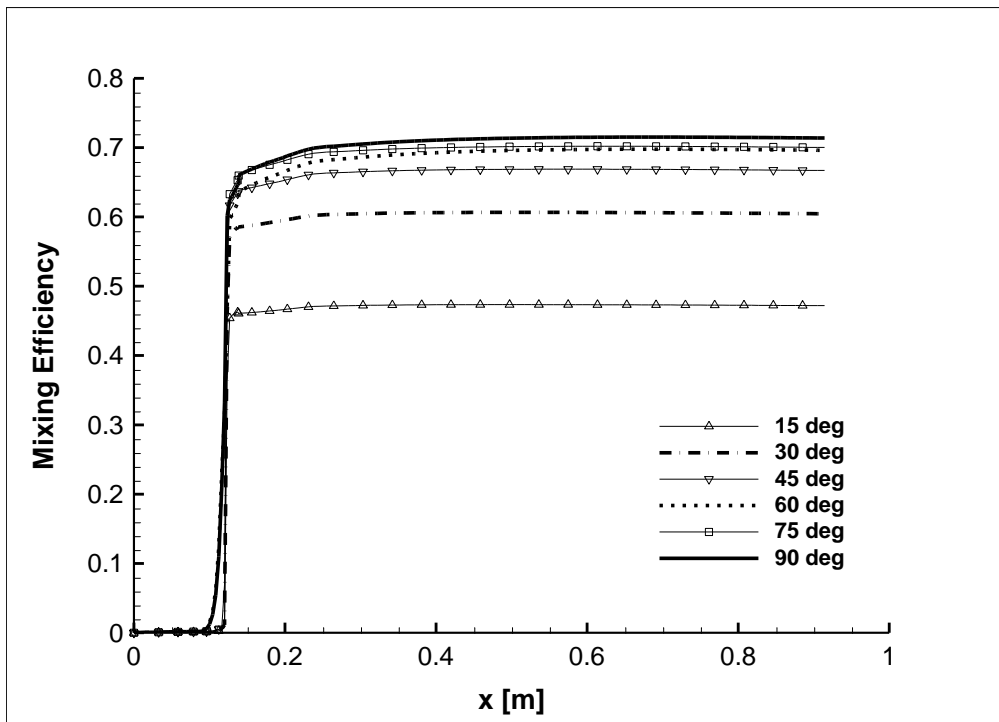
Figure 5.36 Mixing Efficiency for Different Fuel Injection Angles in Flow Direction
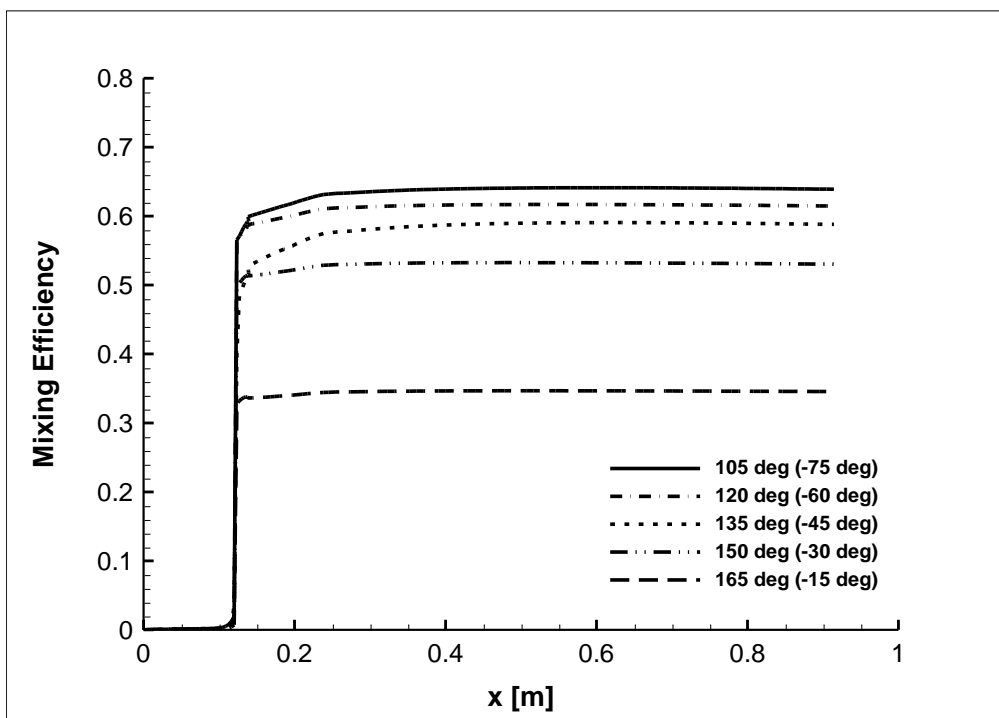

Figure 5.37 Mixing Efficiency for Fuel Injection Angles against the Flow Direction

From Figure 5.36, it can be seen that by increasing the flow injection angle in the flow direction, mixing efficiency is also increased. The maximum efficiency reaches for the configuration in which the fuel is injected at 90 degrees. This is due to the increased penetration of the fuel into the core flow at this angle.

Likewise, increasing the fuel injection angle against the flow direction increases the efficiency of the fuel-air mixing as shown in Figure 5.37. However, comparing the efficiencies for different angle in both flow direction and against it shows that injection in the flow direction shows better performance. This is due to the fact that injecting the fuel against the flow direction causes a deflection in the high velocity core flow and prevents the flow from entering the cavity region. Therefore, the recirculation in the cavity region becomes barely efficient. The core flow reaches higher speeds without experiencing good mixing with the fuel and so poor efficiencies are achieved in these configurations.

5.2.5 Three Dimensional Visualization

In this part, three dimensional visualization of the solutions are given in the Figure 5.38 and Figure 5.39. Density, pressure, temperature and Mach variation through the combustion chamber is shown. In order to have a better visualization of these values three dimensional contours are shown for half of the domain from the combustors half plane (symmetry plane). Therefore, the real width of the combustor is two times bigger than the shown figures. In addition to thermodynamic properties, variation in the mass fraction of the species are shown in three dimensional figures. Effect of the cavity placement in the combustor can be seen from the figures where the chemical reactions occurred mostly in the cavity region. Mach number decreased in the cavity and temperature improved the flameholding and mixing efficiency of the fuel-air reaction.
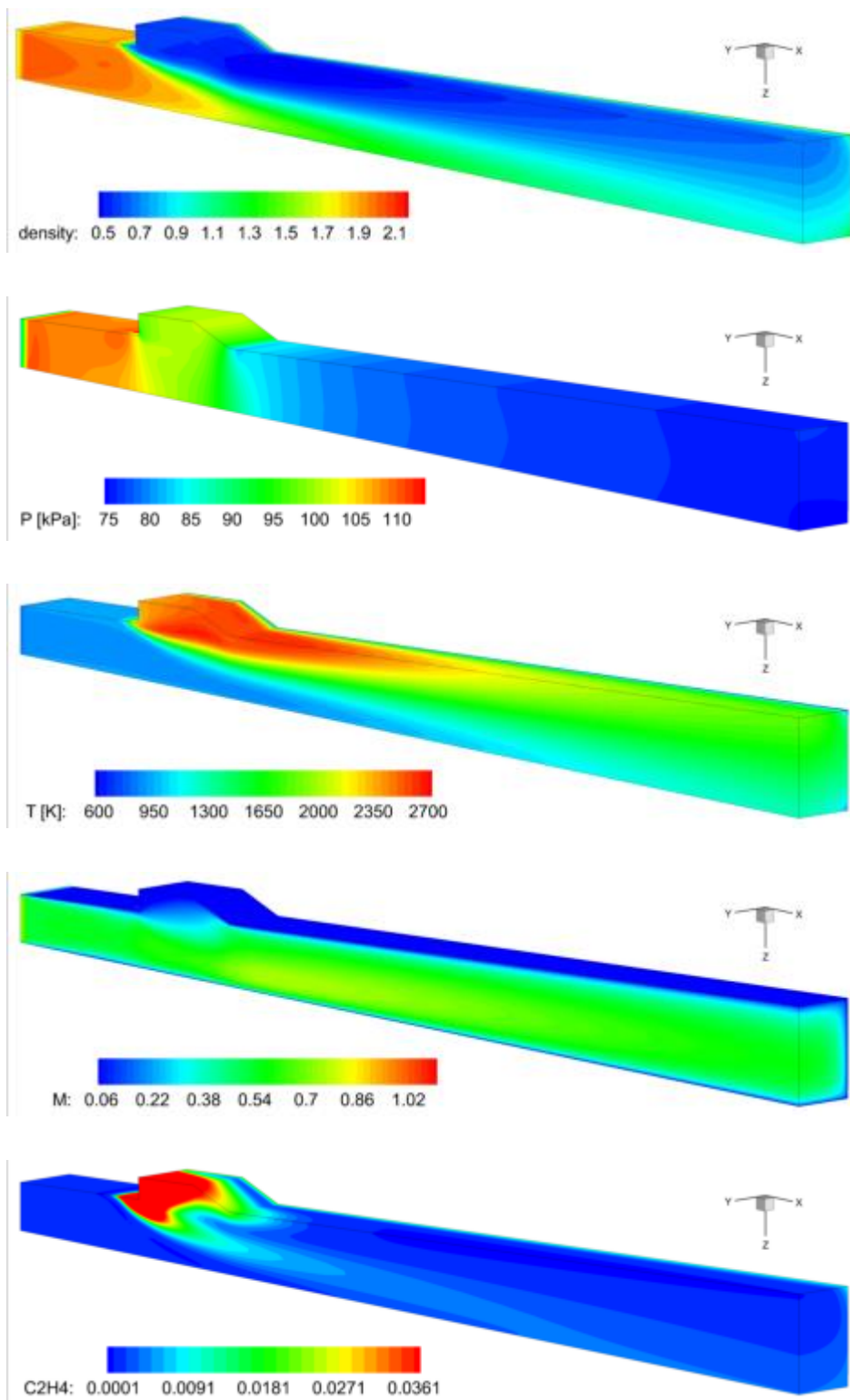
Figure 5.38 Variation of the Flow Variables through the Scramjet Combustor Half Domain (2nd order, Van Leer)
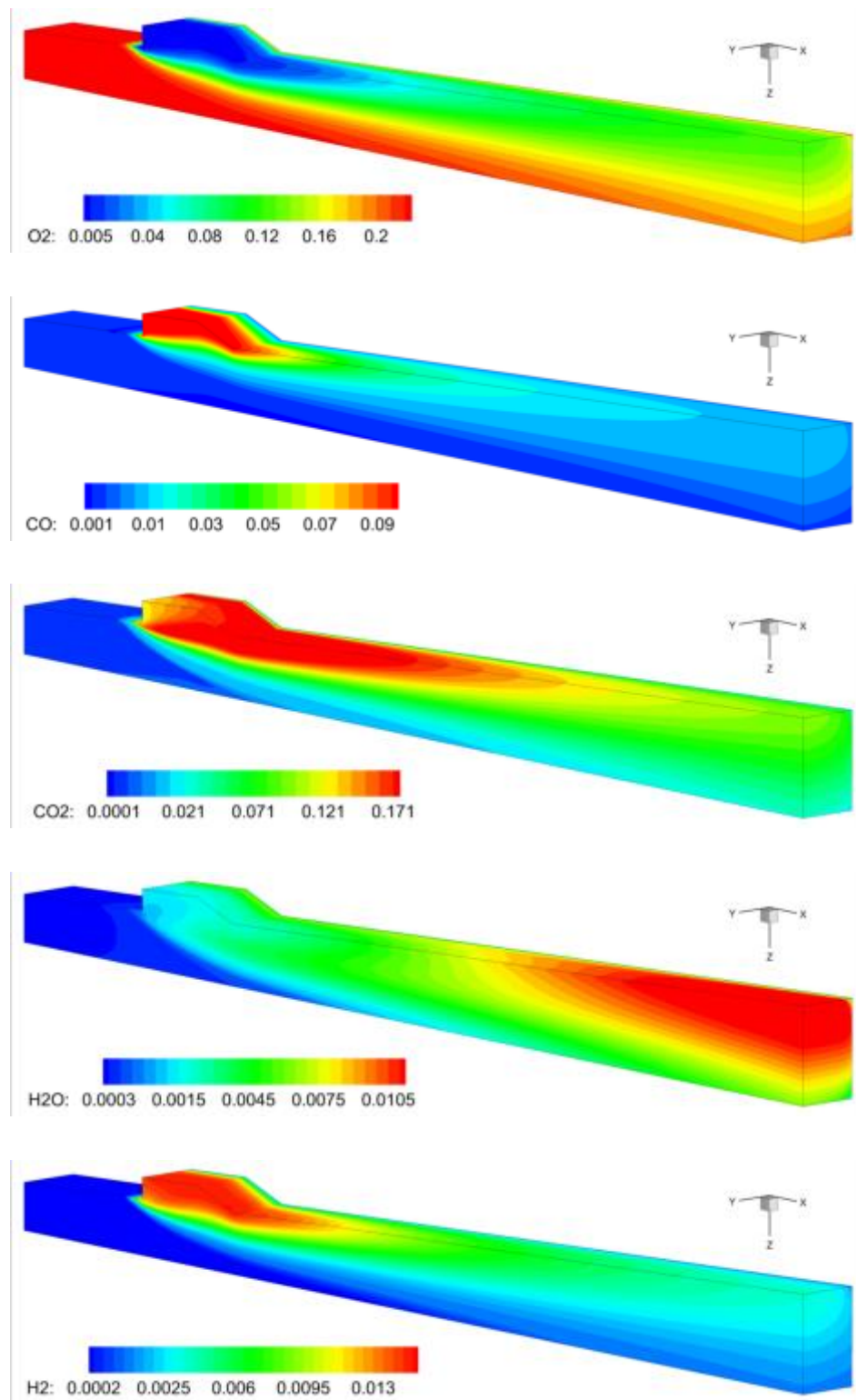
Figure 5.39 Mass Fraction Variation of the Species through the Scramjet Combustor
Half Domain (2nd order, Van Leer)

In order to get insight about how effectively cavity produced a secondary flow region velocity vectors and streamlines are generated over the cavity as shown in Figure 5.40 and Figure 5.41. By analyzing velocity vectors, it can be understood that no-slip boundary condition is achieved on the wall boundaries. In the cavity, the generation of backward flow can be seen clearly. Moreover, streamlines deflects into the cavity region and just behind the front wall of the cavity the circulation of the flow is obvious. The generated circulation region have a great effect on the mixing efficiency of the chemical reactions.
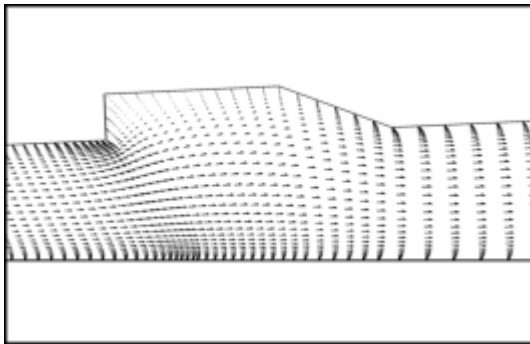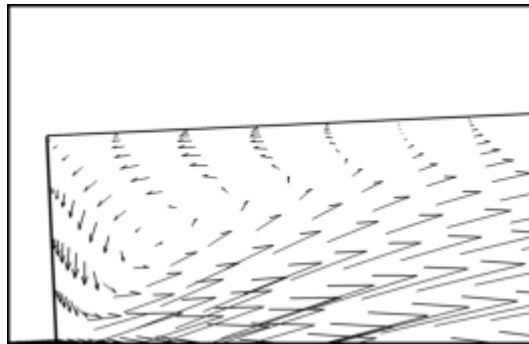
a) Cavity Section   b) Cavity Zoom View

Figure 5.40 Velocity Vectors in the Cavity Region
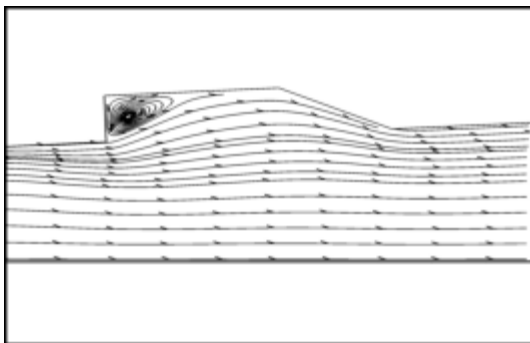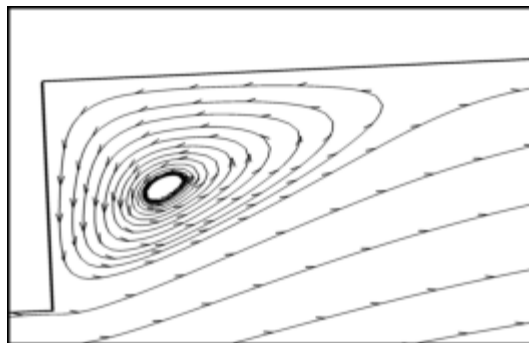
a) Cavity Section   b) Cavity Zoom View

Figure 5.41 Streamlines over the Cavity Region

CHAPTER 6

CONCLUSIONS AND FUTURE WORK

6.1 Conclusions

In this thesis, a CFD code is developed to simulate and analyze the flow of a scramjet combustion chamber. The model used for the analysis is a cavity-based combustor which improves the flameholding and mixing efficiency of the scramjet. Three dimensional coupled Navier-Stokes and finite rate chemical reaction equations are solved using Newton-GMRES method. Newton-GMRES is a matrix free solution i.e. Jacobian matrix is not calculated in its solution process. Moreover, ethylene (C2H4) is used as fuel in the combustion process. The analysis are done with two different fluid characteristics; inviscid and viscous flows. Inviscid flows are employed here to analyze the features of numerical discretization which depends on the inviscid characteristics of the flow such as flux vector splitting methods.

In this study, convective fluxes are split by Steger-Warming, Van Leer and AUSM methods. Moreover, first and second order schemes are employed. Flux splitting methods are compared along with first and second order schemes to find the most efficient and accurate method to perform the analysis. It is shown that Van Leer and AUSM flux splitting methods are computationally more efficient than the Steger-Warming method. AUSM reached the convergence criteria with the lowest CPU time among these methods. However, the accuracy of the solution obtained for AUSM is lower than that of Van Leer's. Furthermore, the analysis of first and second order schemes showed that first order schemes are computationally efficient since they converge in less iteration number and CPU time. Whereas, second order schemes are more accurate and presents more details about the flow than the first orders schemes. In order to increase the efficiency of the second order schemes, flux limiters are

implemented. Flux limiters prevent the oscillations at discontinuities where sharp changes in the flow variable values occurs. The study of flux limiters indicated that they reduce the accuracy of the second order schemes when used in smooth regions. To increase the convergence characteristic of second order schemes while preserving their accuracy a parameter introduced to Van Albada which prevents the activation of limiter function at smooth regions.

In addition, fuel is injected at different angles in and against the flow direction. The analysis show that the injection in the flow direction is generally more efficient than the reverse injection. Also, fuel injection angle of 90 degrees gives the best mixing efficiency for the fuel-air combustion. Moreover, fuel injectors are added downstream of the cavity in order to increase the mixing efficiency. However, the results show that addition of downstream fuel injection do not cause a significant increase in mixing efficiency of the fuel-air.

6.2 Future Work

Coupled equations of Navier-Stokes and finite rate chemical reactions are solved for laminar flows in this study. However, implementing turbulence models will improve the accuracy of the solutions. Moreover, to accelerate the convergence of the solutions for Navier-Stokes equations Multigrid methods can be implemented. In addition, developed CFD tool can easily be modified to solve other parts of the scramjet engine besides to its combustion chamber. Inlet, isolator and nozzle of the scramjet can be analyzed.

REFERENCES

[1]   W. H. Heiser and D. T. Pratt, *Hypersonic Airbreathing Propulsion*. American Institute of Aeronautics and Astronautics, 1994.

[2]   R. Hallion, "The Hypersonic Revolution," *Vol. I*, vol. I, 1987.

[3]   R. J. Weber, J. S. MacKay, and N. G. R. Center, "An analysis of ramjet engines using supersonic combustion." 1958.

[4]   R. S. Fry, "A Century of Ramjet Propulsion Technology Evolution," *J. Propuls. Power*, vol. 20, no. 1, pp. 27–58, 2004.

[5]   N. Hass, M. Smart, and A. Paull, "Flight Data Analysis of the HYSHOT 2," *AIAA/CIRA 13th Int. Sp. Planes Hypersonics Syst. Technol. Conf.*, pp. 1–17, 2005.

[6]   C. Segal, *The scramjet engine : processes and characteristics*, no. 25. 2009.

[7]   A. M. Bonanos, C. P. Goyne, R. W. Barnwell, and J. J. Wang, "Scramjet Operability Range Studies of an Integrated Hydrogen and Hydrocarbon Fuels," no. August, 2005.

[8]   J. J. Mahoney, *Inlets for Supersonic Missiles*. American Institute of Aeronautics and Astronautics, 1990.

[9]   R. A. Baurle and D. R. Eklund, "Analysis of Dual-Mode Hydrocarbon Scramjet Operation at Mach 4-6.5," vol. 18, no. 5, 2002.

[10]   P. E. Dimotakis, "Turbulent Free Shear Layer Mixing and Combustion," in *High Speed Flight Propulsion Systems*, 1991, pp. 265–340.

[11]   K. M. Pandey and T. Sivasakthivel, "Recent Advances in Scramjet Fuel Injection - A Review," *Int. J. Chem. Eng. Appl.*, vol. 1, no. 4, pp. 294–301, 2010.

[12] O. Dessornes and C. Jourdren, "Mixing enhancement techniques in a scramjet," in *8th AIAA International Space Planes and Hypersonic Systems and Technologies Conference*, American Institute of Aeronautics and Astronautics, 1998.

[13] K. Y. Hsu, C. D. Carter, M. R. Gruber, T. Barhorst, and S. Smith, "Experimental Study of Cavity-Strut Combustion in Supersonic Flow," *J. Propuls. Power*, vol. 26, no. 6, pp. 1237–1246, 2010.

[14] T. K. Swain, P. A. Kishan, and S. Kumar, "Comparative Study of the Two Different Strut Based Fuel Injection for 2D Supersonic Combustor Using CFD," 2014, pp. 1–6.

[15] J. Tishkoff, J. Drummond, T. Edwards, A. Nejad, J. Tishkoff, J. Drummond, T. Edwards, and A. Nejad, "Future directions of supersonic combustion research - Air Force/NASA workshop on supersonic combustion," in *35th Aerospace Sciences Meeting and Exhibit*, American Institute of Aeronautics and Astronautics, 1997.

[16] A. (Alexander) S. Roudakov, V. L. Semenov, V. I. Kopchenov, and J. W. Hicks, "Future flight test plans of an axisymmetric hydrogen-fueled scramjet engine on the Hypersonic Flying Laboratory," in *7th International Spaceplanes and Hypersonic Conference*, 1996.

[17] P. Ortwerth, A. Mathur, V. Vinogradov, V. Grin, M. Goldfeld, and A. Starov, "Experimental and numerical investigation of hydrogen and ethylene combustion in a Mach 3-5 channel with a single injector," in *32nd Joint Propulsion Conference and Exhibit*, American Institute of Aeronautics and Astronautics, 1996.

[18] Z. Wang, H. Wang, and M. Sun, "Review of cavity-stabilized combustion for scramjet applications," *Proc. Inst. Mech. Eng. Part G J. Aerosp. Eng.*, vol. 228, no. 14, pp. 2718–2735, Feb. 2014.

[19] M. R. Gruber, U. S. A. Force, P. Air, F. Base, R. A. Baurle, and T. Mathur, "Fundamental Studies of Cavity-Based Flameholder Concepts for Supersonic Combustors Introduction," vol. 17, no. 1, 2001.

[20] X. Zhang and J. A. Edwards, "An investigation of supersonic oscillatory cavity flows driven by thick shear layer," *Aeronatical J.*, vol. 92, no. 940, pp. 355–364, 1990.

[21] A. Ben-Yakar and R. K. Hanson, "Cavity Flame-Holders for Ignition and Flame Stabilization in Scramjets: An Overview," *J. Propuls. Power*, vol. 17, no. 4, pp. 869–877, Jul. 2001.

[22] K.-Y. Hsu, L. P. Goss, and W. M. Roquemore, "Characteristics of a Trapped-Vortex Combustor," *J. Propuls. Power*, vol. 14, no. 1, pp. 57–65, 1998.

[23] A. Ben-Yakar, "Experimental Investigation of Mixing and Ignition of Transverse Jets in Supersonic Crossflows," *Mech. Eng.*, vol. Doctor of , p. 217, 2000.

[24] X. Zhang, A. Rona, and J. Edwards, "The effect of trailing edge geometry on cavity flow oscillation driven by a supersonic shear layer," *Aeronaut. J.*, vol. 102, no. 1013, pp. 129–136, 1998.

[25] M. Samimy, H. L. Petrie, and a. L. Addy, "A study of compressible turbulent reattaching free shear layers," *AIAA J.*, vol. 24, no. 2, pp. 261–267, 1986.

[26] K. Lin and C. Tam, "Fueling Study on Scramjet Operability Enhancement," no. August, pp. 1–15, 2009.

[27] C. D. Ghodke, J. J. Choi, S. Srinivasan, and S. Menon, "Large Eddy Simulation of Supersonic Combustion in a Cavity-Strut Flameholder," *AIAA*, no. January, 2011.

[28] C. Park, "Nonequilibrium hypersonic aerothermodynamics," *Phys. Today*, vol. 44, no. 2, p. 98, 1989.

[29] C. Craddock, "Computational optimization of scramjets and shock tunnel nozzles," no. August, pp. 1–333, 1999.

[30] B. J. McBride, M. J. Zehe, and S. Gordon, "NASA Glenn Coefficients for Calculating Thermodynamic Properties of Individual Species," *Tech. Rep. NASA*, vol. 211556, no. September, p. 291, 2002.

[31] M. Yumuşak and S. Eyi, "Design optimization of rocket nozzles in chemically reacting flows," *Comput. Fluids*, vol. 65, pp. 25–34, Jul. 2012.

[32] M. J. Zehe, S. Gordon, and B. J. McBride, "CAP: A Computer Code for Generating Tabular Thermodynamic Functions from NASA Lewis Coefficients," no. February, 2002.

[33] R. J. Biasca, "Chemical Kinetics of SCRAMJET Propulsion by Rodger Joseph Biasca," 1988.

[34] I. Glassman and R. A. Yetter, *Combustion*. 1996.

[35] M. W. J. Chase, *NIST-JANAF Thermochemical Tables*. American Inst. of Physics, 1998.

[36] K. Roberts, "Analysis And Design Of A Hypersonic Scramjet Engine With A Starting Mach …," *Dspace.Uta.Edu*, no. August, 2008.

[37] P. J. Waltrup, "Upper Bounds on the Flight Speed of Hydrocarbon-Fueled Scramjet-Powered Vehicles," *J. Propuls. Power*, vol. 17, no. 6, pp. 6–11, 2001.

[38] M. J. Lewis, "Significance of Fuel Selection for Hypersonic Vehicle Range," *J. Propuls. Power*, vol. 17, no. 6, pp. 1214–1221, 2001.

[39] O. a. Powell, J. T. Edwards, R. B. Norris, K. E. Numbers, and J. a. Pearce, "Development of Hydrocarbon-Fueled Scramjet Engines: The Hypersonic Technology (HyTech) Program," *J. Propuls. Power*, vol. 17, no. 6, pp. 1170–1176, 2001.

[40] M. R. Gruber, J. M. Donbar, C. D. Carter, and K.-Y. Hsu, "Mixing and Combustion Studies Using Cavity-Based Flameholders in a Supersonic Flow," *Journal of Propulsion and Power*, vol. 20. pp. 769–778, 2004.

[41] C. C. Rasmussen, J. F. Driscoll, K.-Y. Hsu, J. M. Donbar, M. R. Gruber, and C. D. Carter, "Stability limits of cavity-stabilized flames in supersonic flow," *Proc. Combust. Inst.*, vol. 30, no. 2, pp. 2825–2833, Jan. 2005.

[42] B. Varatharajan and F. A. Williams, "Ethylene ignition and detonation chemistry, part 2: ignition histories and reduced mechanisms," *J. Propuls. Power*, vol. 18, no. 2, pp. 352–362, 2002.

[43] D. Eklund, R. Baurle, and M. Gruber, "Numerical study of a scramjet combustor fueled by an aerodynamic ramp injector in dual-mode combustion," in *39th Aerospace Sciences Meeting and Exhibit*, American Institute of Aeronautics and Astronautics, 2001.

[44] K. A. K. A. Hoffmann and S. T. Chiang, *Computational Fluid Dynamics Volume II*. 2000.

[45] F. Liu, "Numerical calculation of turbomachinery cascade flows," Ph.D. Dissertation, Princeton University, 1991.

[46] J. L. Steger and R. . Warming, "Flux vector splitting of the inviscid gasdynamic equations with application to finite-difference methods," *J. Comput. Phys.*, vol. 40, no. 2, pp. 263–293, 1981.

[47] B. Van Leer, "Flux-vector splitting for the Euler equations," in *8th International Conference on Numerical Methods in Fluid Dynamics*, 1982.

[48] M.-S. Liou and C. J. Steffen, "A New Flux Splitting Scheme," *J. Comput. Phys.*, vol. 107, no. 1, pp. 23–39, 1993.

[49] V. Venkatakrishnan, "Convergence to Steady State Solutions of the Euler Equations on Unstructured Grids with Limiters," *J. Comput. Phys.*, vol. 118, no. 1. pp. 120–130, 1995.

[50] B. Yildizlar, S. Eyi, and M. Yumusak, "Comparison of Newton and Newton-GMRES Methods for Three Dimensional Supersonic Nozzle Design," in *32nd AIAA Applied Aerodynamics Conference*, American Institute of Aeronautics and Astronautics, 2014.

[51] Z. BAI, D. HU, and L. REICHEL, "A Newton basis GMRES implementation,"
      IMA J. Numer. Anal., vol. 14, no. 4, pp. 563–581, 1994.

APPENDIX A

DATA OF THE SPECIES' PROPERTIES

Data for the species used in this study are acquired from the tabular thermodynamic functions from NASA Lewis Coefficients by Zehe, M. J. et al. [32].

Table A.1 Thermodynamic Properties of the Species

Species	Molecular weight (kg/mol)	$\Delta_f H^0 (298.15K)$	Percentage at inlet
C_2H_4	0.028	52.5	0.0 %
CO	0.028	428.4	0.1 %
CO_2	0.044	−393.5	< 0.1 %
H_2O	0.018	−241.8	< 0.1 %
O_2	0.032	0.0	21.8 %
H_2	0.002	0.0	< 0.1 %
N_2	0.028	0.0	78.0 %

The coefficients of polynomials obtained from the curve fits of the experimental data are tabulated for different species in the study of McBride, B. J. et al. [30]. The coefficients for the species used in this study are given as follows:

Table A.2 Polynomial Coefficients of C_2H_4

Coefficients	$200 - 1000\ K$	$1000 - 6000\ K$	$6000 - 20000\ K$
a_1	-1.163605836E+05	3.408763670E+06	-
a_2	2.554851510E+03	-1.374847903E+04	-
a_3	-1.609746428E+01	2.365898074E+01	-
a_4	6.625779320E-02	-2.423804419E-03	-
a_5	-7.885081860E-05	4.431395660E-07	-
a_6	5.125224820E-08	-4.352683390E-11	-
a_7	-1.370340031E-11	1.775410633E-15	-
b_1	-6.176191070E+03	8.820429380E+04	-
b_2	1.093338343E+02	-1.371278108E+02	-

Table A.3 Polynomial Coefficients of CO

Coefficients	$200 - 1000\ K$	$1000 - 6000\ K$	$6000 - 20000\ K$
a_1	1.489045326E+04	4.619197250E+05	8.868662960E+08
a_2	-2.922285939E+02	-1.944704863E+03	-7.500377840E+05
a_3	5.724527171E+00	5.916714180E+00	2.495474979E+02
a_4	-8.176235030E-03	-5.664282830E-04	-3.956351100E-02
a_5	1.456903469E-05	1.398814540E-07	3.297772080E-06
a_6	-1.087746302E-08	-1.787680361E-11	-1.318409933E-10
a_7	3.027941827E-12	9.620935570E-16	1.998937948E-15
b_1	-1.303131878E+04	-2.466261084E+03	5.701421130E+06
b_2	-7.859241350E+00	-1.387413108E+01	-2.060704786E+03

Table A.4 Polynomial Coefficients of CO_2

Coefficients	$200 - 1000\ K$	$1000 - 6000\ K$	$6000 - 20000\ K$
a_1	4.943650540E+04	1.176962419E+05	-1.544423287E+09
a_2	-6.264116010E+02	-1.788791477E+03	1.016847056E+06
a_3	5.301725240E+00	8.291523190E+00	-2.561405230E+02
a_4	2.503813816E-03	-9.223156780E-05	3.369404080E-02
a_5	-2.127308728E-07	4.863676880E-09	-2.181184337E-06
a_6	-7.689988780E-10	-1.891053312E-12	6.991420840E-11
a_7	2.849677801E-13	6.330036590E-16	-8.842351500E-16
b_1	-4.528198460E+04	-3.908350590E+04	-8.043214510E+06
b_2	-7.048279440E+00	-2.652669281E+01	2.254177493E+03

Table A.5 Polynomial Coefficients of H_2O

Coefficients	$200 - 1000\ K$	$1000 - 6000\ K$	$6000 - 20000\ K$
a_1	-3.947960830E+04	1.034972096E+06	-
a_2	5.755731020E+02	-2.412698562E+03	-
a_3	9.317826530E-01	4.646110780E+00	-
a_4	7.222712860E-03	2.291998307E-03	-
a_5	-7.342557370E-06	-6.836830480E-07	-
a_6	4.955043490E-09	9.426468930E-11	-
a_7	-1.336933246E-12	-4.822380530E-15	-
b_1	-3.303974310E+04	-1.381286509E+04	-
b_2	1.724205775E+01	-7.978148510E+00	-

Table A.6 Polynomial Coefficients of O_2

Coefficients	$200-1000\ K$	$1000-6000\ K$	$6000-20000\ K$
a_1	-3.425563420E+04	-1.037939033E+06	4.975294300E+08
a_2	4.847000970E+02	2.344830282E+03	-2.866106875E+05
a_3	1.119010961E+00	1.819732036E+00	6.690352250E+01
a_4	4.293889240E-03	1.267847582E-03	-6.169959020E-03
a_5	-6.836300520E-07	-2.188067988E-07	3.016396027E-07
a_6	-2.023372700E-09	2.053719572E-11	-7.421416600E-12
a_7	1.039040018E-12	-8.193467050E-16	7.278175770E-17
b_1	-3.391454870E+03	-1.689010929E+04	2.293554027E+06
b_2	1.849699470E+01	1.738716506E+01	-5.530621610E+02

Table A.7 Polynomial Coefficients of H_2

Coefficients	$200-1000\ K$	$1000-6000\ K$	$6000-20000\ K$
a_1	4.078323210E+04	5.608128010E+05	4.933884120E+08
a_2	-8.009186040E+02	-8.371504740E+02	-3.147547149E+05
a_3	8.214702010E+00	2.975364532E+00	7.984121880E+01
a_4	-1.269714457E-02	1.252249124E-03	-8.414789210E-03
a_5	1.753605076E-05	-3.740716190E-07	4.753248350E-07
a_6	-1.202860270E-08	5.936625200E-11	-1.371873492E-11
a_7	3.368093490E-12	-3.606994100E-15	1.605461756E-16
b_1	2.682484665E+03	5.339824410E+03	2.488433516E+06
b_2	-3.043788844E+01	-2.202774769E+00	-6.695728110E+02

Table A.8 Polynomial Coefficients of N_2

Coefficients	$200 - 1000\ K$	$1000 - 6000\ K$	$6000 - 20000\ K$
a_1	2.210371497E+04	5.877124060E+05	8.310139160E+08
a_2	-3.818461820E+02	-2.239249073E+03	-6.420733540E+05
a_3	6.082738360E+00	6.066949220E+00	2.020264635E+02
a_4	-8.530914410E-03	-6.139685500E-04	-3.065092046E-02
a_5	1.384646189E-05	1.491806679E-07	2.486903333E-06
a_6	-9.625793620E-09	-1.923105485E-11	-9.705954110E-11
a_7	2.519705809E-12	1.061954386E-15	1.437538881E-15
b_1	7.108460860E+02	1.283210415E+04	4.938707040E+06
b_2	-1.076003316E+01	-1.586639599E+01	-1.672099736E+03

APPENDIX B

FLUX VECTOR SPLITTING METHODS

B.1. Steger-Warming Method

The flux vector obtained in η and ζ directions using Steger-Warming method are given as:

$$
\hat{G}_c^\pm = \frac{\rho}{2\gamma}
\begin{bmatrix}
\beta \\
\beta u + a(\lambda_1^\pm - \lambda_3^\pm)\hat{\eta}_x \\
\beta v + a(\lambda_1^\pm - \lambda_3^\pm)\hat{\eta}_y \\
\beta w + a(\lambda_1^\pm - \lambda_3^\pm)\hat{\eta}_z \\
\beta \dfrac{(u^2 + v^2 + w^2)}{2} + aU(\lambda_1^\pm - \lambda_3^\pm) + \dfrac{a^2(\lambda_1^\pm - \lambda_3^\pm)}{\gamma - 1} \\
\beta(\rho_1/\rho) \\
\vdots \\
\beta(\rho_{K-1}/\rho)
\end{bmatrix}
$$

$$
\hat{H}_c^\pm = \frac{\rho}{2\gamma}
\begin{bmatrix}
\beta \\
\beta u + a(\lambda_1^\pm - \lambda_2^\pm)\hat{\zeta}_x \\
\beta v + a(\lambda_1^\pm - \lambda_2^\pm)\hat{\zeta}_y \\
\beta w + a(\lambda_1^\pm - \lambda_2^\pm)\hat{\zeta}_z \\
\beta \dfrac{(u^2 + v^2 + w^2)}{2} + aU(\lambda_1^\pm - \lambda_2^\pm) + \dfrac{a^2(\lambda_1^\pm - \lambda_2^\pm)}{\gamma - 1} \\
\beta(\rho_1/\rho) \\
\vdots \\
\beta(\rho_{K-1}/\rho)
\end{bmatrix}
\tag{B.1}
$$

B.2. Van Leer Method

The flux vector in η and ζ directions using Van Leer method are found as:

$$\hat{G}_c^{\pm} = \pm\frac{\rho a}{J}\left(\frac{M\pm 1}{2}\right)^2 \begin{bmatrix} 1 \\ \frac{1}{\gamma}(-\hat{U}_\eta \pm 2a)\hat{\eta}_x + u \\ \frac{1}{\gamma}(-\hat{U}_\eta \pm 2a)\hat{\eta}_y + u \\ \frac{1}{\gamma}(-\hat{U}_\eta \pm 2a)\hat{\eta}_z + u \\ \frac{\hat{U}_\eta(-\hat{U}_\eta \pm 2a)}{\gamma + 1} + \frac{2a}{\gamma^2 - 1} + \frac{u^2 + v^2 + w^2}{2} \\ \rho_1/\rho \\ \vdots \\ \rho_{K-1}/\rho \end{bmatrix}$$

$$\hat{H}_c^{\pm} = \pm\frac{\rho a}{J}\left(\frac{M\pm 1}{2}\right)^2 \begin{bmatrix} 1 \\ \frac{1}{\gamma}(-\hat{U}_\zeta \pm 2a)\hat{\zeta}_x + u \\ \frac{1}{\gamma}(-\hat{U}_\zeta \pm 2a)\hat{\zeta}_y + u \\ \frac{1}{\gamma}(-\hat{U}_\zeta \pm 2a)\hat{\zeta}_z + u \\ \frac{\hat{U}_\zeta(-\hat{U}_\zeta \pm 2a)}{\gamma + 1} + \frac{2a}{\gamma^2 - 1} + \frac{u^2 + v^2 + w^2}{2} \\ \rho_1/\rho \\ \vdots \\ \rho_{K-1}/\rho \end{bmatrix}$$

(B.2)

B.3. AUSM Method

The flux vectors obtained in η and ζ directions using AUSM method are:

$$\hat{G}_c^{\pm} = M^{\pm}\begin{bmatrix} \rho a \\ \rho a + u\hat{\eta}_x p^{\pm} \\ \rho a + v\hat{\eta}_y p^{\pm} \\ \rho a + w\hat{\eta}_z p^{\pm} \\ a(\rho e_t + (\gamma - 1)\,\varphi) \\ \rho a(\rho_1/\rho) \\ \vdots \\ \rho a(\rho_{K-1}/\rho) \end{bmatrix} \qquad \hat{H}_c^{\pm} = M^{\pm}\begin{bmatrix} \rho a \\ \rho a + u\hat{\zeta}_x p^{\pm} \\ \rho a + v\hat{\zeta}_y p^{\pm} \\ \rho a + w\hat{\zeta}_z p^{\pm} \\ a(\rho e_t + (\gamma - 1)\,\varphi) \\ \rho a(\rho_1/\rho) \\ \vdots \\ \rho a(\rho_{K-1}/\rho) \end{bmatrix}$$ (B.3)

where,

$$\varphi = \left(\rho e - \frac{u^2 + v^2 + w^2}{2}\right)$$